Development of Tubular Solar Receiver with Supercritical Carbon Dioxide as Working Fluid

A Thesis

Submitted for the Degree of

Doctor of Philosophy (Engineering)

in the Faculty of Engineering

By

Sagar D. Khivsara

Department of Mechanical Engineering

Indian Institute of Science

Bangalore – 560 012, India

December 2018

Dedicated to

My Parents, Friends and Teachers

ACKNOWLEDGEMENT

I would like to express profound gratitude to my advisor Prof. Pradip Dutta for his invaluable support, guidance and encouragement; and for providing inspiration and refreshing enthusiasm in every discussion over the course of this work. His insights, intuition and experience amazingly streamlined things and taught me a systematic way of doing research.

I would also like to thank Prof. K. P. J. Reddy (IISc) and his team for providing the guidance and resources for measurements using their shock tube facility at LHSR, IISc. Support from Dr. R. N. Das and inputs from his BHEL team have had a profound impact throughout this work.

I take this opportunity to thank Dr. Clifford Ho from Sandia National Laboratories (SNL) for the many insightful discussions and the opportunity to perform experiments at SNL. His critical comments, precise observations and guidance played a pivotal role in this work. The enthusiasm, guidance and huge support provided by Jesus Ortega (SNL) has been instrumental for successful completion of this research. Working with Jesus has been the most wonderful learning experience; he is an exceptional friend and a wonderful human being. The intercontinental collaborative research which is a part of this thesis would not have been possible without continuous support and involvement from Joshua Christian, Julius Yellowhair and numerous other scientists and technicians at the National Solar Thermal Test Facility at SNL, USA.

This acknowledgment will be incomplete without a mention of the world class faculty at IISc that I feel privileged to be taught and mentored by. Working at IISc has been a life-changing experience. I would like to thank all the ‘Heat Transfer Lab’ members, with a special mention of Aswin, who is a remarkable person and a great friend. Through countless discussions during this work, he helped me ask the right questions and seek answers for them.

Lastly, I would like to thank my parents, wife, brother and friends for their continuous support and encouragement to embark on this beautiful and enriching journey at IISc.

-Sagar Khivsara, Dept. of Mechanical Engineering, IISc Bangalore

ABSTRACT

Over the past decade, solar powered supercritical carbon dioxide (s-CO_2) based Brayton cycle has been identified as a promising candidate due to its potentially high cycle efficiency (50%, for turbine inlet temperatures of ~ 1000 K). Materialization of this cycle requires development of solar receivers capable of heating s-CO_2 by over 200 K, to a receiver outlet temperature of about 1000 K. Due to the extreme outlet conditions (~1000 K, 20 MPa), tubular solar receivers which typically employ panels consisting of metallic circular tubes for transfer of the incident concentrated solar radiation to the fluid flowing within the tubes are considered to be a suitable option for direct heating of s-CO_2.

In the design of receivers/heat exchangers for s-CO_2 Brayton cycle, equipment wall temperatures above 1000 K are anticipated. While CO_2 is considered to be transparent to the solar radiation spectrum, it has considerable absorption component in the longer wavelength range. This absorption effect may be present for s-CO_2 also, yet its participating nature in radiation heat transfer has been traditionally ignored for flow through tubes. In this study, a numerical analysis using existing analytical data for s-CO_2 absorption spectrum has been performed to study the fundamental aspects of a developing laminar flow of s-CO_2 for a constant heat flux boundary condition. It is observed that while the velocity profiles remain largely unaffected, augmentation of overall heat transfer coefficient and Nusselt number due to presence of radiation heat transfer in addition to convection and conduction has a significant effect on the temperature distribution on the tube wall and its vicinity. It is found that for accurate design and estimation of heat transfer performance of s-CO_2 equipment, the participating nature of s-CO_2 can be critical for laminar and low Reynolds number turbulent flows. In general, the effect of absorption can be increasingly significant for lower values of Reynolds number and larger values of tube internal emissivity, tube diameter, tube length and the incident heat flux.

In addition to absorption of radiation, emission by s-CO_2 may also be significant and has been ignored in the literature in spite of the high temperatures involved. To investigate this aspect, a novel experimental method for measurement of radiation emitted by s-CO_2 at high pressure and high temperature is presented in this thesis. Due to high pressure conditions, use of conventional spectroscopic methods to measure radiative properties of s-CO_2 is challenging. In the present method, supercritical conditions are created in a shock tube by using carbon dioxide (CO_2) as the driven gas, and a platinum thin film sensor is used to measure the radiation heat flux emitted by s-CO_2. The total emissivity for s-CO_2 is estimated and the value compares favourably with that predicted theoretically using a standard method available in literature. It is estimated that the total emissivity value in supercritical conditions is nearly 0.2 for the conditions studied, implying that s-CO_2 acts as a participating medium for radiation heat transfer. The outcome of this study has a significant impact on the design and analysis of heat transfer equipment where laminar or low Reynolds number turbulent flows are encountered.

For accurate and realistic design of a tubular solar receiver, a novel methodology for coupled optical-thermal-fluid analysis is presented in this work and the proposed methodology is utilized for developing a prototype of s-CO_2 receiver consisting of panels constituted by tubes. First, a preliminary analysis is presented, detailing the methodology for coupled analysis. The effect of staggering the tubes to increase the effective absorptance and reduce the reflective losses is explored. A receiver consisting of a single large panel is analysed to establish the methodology and to estimate the tube wall temperature and efficiency for a typical incident flux distribution on the receiver tubes in conjunction with flow of s-CO_2

through the tubes. Subsequently, detailed optical-thermal-fluid analysis and design of a s-CO_2 tubular receiver with flat panels is performed. Different flow arrangements with and without recirculation, aim point strategies and power levels of operation are studied for comprehensive evaluation of the receiver performance under different conditions. It is found that the receiver designed is able to provide the required temperature rise while the pressure drop and peak receiver temperatures are within allowable limits.

As found in a recent study at Sandia National Laboratories, arrangement of the receiver panels in the form of blades can result in an increase in the overall receiver efficiency by up to 5 % compared to the flat receiver arrangement, due to better optics. This bladed receiver arrangement is adopted in the final stage of this work for modelling, testing and design validation of the s-CO_2 receiver using compressed air as the heat transfer fluid. Details of the bladed receiver configuration, coupled modelling, prototyping and testing are presented in this thesis. For high temperature on-sun testing on a solar tower, despite the limited availability of pressurized air, a unique test strategy is employed. The receiver is successfully demonstrated to safely heat air up to a temperature of 700 K, with receiver wall temperatures approaching 1000 K. To account for the thermal mass associated with the transient nature of the tests and heating of the non-irradiated part of the receiver structure during the on-sun tests, a modified receiver efficiency calculation is proposed in this work. The agreement between the measured and simulated values of receiver efficiency, temperature and heat flux distributions is found to be satisfactory.

TABLE OF CONTENTS

LIST OF FIGURES

LIST OF TABLES

NOMENCLATURE

a	absorption coefficient (m^{-1}), correlation parameter for equation 4.6
A	total surface area (m^2)
b	correlation parameter for equation 4.6
c	correlation parameter for equation 4.6
C	specific heat (J/kg-K)
D	tube diameter (mm)
E	voltage (mV or V)
h	specific enthalpy (J/kg-K), convection heat transfer coefficient (W/m^2-K)
I	current (mA)
k	turbulent kinetic energy (J)
k_s	thermal conductivity (W/m-K)
L	tube length (mm)
M	Mach number
$\dot{m}$	mass flow rate (kg/s)
n	number of aim points
Nu	Nusselt Number
P5	pressure of shocked gas after reflected wave has passed (bar)
P_E	effective pressure
$\dot{q}$	heat flux (W/m^2)
Q	heat (W)
R	resistance (Ω)
Re	Reynolds number
t	time (s)
T	temperature (K)
T5	temperature of shocked gas after reflected wave has passed (K)
V	voltage (V)
Y+	non-dimensional cell height

Greek alphabets:

α	temperature coefficient of resistance (K^{-1})

β	MACOR (backing material) parameter defined by $\sqrt{\rho C k_s}$ ($W/m^2\text{-}K^1\text{-}s^{1/2}$)
γ	ratio of specific heats
ρ	density (kg/m^3)
ε	dissipation rate (J/kg-s) in k-ε turbulence model, emissivity
ω	specific turbulence dissipation (/s)
σ	Stefan-Boltzmann constant ($W/m^2\text{-}K^4$)
λ	wavelength (m)
η, φ	efficiency
ϵ	emissivity

Subscripts:

1	initial Mach number
abs	absorbed
b	black body, bulk fluid
conv	convective
e	electrical
eff	effective
f	initial voltage, fluid
h	heated portion
i, n	time step
in	receiver inlet
in	incident
inp	input
max	maximum
opt	optical
out	receiver outlet
p	constant pressure
rad	radiation
surf	surface
th	thermal
w	wall
∞	ambient

1. INTRODUCTION AND BACKGROUND

1.1. CONCENTRATED SOLAR POWER (CSP)

The production of electricity in an eco-friendly and cost-effective manner is a crucial challenge which the world faces today. Addressing the ever-increasing energy requirements of large populations while minimizing the adverse impact on our environment is a concerning issue for developing as well as industrialized nations around the world. With the over-reliance on digital communications and electrical appliances, electrical energy is increasingly becoming an inseparable part of our lives. The change in lifestyle and evolution of human society will be largely dependent on how widely energy is going to be accessible and affordable. With the rapidly depleting reserves of fossil fuels and the increasing adverse effects by use of conventional sources of energy, it is obvious that renewable energy sources will play a central role towards achieving the goal of an environment friendly, economical and energy intensive society. In particular, solar energy has a promising capability to meet the ever increasing energy demands.

There are two popular technologies which are employed for conversion of solar energy to electric power:

- Photovoltaic (PV) technology: Flat panels of ‘solar cells’ are employed for direct conversion of incident solar energy to electrical energy.
- Concentrated Solar Power (CSP) technology: Incoming solar radiation is used to heat a pressurized fluid stream, which then serves as the working fluid for conventional power plants.

Of the two approaches mentioned above, the second approach, i.e. CSP is particularly suited for production of electrical energy at a large scale. In this technology, the incoming solar radiation is reflected using mirrors and concentrated on a surface where the radiation is absorbed and the energy is transferred to a heat transfer fluid. CSP systems typically concentrate the solar irradiation on earth to heat a stream of pressurized working fluid which then expands in a turbine to generate electricity as in a conventional thermal power plant.

The decisive advantage of CSP technology over other renewable sources of energy is the prospect of employing thermal energy storage. Also, CSP plants offer ease of cogeneration by operating in a hybrid mode, allowing use of other heat sources such as biomass or fossil fuels. Consequently, CSP plants have the capability to generate electricity even at night and during periods of low solar irradiation due to cloud cover and other uncontrollable factors. This renders CSP plants suitable for supplying electricity at both, base load and peak load requirements.

Figure 1.1 illustrates the basic building blocks of a CSP plant. The plant consists of:

- an optical concentration system comprising of flat mirrors, reflective dishes or troughs whose function is to track the sun and concentrate the solar irradiation by reflecting it towards a designated spot/surface/area, depending on the collector geometry.
- a solar receiver, where the concentrated radiation energy received from the reflectors is transferred to a heat transfer fluid
- a power block/heat engine whose function is to utilize the hot high pressure fluid delivered by the receiver for producing electricity through power cycles such as Brayton/Rankine/Stirling cycles

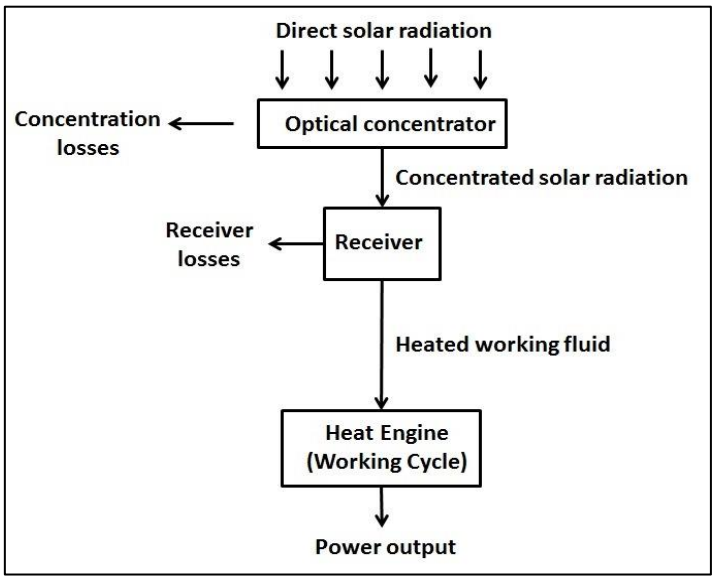

Fig. 1.1: Building blocks of a CSP plant

Existing CSP systems employ one of the following four configurations:

1. Parabolic Trough
2. Linear Fresnel Reflector
3. Power Dish
4. Power Tower (also called Central Receiver or Central Tower)

The parabolic trough technology typically consists of series of single-axis tracking parabolic concentrating mirrors, which track the sun dynamically throughout the day. The parabolic mirrors reflect and concentrate the solar irradiation on a linear heat absorbing tube that carries the heat transfer fluid. The tube is placed longitudinally along the focus of the parabola. To reduce the heat losses from the tube, an evacuated transparent tube is generally installed outside the metal tube through which the working fluid flows.

In the linear Fresnel reflector system, a linear receiver element through which the heat transfer fluid such as air, water/steam flows is heated by a series of narrow flat mirrors. Instead of utilizing parabolic concentrators, the solar irradiation is reflected by long, parallel and flat reflectors which focus the energy on a line-collector that is typically placed at an elevation above the reflector field. Typically, the linear Fresnel systems efficiency is only up to 70% of the efficiency obtained by using the parabolic trough systems.

Dish based systems typically employ a paraboloid dish as the reflector, in which the reflector surface focuses solar irradiation at the focal point of the paraboloid. A solar receiver located at the focal point absorbs the concentrated radiation and subsequently transfers it to the heat transfer fluid circulating through the receiver.

In a power tower system, also called as a central receiver system (CRS), a large array of flat or slightly curved mirrors, called as ‘heliostats’, is arranged on the ground. These heliostats reflect the incident solar radiation on a small area at the top of a central tower, resulting in a large amount of energy impinging over a small surface at high concentration ratios. The solar receiver, which is placed at the top of the tower, absorbs this concentrated irradiation and transfers the energy to the heat transfer fluid flowing through it.

CSP systems can thus be classified as line-focusing and point-focusing systems. The parabolic and linear Fresnel systems are line-focusing, while the dish based and central tower systems are point-focusing CSP systems. In general, the point-focusing systems result in

larger concentration ratios and are capable of achieving high temperatures. The design of heat transfer element, i.e. the receiver is very challenging for such systems.

1.2. CSP BASED SUPERCRITICAL CARBON DIOXIDE (s-CO_2) BRAYTON CYCLE

In a typical gas turbine power plant operating on the Brayton cycle, the working fluid is first drawn into a compressor where it is pressurized. This pressurized gas then enters the combustor where conventional fuel is burned to heat the gas. The high temperature pressurized gas then enters a gas turbine, where it expands to produce power. The exhaust gas at the exit of the turbine is either released to the atmosphere (open cycle) or recirculated (closed cycle) completely or partially. If the exhaust at the turbine exit is used to heat the colder fluid exiting the compressor, the cycle is designated as Brayton cycle with regeneration.

In recent years, several researchers have proposed that a closed Brayton cycle using supercritical carbon dioxide (s-CO_2) as the working fluid can result in a high cycle efficiency (~50 %) due to significant reduction in compressor work compared to other candidates such as compressed air. The critical pressure and temperature of CO_2 are 304 K and 7.39 MPa, respectively. The high density of s-CO_2 results in extremely compact turbo-machinery and regenerators/heat exchangers. The typical turbine inlet pressure in the proposed cycle is in the range of 15-20 MPa, while the turbine inlet temperature is 900-1000 K. For operating conditions away from the critical point, there is no sudden variation of thermophysical properties such as density, specific heat and thermal conductivity. As all the processes in this cycle involve sensible heating and cooling only, phase change issues in the compressor and turbine are non-existent. Another important advantage of the s-CO_2 Brayton cycle is its scalability, thus providing the possibility of employing large number of compact distributed power plants, resulting in reduction of the transmission costs.

For typical turbine inlet conditions, such as 15 MPa and 1000 K for the s-CO_2 Brayton cycle, the density of s-CO_2 is nearly eleven times that of air at a typical turbine inlet condition for an air-Brayton cycle (4 MPa, 2000 K), while enthalpy of s-CO_2 is more than half of the value of air at the respective conditions. Use of s-CO_2 as the working fluid results in the benefit of having a compact receiver, resulting in low thermal losses and less material cost. Due to the excellent heat transfer properties of s-CO_2, for a particular thermal rating of receiver, a

smaller mass and volume flow rate of s-CO_2 is required for transferring heat from the receiver surface, compared to other working fluids.

Nuclear energy has been conventionally considered as a viable source for heating s-CO_2 before it enters the turbine. In the past decade, CSP as the source of energy for heating s-CO_2 has received considerable attention. The layout and corresponding thermodynamic processes in a solar powered s-CO_2 Brayton cycle with regeneration is shown in figure 1.2. It consists of a concentrating heliostat field, solar receiver, turbine, regenerator, cooler and a compressor.

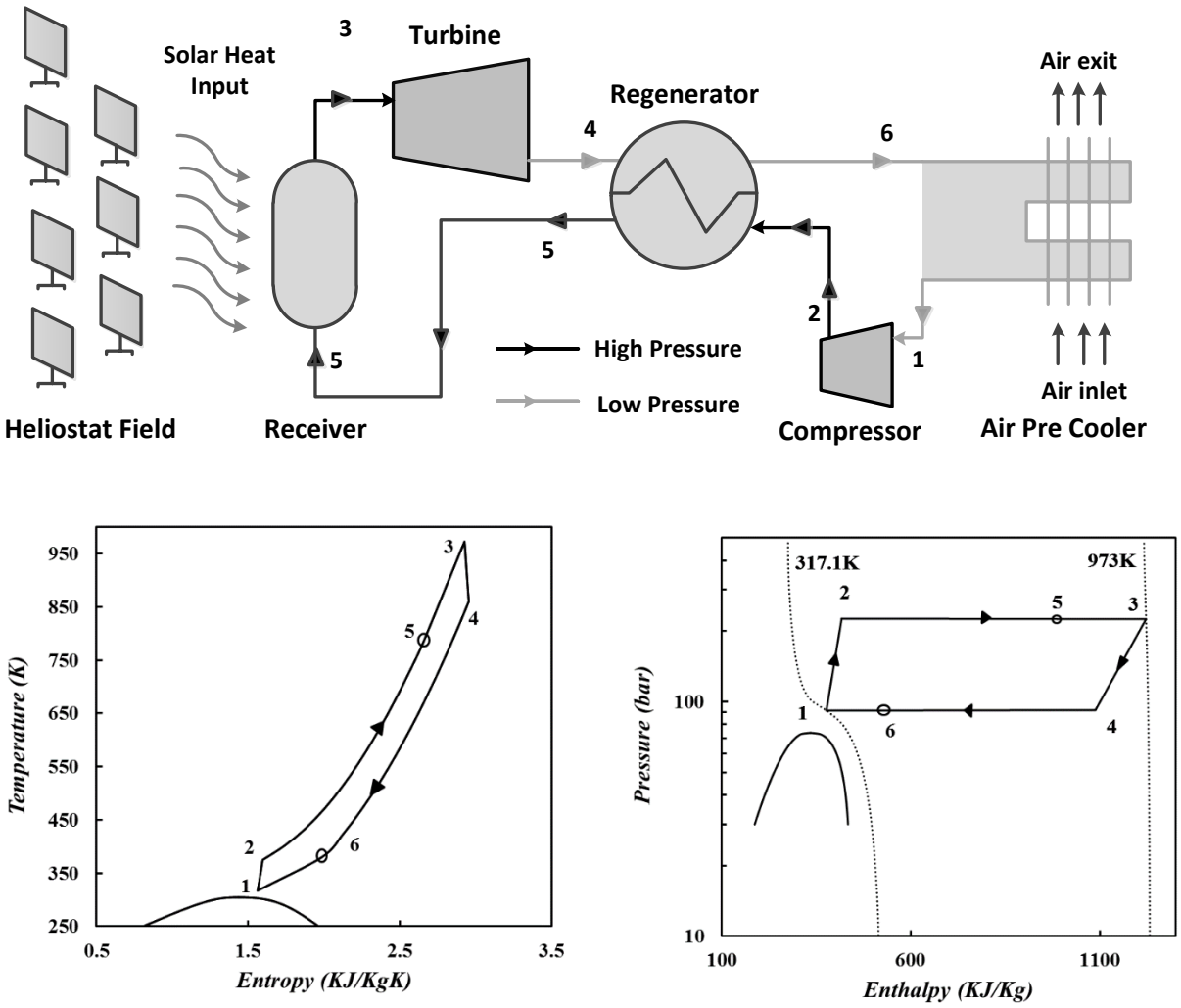

Fig. 1.2: Layout and corresponding thermodynamic process in a solar powered s-CO_2 Brayton cycle with regeneration

The materialization of a solar powered s-CO_2 cycle requires the design and development of a solar receiver capable of raising the temperature of s-CO_2 from around 750 K to 950 K, at pressure around 15-20 MPa.

1.3. SOLAR RECEIVER CONFIGURATIONS

As discussed above, the solar receiver is a key component of the CSP system. It is the component which absorbs the concentrated solar energy reflected by optical concentrators and transfers the thermal energy to the heat transfer fluid.

A solar receiver must efficiently transfer the incident concentrated energy received from the optical concentrator to the working fluid, while losing least possible energy to the atmosphere. For achieving high values of the power cycle efficiency, it is required that the working fluid temperatures are high, which in-turn necessitates that the receiver be subjected to a high concentration ratio resulting in high values of incident heat flux on the receiver aperture. The receiver design thus plays a vital role in efficient conversion of solar energy to electrical energy.

The heat transfer fluid in a solar receiver can either be the working fluid for the power cycle (like s-CO_2) or other any other fluid can be used as the heat transfer fluid in the receiver. An additional heat exchanger is then required for transferring the collected thermal energy from the secondary fluid in receiver to the working fluid in the power block. While direct heating of s-CO_2 would avoid use of an additional heat exchanger and the exergy destruction associated with an additional heat exchange process, use of a secondary heat transfer fluid in the receiver may facilitate easy use of a thermal storage unit to provide energy for operating the s-CO_2 Brayton cycle based power plant during periods of cloud cover and for night-time operation of the plant. Direct heating of s-CO_2 in the receiver coupled with an external thermal energy storage which can be charged and discharged as per requirement is another popular option and has received considerable attention from researchers.

There are four basic receiver configurations which can be employed for heating the working fluids such as air, molten salt or s-CO_2. In a tubular receiver configuration (figure 1.3), the reflectors focus solar energy on the outer surface of the tube. This energy is first conducted

through the thickness of the tube and then convected on the inner wall by the heat transfer fluid flowing inside the tube.

In a typical volumetric receiver configuration (figure 1.4), irradiation from the concentrator impinges on a porous surface of an absorber and penetrates into the volume. The absorber is typically constructed using a metal mesh or a high temperature ceramic material. While radiation penetrates the absorber by undergoing multiple reflections within the absorber, it makes the absorption of energy a volumetric phenomenon. There is simultaneous flow of the receiver heat transfer fluid through the absorber and heat is transferred to the fluid by convection.

The falling particle receiver configuration is shown in figure 1.5. The concentrated solar radiation incident on the receiver aperture impinges on a continuously flowing curtain of small particles, which are either coated to have high absorptivity or have intrinsically high absorptance to effectively absorb most of the incident concentrated solar radiation. These particles are recirculated (if required) and then stored in an insulated chamber as thermal storage. An additional heat exchanger is always required in such a receiver configuration in order to heat the working fluid of the power cycle. Handling of the solid particles present considerable difficulties and effective heat exchange with the pressurized working fluid is another major issue with the falling particle receiver.

For a cavity receiver configuration (figure 1.6), the reflected solar radiation from the concentrator enters a cavity and impinges on the concave surface of the cavity. The absorbed thermal energy is conducted through the cavity wall thickness and subsequently convected to the working fluid which flows on the convex side of the cavity.

Solar receivers are sometimes classified as directly irradiated or indirectly irradiated receivers. In a directly irradiated receiver, energy is transferred to the working fluid at the same surface which absorbs irradiation from the concentrator. In an indirectly irradiated receiver, thermal energy absorbed on a face of the wall is conducted through the wall thickness initially; while the transfer of energy to the working fluid occurs on the opposite face of the wall. Tubular and cavity receiver configurations are examples of indirectly irradiated receivers, while volumetric and falling particle receivers are examples of directly irradiated receivers.

Tubular receivers usually consist of panels which are manufactured by welding a large number of tubes to a common header. Numerous such panels may be arranged next to each other at the top of the tower. The tubular receiver configuration is the simplest configuration of a solar receiver and allows direct heating of pressurized fluids.

Volumetric receivers which consist of porous ceramic/metallic blocks as absorbers are capable of sustaining very high temperatures by using ceramic absorbers. The absorber volume is heated with a large concentrated radiation flux which is absorbed and transferred to the working fluid via convection through the porous matrix. For using pressurized fluids in a volumetric receiver, it is necessary to employ a transparent window for allowing the concentrated solar radiation to enter the receiver structure and interact with the porous medium. The window also performs the function of maintaining the pressure inside the receiver by isolating the absorber and heat transfer fluid from the external atmosphere. For causing least attenuation to the incoming solar radiation, the window for such a volumetric receiver must be thin, but for sustaining a large pressure differential between the working fluid and atmosphere, like in the case of a s-CO_2 volumetric receiver, the window needs to be substantially thick. The window also needs to be highly durable and capable of sustaining high pressure and temperature for the lifetime of receiver. The design of such a window with appropriate sealing for a pressurized high temperature receiver is very difficult and poses a significant task for successful design of a volumetric receiver. Moreover, scalability becomes an issue as larger aperture areas will require thicker windows due to structural considerations. On the other hand, solar receiver configurations such as tubular and cavity receivers eliminate the requirement of a pressurized window by using external surfaces of their opaque walls as the radiation absorbing surfaces.

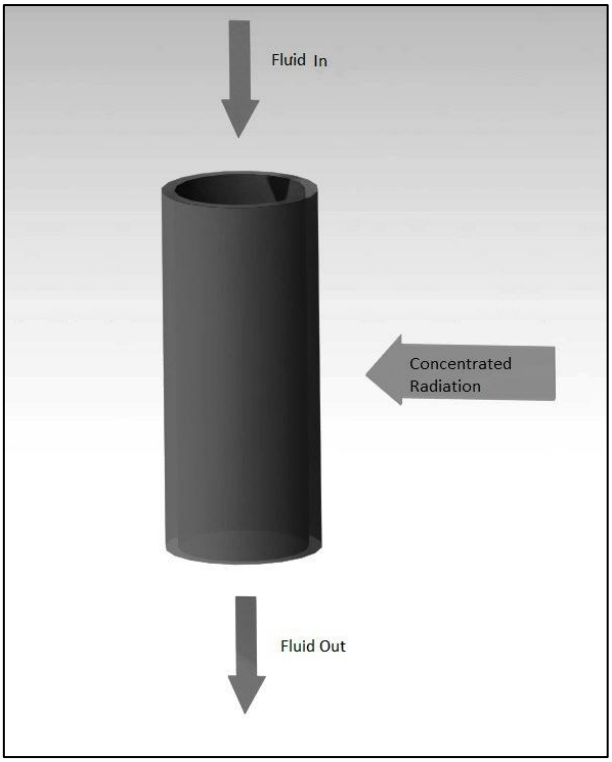

Fig. 1.3: Heat transfer mechanism in a tubular receiver

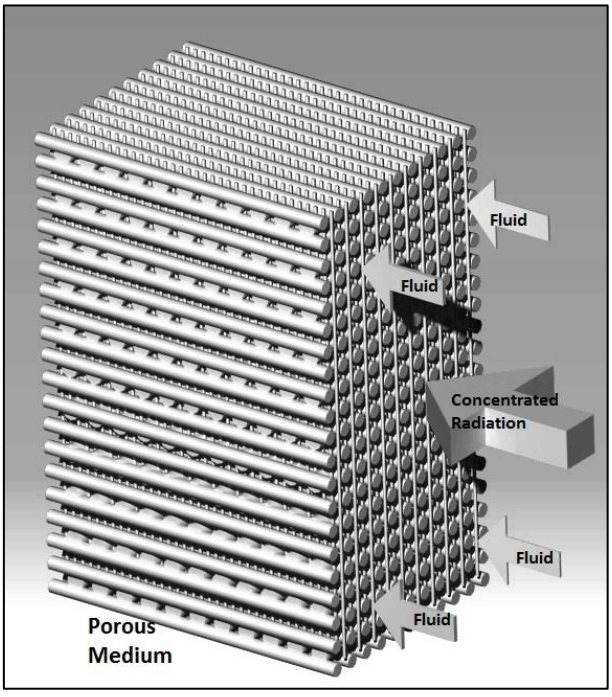

Fig. 1.4: Heat transfer mechanism in a volumetric receiver

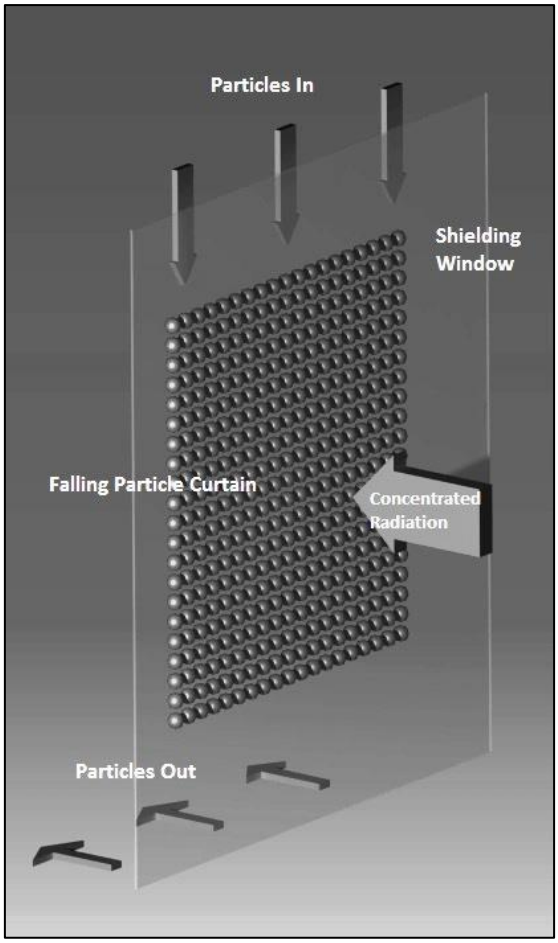

Fig. 1.5: Heat transfer mechanism in a falling particle receiver

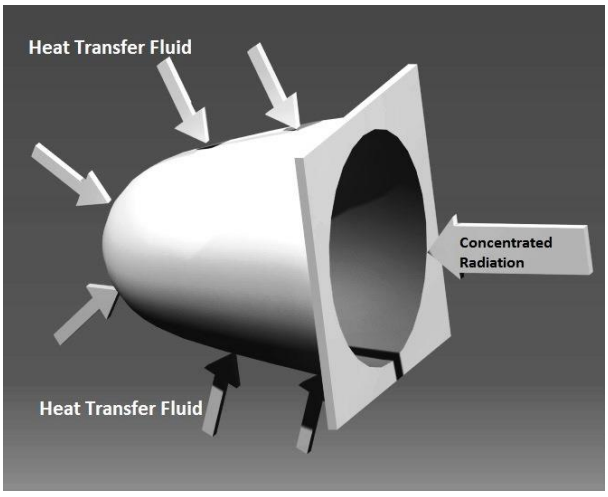

Fig. 1.6: Heat transfer mechanism in a cavity receiver

1.4. HEAT TRANSFER CHALLENGES AND ISSUES FOR s-CO_2 RECEIVERS

As mentioned earlier, many researchers have predicted high power cycle efficiency values for the s-CO_2 closed Brayton cycle with operating pressure around 20 MPa. In the case of a tubular receiver, a substantial thickness for the tube walls is required to sustain these high pressures. The wall thickness has a direct impact on the allowable heat flux. In general, thinner tubes can sustain a larger heat flux due to the lower value of conduction resistance [1]. The use of nickel based super alloys such as Inconel 625, Inconel 617 and Haynes 230 is essential for employing a small thickness while sustaining the high pressure and temperature for extended durations.

As discussed earlier, a pressurized volumetric receiver which uses s-CO_2 as the working fluid would require a transparent window with a high pressure high temperature sealing to prevent the pressurized s-CO_2 from leaking outside the receiver, and to allow the radiation to impinge on the porous volume to obtain volumetric absorption of the concentrated solar energy. While there may be direct absorption of the high intensity radiative energy passing through the window, the window receives additional thermal energy by virtue of re-radiation from the hot absorber emission in addition to convection and radiation emission from the hot flowing s-CO_2. Cooling of this window and ensuring a high temperature pressurized sealing is a humongous challenge for execution of a volumetric receiver for s-CO_2.

The falling particle receiver provides an opportunity to easily store the collected thermal energy and operate the receiver at nearly atmospheric pressure. Designing and maintaining the curtain of falling particles with a precise control of the particle temperatures is very challenging. While the particle receiver technology itself is quite immature and the dynamics of operation are not well understood yet, the design of an effective heat exchanger for energy exchange between the particles and high pressure s-CO_2 is also a subject of research.

All receiver configurations typically require an absorber coating on the irradiated surface to absorb a large fraction of the solar radiation while minimizing the reflection losses. Selvakumar and Barshilia [2] have reviewed high temperature absorber coatings stable up to 900 K. While these coatings exhibit stability in vacuum, exposure to air reduces the temperature up to which the coatings are stable. The behavior of these coatings at higher temperatures and in presence of s-CO_2 is not known, such a situation may occur in a s-CO_2 volumetric receiver configuration. For s-CO_2 receivers with a target outlet temperature of

1000 K, the coating must be stable up to 1300 K. High temperature absorber coatings such as Pyromark 2500 have been demonstrated up to 1300 K, but these coatings also exhibit a total emissivity as high as 0.89, thus having a large radiative loss [3].

With regards to the preceding discussion, it is evident that a tubular receiver configuration is most suitable for direct heating of s-CO_2. At scales of interest which range from few 100 kW's to few MW's and for the desired fluxes and temperatures, use of the central tower technology is necessary and appropriate. An outline of the remaining chapters in this thesis is as follows:

- Chapter 2 presents a brief literature review of CSP plants and previous experiences with the tubular receiver configuration.
- In chapter 3, effect of the participating nature of s-CO_2 on the heat transfer equipment design is explored by studying the absorption by s-CO_2 using the limited optical property data which is available. Radiation-convection interaction for a developing flow for heat transfer from the tube wall to s-CO_2 has been discussed.
- In chapter 4, traditionally neglected radiative emission by s-CO_2 is explored and a first-of-its-kind novel measurement of total emissivity of s-CO_2 is presented.
- In chapter 5, a novel methodology for coupled optical-thermal-fluid analysis of a tubular receiver is presented and used for detailed design of the s-CO_2 tubular receiver panels. Parametric studies for various geometric arrangements, field optics and flow configurations are presented and a feasible design of tubular receiver panels for s-CO_2 is obtained.
- In chapter 6, modelling, manufacturing and testing of the s-CO_2 tubular receiver panels designed in chapter 5 is presented using compressed air as the heat transfer fluid to test and demonstrate the receiver; and to validate the modelling. A recently proposed novel arrangement of receiver panels, called as a bladed receiver configuration is adopted for this purpose.
- Chapter 7 presents a summary of the main conclusions from the studies presented in this thesis.

2. LITERATURE REVIEW

2.1. OVERVIEW OF CSP TECHNOLOGIES

As discussed in chapter 1, CSP technologies are classified based on the manner in which solar energy is focussed on the absorbing element. A summary of the key aspects of the four technologies (parabolic trough, central receiver, linear Fresnel and dish) is provided in table 2.1, reproduced from Behar et al. [4].

Table 2.1: Key aspects of CSP technologies [4]

	PARABOLIC TROUGH	**CENTRAL RECEIVER**	**LINEAR FRESNEL**	**DISH**
Solar collector	Line focus	Point focus	Line focus	Point focus
Solar receiver	Mobile	Fixed	Fixed	Mobile
Power conversion cycle	RC, CC	RC, BC, CC	RC	RC, SC
Concentration ratio	70-80	> 1000	> 60	> 1300
Solar field slope (%)	< 1-2	< 2-4	< 4	10 or more
Working temperature (^{0}C)	Medium	Higher	Relatively Lower	Highest
Current efficiency (%)	15-16	16-17	08-10	20-25
Plant Peak efficiency (%)	14-20	23-35	18	30
Typical capacity (MW)	10-300	10-200	10-200	0.01-0.025
Annual capacity factor (%)	25-43	55	22-24	25-28
Development Status	Commercialized	Commercialized	Pilot	Demonstration
Technology development risk	Low	Medium	Medium	Medium
Outlook for improvements	Limited	Very significant	Significant	Via mass production only
Efficiency with improvements	18	25-28	12	30
Relative rise of efficiency after improvements (%)	20	40-65	25	25

The overall efficiency of the CSP plant using any of the four technologies varies with the receiver configuration, location of the CSP plant, hour of the day and particular time of the year. For every technology, there is a range of possibilities of the receiver configurations, concentrator field design and associated tracking mechanisms, heat transfer fluids (HTFs), storage technologies and thermal-to-electric conversion systems. North–south or east–west orientation of the parabolic troughs with single-axis tracking is usually employed in the parabolic trough based solar field [5]. For the central tower technology, surround field and north facing fields are the possible configurations [6]. While the parabolic trough and linear Fresnel technologies use linear receivers, i.e. tubes through which fluid flows, various receiver configurations discussed in chapter 1 are used for the central tower and dish based CSP plants. Many high temperature receivers based on the volumetric, particle and cavity receiver configurations are recently proposed and developed around the world [7-10]. With reference to heat transfer fluids, molten salt and steam are the most widely used HTFs in commercial plants. Synthetic oils are also considered as potential HTFs for commercial plants operating at moderate temperatures. High pressure air and various other gases (such as carbon dioxide and nitrogen), nano-fluids, circulating particles are being studied for use in the parabolic trough and central tower technologies, while helium is a potential fluid for use in dish technology coupled with a Stirling engine [11–13].

For thermal energy storage after heating the fluid in a CSP plant, liquid molten salt based thermal storage is popular for long term storage, while steam and metal based storage systems are popular for relatively short-term storage [14, 15]. Phase change based storage and thermochemical storage are other potential storage options for thermal energy storage in CSP plants [14–16]. The Rankine cycle, Brayton cycle and combined cycles are the popular thermodynamic cycles for parabolic trough, central tower and linear Fresnel types of CSP plants, while the Stirling cycle is the most popular one for use with the paraboloid dish technology. Advanced Brayton cycles using s-CO_2 and pressurized air as the working fluid and Rankine cycle based CSP plants using supercritical steam as the working fluid are under development, and have made considerable progress in the past few years resulting in potential enhancement in the power block efficiencies.

Among the four CSP technologies, the power tower or central receiver system (CRS) configuration is at the forefront; it is the technology of choice at present [17]. The reason for this choice is the scope for performance enhancement and price decline with technology

advances of its component systems, which are the reflectors (heliostats), the solar receiver and the associated thermodynamic cycles. CRS offers the following potential features-

- High temperatures ~ 1300 K and resulting greater conversion efficiency of the thermodynamic block [5];
- Easy integration with conventional fuel based power plants and hybrid operation with capability of achieving high power plant capacity factors (0.4- 0.8), by employing high temperature thermal energy storage systems [5];
- Large potential for reduction in costs and improvement in efficiency (40–65%) [5].

2.2. CENTRAL RECEIVER SYSTEM (CRS) BASED PILOT PLANTS

The CRS configuration has been demonstrated and has been seeing continuous improvements and innovations since early 80's. With the successful demonstration of many pilot plant projects like Solar Two (improvement of Solar One), the CESA1 and TSA from Spain, and the THEMIS plant from France, the power tower technology is one of the leading renewable energy harnessing technologies [18]. The most pertinent pilot power tower plants are reported below (table 2.2), reproduced from reference [4].

Table 2.2: Pilot CRS plants in 20th century [4]

Project	Capacity MW	Country	Starting Year
SSPS	0.5	Spain	1981
TSA	1	Spain	1993
CESA-1	1	Spain	1983
Solar One	10	USA	1982
MSEE/Cat-B	1	USA	1984
Solar Two	10	USA	1996
THEMIS	2.5	France	1984
EURELIOS	1	Italy	1981
SUNSHINE	1	Japan	1981
SPP-5	5	Russia	1986

These pilot CRS projects proved the viability as well as cost-effective prospective of the central tower configuration. These pilot plants have set benchmarks and given directions for enhancement in the design process of various power tower system components, exploration of hybridization concepts and innovations in the field of HTFs and thermal storage systems.

2.3. CENTRAL RECEIVER SYSTEM (CRS) BASED PLANTS IN OPERATION

Water/steam was initially used in some CRS plants such as PS10, PS20, Beijing Badaling, Sierra and Yanqing. Due to high conductivity, nitrate based molten salt used in Gemasolar plant is also a very commonly used HTF. Use of air as the heat transfer fluid (e.g. Julich solar power plant) has received considerable attention recently.

Based on the choice of HTF and receiver configuration, exit temperatures ranging from 550 K (for water/steam) to 800 K (present molten salt designs) can be obtained. Use of Direct Steam Generation (DSG) as the configuration for heating water as the HTF is promising with respect to cost reduction and augmentation of the plant efficiency owing to exclusion of the heat exchanger set-up [19, 20].

In 2006, Abengoa Solar built the PS10 in Sevilla, Spain. It was a CRS power with 11 MW_e rating. Subsequently, a 20 MW_e capacity CRS plant (PS20) was built adjacent to PS10. In 2009, a 5 MW system called Sierra Sun Tower was commissioned in Lancaster, USA, while the 1.5 MW air based system was built in Julich, Germany. The Gemasolar CRS plant (Spain) with surround heliostat field and 15 hrs of external thermal storage has been functioning and providing electricity round the clock since 2011 [20]. Following the three leading nations in CSP technologies, namely Spain, USA and Germany, China has joined the CSP community by executing the Beijing Yanqing plant in 2010. In 2012, China followed it with Beijing Badaling Solar Plant. The 330 MW CRS based plant at Ivanpah, California USA is the largest operational CSP plant around the world, with even bigger projects in planning and construction stage. Some of the key currently operating CRS power plants are reported below (table 2.3).

Table 2.3: Some central receiver based solar thermal power plants [4]

Name	Country, Location	Owners	Capacity (MW)	Heliostat field area (m^2)	Power cycle	Storage	Type
Beijing Badaling	China Beijing	Academy of sciences	1.5	10,000	Rankine	1 h	Fossil-solar
Gemasolar	Spain, Andalucia (Sevilla)	Torresol energy	19.9	304,750	Rankine	15 h	Fossil-solar
Jùlich	Germany, Jùlich	DLR	1.5	17,650	Rankine	1.5 h	Fossil-solar
Planta solar 10	Spain, Sanlúcar, la mayor, (Sevilla)	Abengoa solar	11.0	75,000	Rankine	1 h	Fossil-solar
Planta solar 20	Spain, Sanlúcar, la mayor, (Sevilla)	Abengoa solar	20.0	150,000	Rankine	1 h	Fossil-solar
Sierra	United States Lancaster California	eSolar	5.0	27,670	Rankine	-	Solar only
Yanqing	China, Yanqing country	Academy of sciences	1	10,000	Rankine	2-stage	

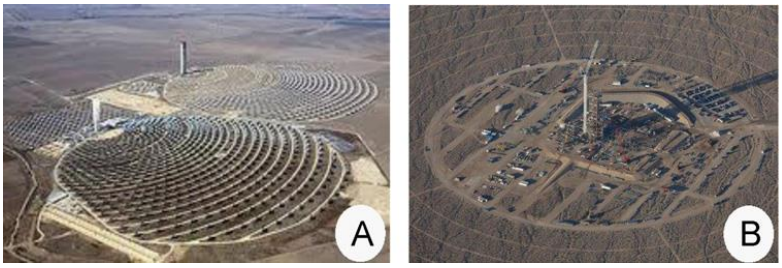

Fig. 2.1: (A) PS10-PS20 (front) in operation near Seville, Spain [21], (B) Ivanpah plant during the under construction stage [22]

Fig. 2.2: Solar One, Barstow, California [23]

Fig. 2.3: Beams visible due to dust at PS10, Seville, Spain [24]

2.4. CHALLENGES AND BENEFITS OF VARIOUS RECEIVER DESIGNS

Ho and Iverson [25] have provided an excellent review of existing high-temperature solar receiver configurations and technologies which can be used in the central receiver systems. Although many innovative receiver concepts have been proposed till date, only a small number of ideas have been implemented practically with large scale demonstration in a central receiver based power plant. A tubular receiver employing air, molten salt or steam as the HTF is the most common configuration. For obtaining high overall power plant efficiency, design of efficient higher temperature receivers is of utmost importance. A reasonable, yet challenging approach is to improve current receiver designs for usability at elevated temperatures with newly emerging HTF candidates such as s-CO_2. The resurgence of particle based receivers is also observed in the last decade. However, particle conveyance, abrasion, and heat exchange with working fluid of the power cycle remain challenges to overcome.

Air receivers have exhibited the highest receiver exit temperatures till date, but suffer from the disadvantage of low thermal conductivity and heat capacity of air, and the requirement of an additional heat exchanger and means for thermal energy storage. Table 2.4, reproduced from Ho and Iverson [25], provides a succinct summary of the receiver types and advantages/challenges related to each configuration. For liquid or gas HTFs, tubular receiver configuration is most promising for CSP plants. For solid particle receivers, the receiver designs still need substantial technological maturity, and efforts are ongoing for improving the efficiency and overall heat transfer performance of particle receivers.

Table 2.4: Summary of Receiver Designs [25]

Receiver Design	Outlet Temperature / Thermal Efficiency	Benefits	Challenges / Research Needs
Gas Receivers			
Volumetric Air Receiver	>700°C / ~50 – 60%	Capable of achieving high temperatures, simple and flexible construction	Material durability, flow instability, radiative heat loss, low thermal efficiency, long- term storage
Small Particle Air Receiver	>700°C / ~80 – 90% (theoretical)	Capable of achieving high temperatures, volumetric gas absorption of energy	Requires window for pressurized receivers, solid-gas suspension system to Maintain desired particle concentration and temperature, long-term storage
Tubular Gas Receiver	>800°C / ~80 – 85% (theoretical) ~40% (prototype Test)	Capable of achieving high temperatures and gas pressures; heat-pipes can provide effective and compact heat transfer to gas	High radiative and convective heat loss, low thermal efficiency, need improved heat transfer from irradiated tubes to gas, material durability, long-term storage
Liquid Receivers			
Tubular Liquid Receiver	>600°C / ~80 – 90%	Contained liquid; demonstrated performance; can accommodate potentially high pressures	Thermal expansion; material compatibility; increased pressure requirements to manage pressure drop across receiver panel; potential for tube solidification and plugging
Falling Film Receiver (Direct Exposure)	>600°C / 80-90% (experimental) ~94% (theoretical)	Higher receiver outlet temperatures; reduced thermal resistance and startup time through direct absorption; lower pumping losses	Film stability in exposed environments; complexity of rotating body; fluid impurities and integrity in exposed environments; absorber wall flatness during thermal expansion.
Falling Film Receiver (Indirect Exposure)	>600°C/ >80% (theoretical)	Reduced pumping losses; faster response time; capability of operation at lower insolation; simplicity of fabrication; no need for fluid doping	Film stability and potential for dry spots; absorber wall flatness/shape integrity; flow distribution across illuminated surfaces to match incident flux; thin sheet warping during thermal expansion; thermal loss reduction and efficiency improvement by exploring hybrid cavity/external receiver concepts.
Solid Particle Receivers			
Falling Particle Receivers	>800°C / ~80% (simulation), 50% (prototype)	Capable of achieving high temperatures, direct irradiance of particles reduces flux limitations (on tubular receivers), particles can be stored at high temperatures, particles can be cheaper than molten salt	Need lower radiative and convective heat losses, higher concentration ratios, lower particle attrition, greater solar absorptance, lower thermal emittance, increased particle residence time, more effective particle/fluid heat exchangers

2.5. LITERATURE ON TUBULAR RECEIVERS

Solar thermal receivers for high-temperature air-Brayton cycle have been under development since 1970's, and there has been continuous development and testing of new prototypes. The earliest receiver designs employed liquid metal heat pipes to enhance the heat transfer coefficient of receivers associated with parabolic dish concentrators [26]. Use of liquid metal heat pipes results in very high heat transfer coefficients (~30,000 W/m^2K), but the limitation of these receivers is efficient exchange of heat from liquid metal to air with heat transfer coefficients as low as 300 W/m^2K for gases [26]. Heat pipe based tubular receivers are capable of handling very high heat fluxes, resulting in compact receivers with low temperatures and moderate pressure drop, and were designed for delivering air at temperatures as high as 1100 K, albeit at a very low flow rate of air and extremely high cost of the receiver [26].

DLR (Germany) has proposed and tested many new central receiver design concepts in recent years. Design improvements such as sandwiching of copper tube in the annulus between two Inconel tubes for enhancement of the circumferential heat distribution, use of segmented quartz window cut out of circular tubes to arrest the radiative and convective losses, and an integrated air-turbine with the receiver are some of these innovations (figure 2.4). DLR used a micro-turbine system in conjunction with the receiver to demonstrate operation at different power scales in the range 100 kW - 1 MW [27-31].

While the simulations presented by DLR predicted enhancement of receiver thermal efficiency from 68% to 81% due to the use of segmented window, demonstration tests at the Plataforma Solar de Almeria showed a lesser improvement, where the receiver efficiency increased to 43 % from 40% due to use of a window. The smaller power input compared to design conditions resulted in large heat losses and lesser efficiency than predicted by their simulations.

Tubular receivers are subjected to large convective and radiative heat losses. In the event of rapid variation in the heat input, the receiver walls can be subjected to large thermal stress values due to rapid changes in receiver wall temperatures, affecting the receiver life-span. Uhlig [32] experimented and proposed models to accurately predict reliable lifetime of tubes manufactured from nickel alloys subjected to fatigue and temporal thermally induced stress. Kolb collected fatigue data for various super alloys such as Haynes 230, Incoloy 800 and

Inconel 625 to determine the maximum permissible heat flux on circular tubes made of these metal alloys aimed at operation in a molten-salt based central receiver [33].

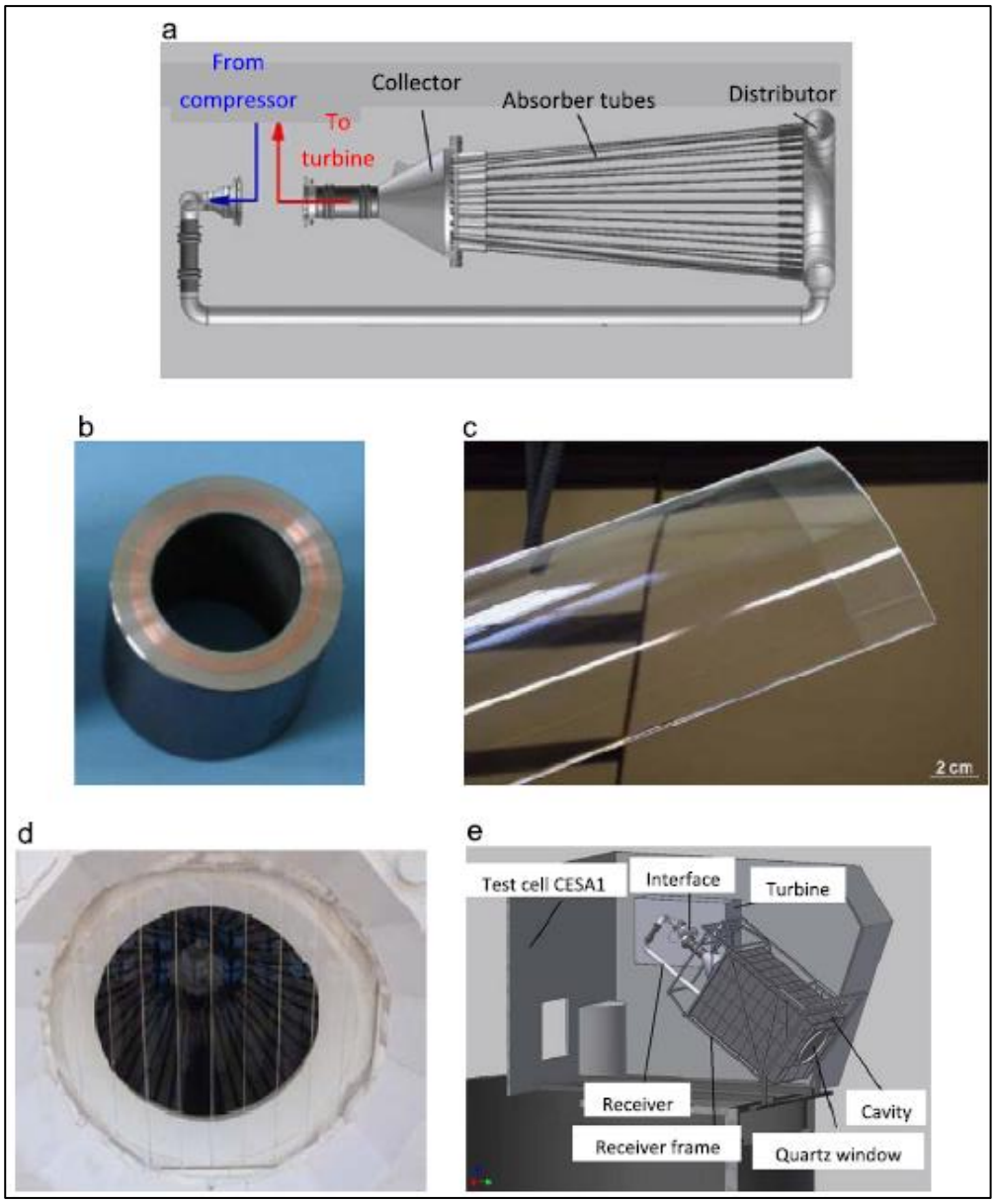

Fig. 2.4: Design innovations from DLR [29-31]: a) Tubular air-turbine receiver, b) multi-layer copper/ Inconel tube, c) and d) segmented parts of glass tubes to form a window on the receiver aperture, and e) schematic of receiver and micro turbine on top of a tower

Tubular receivers for s-CO_2 seem to be feasible because of the small diameter requirement owing to smaller volumetric flow rates (due to larger density and specific heat) compared to air, thus enabling high pressure operation. For thermal energy storage, s-CO_2 cannot be stored directly, as it is in the supercritical phase and not a viable option [34], thus needing an external storage medium and an additional heat exchanger for incorporating a thermal storage system.

Tubular central receiver systems which use liquids as the heat transfer fluid were investigated starting in the 70's and the first demonstrations happened in the 80's and 90's with the Solar One and Solar Two [35, 36] projects. These liquid tubular receivers conventionally operate at a much lower pressure and temperature as compared to the s-CO_2 receiver targets, and are built out of stainless steel tubes. Liquid based tubular receivers employing molten salt as the working fluid have been studied in detail at Sandia National Laboratories [37, 38], Plataforma Solar de Almeria [39] and Themis [40]. These receivers operate at a maximum receiver outlet temperature around 900 K. This is primarily due to the limitation on temperatures that molten salts can handle. Liquid sodium [41] and fluoride-salt [42] based HTFs are being evaluated as alternatives to conventionally used molten nitrate salts for operation at larger fluxes and temperatures, leading to better efficiencies. High values of thermal conductivity of liquid metals usually allow use of larger incident radiation heat fluxes on the receivers, as compared to gases [41]. Larger impinging heat flux values result in improved receiver efficiency as a lesser area is required for identical energy collection at the aperture.

For optimum size of the tubes in a receiver, the diameter and wall thickness need to be such that the heat transfer is maximized while the pressure drop is least. Unfortunately, while the convection heat transfer coefficient for any HTF increases with reduction in diameter, so does the pressure drop. Hence a trade-off exists between these two effects and optimization of tube size can be done [43].

Estimated efficiencies for external tubular receivers which employ different HTFs indicate receiver thermal efficiencies above 85 % [44, 45]. Solar Two receiver tests showed efficiency as high as 90 %. Use of a solar selective absorber coating can result in significant reduction in radiative losses and boost the efficiency to the desired target values [33, 46, 47]. These coating have high absorptivity in the solar spectrum and low emissivity at wavelengths where the hot metal tubes emit.

In general, receivers using liquid HTFs exhibit higher heat transfer coefficients due to better thermal conductivity and specific heat, compared to gaseous HTFs. A large number of HTFs have been demonstrated in power tower plants, such as steam [48], nitrate salts [35], and liquid sodium [39]. Water based plants at high temperatures were demonstrated at numerous plants, for instance Solar One, PS10, PS20 and Ivanpah. Conventional steam cycles typically operate at turbine inlet pressures up to 10 MPa [41]. Solar Two demonstrated a tubular receiver using molten salt as the HTF, capable of convecting flux up to 850 kW/m^2, while Solar One could accommodate fluxes up to 300 kW/m^2 [49]. Using molten salts as the HTF is an attractive prospect due to direct storage of molten salt, removing an intermediary heat exchanger for employing a thermal storage. A significant limitation for using nitrate salts is the dramatic decomposition of salts as the temperature increases above 800 K [50]. In the case of liquid sodium as the HTF, reaction with oxygen and leaking is a concern. Cavity-type receivers generally exhibit lower radiative losses, in comparison to external tubular receivers, but have higher convective losses [51] and are more complicated from control and operation point of view.

Surround field systems and north-facing fields have been studied and deployed in the past and it was found that surround field towers are usually shorter than north-field design towers. However, surround fields require a larger land area than north-facing fields. Selective absorber coatings that enhance the solar absorption while minimizing thermal re-radiation emittance can result in significant thermal efficiency augmentation. High temperatures stability, great durability for a large number of receiver cycles, cost-effectiveness and ease of use are some key requirements of a good coating. Commercially offered high-temperature coating Pyromark 2500 was studied by Ho et al. [3] and Persky et al. [52]. Several glazing materials and novel application methods were studied for high temperature solar applications in the literature [53, 54], but continuous and reliable operation for temperatures targeted by s-CO_2 receivers has not been demonstrated yet.

3. RADIATIVE HEATING OF SUPERCRITICAL CARBON DIOXIDE FLOWING THROUGH TUBES

3.1. INTRODUCTION

A closed Brayton power cycle using supercritical carbon dioxide (s-CO_2) as the working fluid is considered as a promising candidate for solar-thermal power plants. Numerous configurations of heat exchangers and solar receivers to be used with s-CO_2 are being developed, with predicted tube wall temperatures greater than 1000 K. Detailed knowledge of the heat transfer characteristics of s-CO_2 is required for precise and optimum design of heat transfer equipment for the s-CO_2 Brayton cycle. Niu et. al. [55] and Kim et. al. [56] have carried out experimental study of heat transfer for s-CO_2; while there are many investigations in the literature which employ numerical modeling for design of heat transfer equipment using s-CO_2 as the working fluid.

All the studies evaluating heat transfer for s-CO_2 have assumed that s-CO_2 is transparent to radiation heat transfer, i.e., it is a non-participating medium. The inclusion of radiation heat transfer modelling to evaluate the effect of absorption of s-CO_2 and the radiative heat transfer among the equipment surfaces makes the simulations more complex. Despite the high temperatures, radiation heat transfer in s-CO_2 is often ignored on the assumption that convection is the dominant transport mechanism.

The intensity of thermal radiation emitted by a surface at any temperature T (K) peaks at a wavelength λ_{max} (m), as governed by the well-known Wien's displacement law of thermal radiation:

$$\lambda_{max} T = 2.89 * 10^{-3} \text{ m-K} \qquad (\ldots \text{Eqn. } 3.1)$$

Carbon dioxide at room temperature and pressure is largely transparent to solar irradiation (figure 3.1). The solar irradiation intensity peaks at a wavelength of 0.5 μm, in accordance with the sun's surface temperature and Wien's displacement law. First observed by Fourier in

1827 [57], CO_2 is now a well acknowledged greenhouse gas due to its ability to absorb radiation emitted by the earth's surface, i.e. long wavelength radiation. The intensity of thermal radiation emitted by the earth's surface is largest near 10 μm, as per the Wein's displacement law.

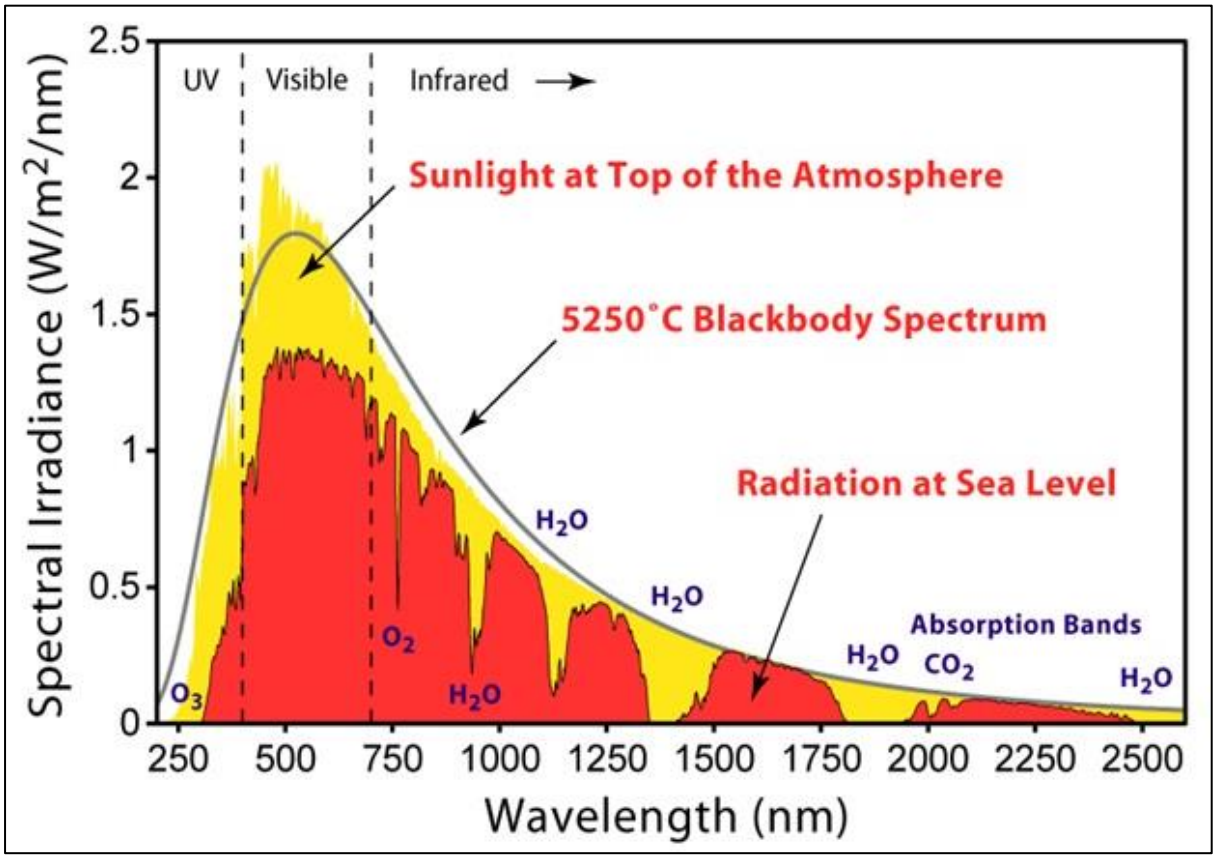

Fig. 3.1: Solar Radiation Spectrum [21]

For a tubular solar receiver or a heat exchanger with wall surface temperatures around 1000 K, the peak intensity of emitted radiation from these walls occurs at a wavelength of approximately 3 μm. While atmospheric CO_2 is largely transparent to the solar irradiation spectrum which peaks at 0.5 μm, the absorption may be significant for radiation spectrum emitted by walls of heat transfer equipment through which CO_2 flows. Such an absorption effect may also be expected for supercritical CO_2, but has traditionally been ignored in the literature. If the absorption is significant, it will alter the temperature distribution inside the heat transfer equipment and influence its design.

Evaluation of the absorption by s-CO_2 is challenging because of the large computational expenses for radiation modelling in a participating medium, as well as non-availability of data on radiative properties of CO_2 at elevated pressure and temperature. With increase in temperature and pressure of CO_2, modification in the absorption behaviour can be anticipated due to alteration in the molecular vibration frequencies. Line-broadening and lateral shifting of the absorption bands due to elevated conditions can be expected, but these effects for CO_2 in supercritical state are unknown.

For reasons discussed above, it is important to study the effect and contribution of radiative heat transfer for s-CO_2, in conjunction with its outstanding convection heat transfer capability. Caliot and Flamant [58] have studied the influence of radiative heat transfer for turbulent flow of s-CO_2 through circular tubes, and have recommended that for highly turbulent flows, radiative heat transfer can be neglected.

In this chapter, a numerical study will be presented for characterizing the heat transfer in a developing laminar flow of s-CO_2 through a circular tube. Such laminar flow of s-CO_2 typically occurs in a printed circuit heat exchanger (PCHE), used as a regenerator in s-CO_2 Brayton cycle power plants. It can also occur in tubular solar receivers for certain geometric and operating conditions. In the present numerical work, laminar flow of hot s-CO_2 in a circular tube is subjected to a constant heat flux boundary condition. Fundamental discussion on effect of radiation heat transfer towards altering the velocity and temperature profiles is presented and the effect of radiation on the overall transport of momentum and energy is evaluated. The combined effect of convection and radiation is studied for various flow conditions and geometric circumstances. The role of total internal emissivity and total imposed heat flux on the contribution of radiation heat transfer is also observed and discussed in this chapter.

3.2. SCOPE OF CURRENT ANALYSIS

The s-CO_2 Brayton cycle is considered as a viable option for large scale as well as distributed small scale applications (~kW to MW) with typical turbine inlet temperature ~1000 K and an operating pressure ~20 MPa, with predicted cycle thermal efficiency ~50 %. In this study, developing laminar flow of hot s-CO_2 through circular tubes subjected to a constant heat flux

is studied using the numerical solver ANSYS Fluent. The present study is focused on flows within the laminar regime, such that the contribution of radiative transport towards the overall heat transfer (convection + radiation) remains significant. For highly turbulent flows, i.e. large Reynolds number flows, it is possible that convection will always dominate over radiative heat transfer, rendering it possibly safe to ignore the radiation heat transfer interaction of s-CO_2 [58].

The intent of this study is to look at radiation-convection interaction for a developing flow while providing a guideline for future researchers regarding the conditions for which radiative heat transfer modelling for flow through tubes is critical, and what errors can be expected if s-CO_2 is considered as a completely non-participating medium. The effect of parameters such as Reynolds number (Re), pipe geometry, internal wall emissivity and magnitude of total wall heat flux will be discussed briefly. The effect of radiation modelling on the resulting wall temperature is also examined. This data is important, as the tube wall temperature affects the estimation of heat loss to the environment in the case of solar receivers; and also plays a major role in deciding the material to be used to manufacture the heat exchanger/receiver.

The only source of data for s-CO_2 absorption spectrum that could be found in the literature is the HITRAN compilation and its associated database HITEMP [59, 60]. The high temperature, high pressure absorptivity by CO_2 in this database is largely based on analytical estimates. Also, there seems to be a limitation on the highest pressure of CO_2 (10 MPa) for which reliable data can be obtained from this database. As a consequence, the absorptivity data for s-CO_2 at 623 K and 10 MPa is obtained from this database and used to evaluate radiation heat transfer contribution towards transferring the total heat flux imposed on the tube surface.

3.3. COMPUTATIONAL FLUID DYNAMICS MODELLING

3.3.1. Problem Statement

Supercritical CO_2 entering the circular tube is heated by a few hundred Kelvin, depending on the applied external heat flux on tube surface and the flow Reynolds number. For an inlet temperature of 623 K, the inner wall of the tube can have peak temperature as high as 1100-

1200 K. The inner wall of the tube emits thermal radiation within the tube, which occur over a range of wavelength in the form of a temperature dependent spectrum. The peak wavelength (wavelength at which the intensity of emission peaks, λ_{max}), is inversely proportional to the wall temperature, and is governed by Wien's displacement law [61].

Based on whether or not s-CO_2 has effective radiation absorption bands at wavelengths around λ_{max}, the effect of radiative heat transfer may or may not be worth considering. If radiation plays a noteworthy role and aids convection for transfer of heat from wall to s-CO_2, it will result in better dispersion of thermal energy along the radial direction, leading to thickening of the thermal boundary layer and affecting temperature distribution of the tube wall and flowing s-CO_2. This change in the temperature distribution then affects the convection heat transfer and an iterative procedure is required to predict the steady state temperature distribution and the relative contribution of radiation heat transfer from the tube to s-CO_2, when compared to convection heat transfer.

For transferring the same amount of heat from the tube surface to s-CO_2, if the radiative participation of s-CO_2 results in an enhancement in the overall heat transfer coefficient, the average temperature difference between the tube wall and s-CO_2 will be lowered in comparison to the 'convection-diffusion only' case, resulting in less stringent material requirements and lower thermal losses to the environment

3.3.2. Geometry and modelling details

A 2-dimensional axisymmetric section of the tube (shown in figure 3.2) is modelled and meshed in ANSYS ICEM CFD. The two geometric parameters, namely the length (L) of the tube and diameter (D) of the tube are varied from case to case; L has been varied from 80 mm to 600 mm, and D has been varied from 8 mm to 16 mm. Uniform heat flux (5 kW/m^2, 10 kW/m^2) boundary condition is applied on the outer wall of the tube, and the tube thickness is ignored. Velocity inlet and pressure outlet boundary conditions are specified for the tube inlet and tube outlet, respectively.

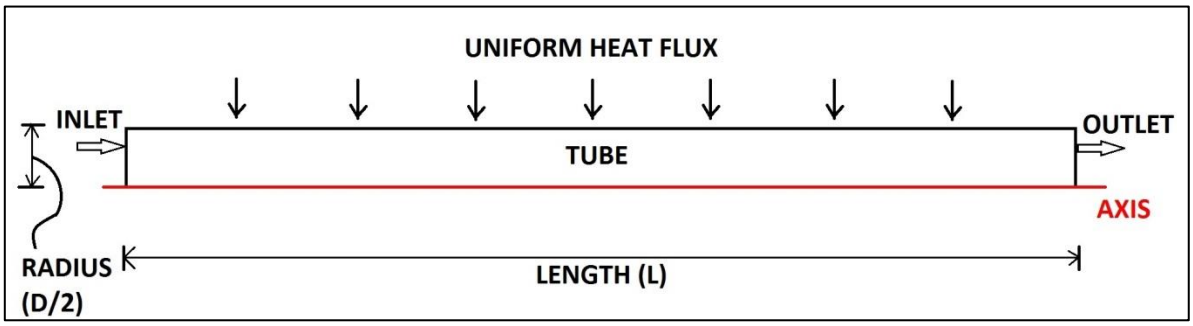

Fig. 3.2: Geometry and boundary conditions

A non-uniform structured quadrilateral mesh is generated by using the 'blocking' methodology in ANSYS ICEM CFD and the grid size is distributed in such a manner that it is coarsest at the core of the flow and finest (most refined) near the tube wall. Grid independence study is implemented and the mesh is refined until doubling the grid points yielded less than 0.2% variation in the solution parameters.

Coupled and discretized conservation equations for transport of mass, momentum, energy and radiation (Discrete Ordinates Method (DOM)) are solved by ANSYS Fluent, which uses the finite volume method to discretize the transport equations [62]. The steady state, pressure based solver using SIMPLE algorithm for the pressure velocity coupling and second-order upwind for spatial discretization is used for the simulations. Mass and energy imbalance along with the scaled residuals are continuously monitored as the solution advanced, and convergence is assumed when the quantities of interest exhibit negligible variation and the scaled residuals for all equations drop below at least 10^{-3}.

To obtain accurate thermo-physical properties for s-CO_2, Fluent is linked to REFPROP, which is a database provided by NIST [63]. The equation of state for CO_2 provided by Span and Wagner is used by this database [64]. During every iteration of the numerical solution and for each computational point in the domain, the thermo-physical property is obtained from the NIST database before solving the Navier Stokes equations.

The spectral variation of absorption coefficient of s-CO_2 at 10 MPa and 623 K is obtained from HITRAN compilation and its associated database HITEMP. This system uses the line-by-line method for computation of absorption coefficient. A large number of data points for wavelength and corresponding absorption coefficient are obtained from the program. Non-

grey radiation is implemented using the grey-band option in DOM to capture the radiation interaction accurately. The DOM grey-band model in ANSYS Fluent requires a constant value of absorption coefficient within each band. Hence, the data is inspected and 19 unequal continuous bands in the range 0-100 μm are finalized for approximating the absorption by s-CO_2. These bands are tabulated in table 3.1.

The average value for absorption coefficient for each band is calculated using numerical integration over the data points in that range. The methodology for obtaining the absorption coefficients of each band is similar to the 'Band Model' described by Modest [65]. It is apparent that for the values of diameter (D = 8 mm to 16 mm) investigated, the gas is optically transparent in most of the spectrum. However, there are discrete bands (values) where the optical path length given by $a_\lambda D$ is of the order of unity, where a_λ is the absorption coefficient. Radiative participation is likely to be significant in these bands.

The effect of gravity is ignored and s-CO_2 at the 'velocity inlet' boundary is specified to enter at a pressure and temperature of 10 MPa and 623 K, respectively.

Table 3.1: Absorption bands corresponding absorption coefficients for s-CO_2 at 10 MPa and 623 K

Band Number	Wavelength Bands (μm)	Absorption Coefficient (cm^{-1})
1	0-0.25	0
2	0.25-0.86	0
3	0.86-0.91	2×10^{-6}
4	0.91-1	0
5	1-1.1	2×10^{-5}
6	1.1-1.2	1.23×10^{-6}
7	1.2-1.4	4×10^{-5}
8	1.4-1.7	3.09×10^{-3}
9	1.7-1.9	5.58×10^{-4}
10	1.9-2.1	0.128
11	2.1-2.5	5.12×10^{-4}
12	2.5-2.6	0.156
13	2.6-2.9	7.87
14	2.9-4.2	31.5
15	4.2-4.5	533
16	4.5-8.3	6.32×10^{-3}
17	8.3-12.5	0.26
18	12.5-18.2	39.3
19	18.2-100	0.407

3.4. RESULTS AND DISCUSSION

The situation considered here is essentially a combined entry-length problem, in which momentum and thermal boundary layers are developing simultaneously in the presence of radiation. While this has been extensively studied by several investigators, the additional complexity here is the presence of a participating medium. Very few investigators have studied this situation. For a grey gas, Modest [65] has presented the stream-wise variation of the heat transfer coefficient as a function of a conduction/radiation parameter. Most of the

researchers use the constant temperature boundary condition. In this study, the assumption of a constant wall heat flux has important consequences, as discussed below.

To illustrate the effect of participating media, consider a situation specified by Reynolds number equal to 1000, L=120 mm, D=12 mm and diffuse internal tube wall emissivity ϵ=0 or 0.9. The velocity and temperature profiles at discrete location along the length of the tube are shown in figure 3.3 and 3.4, respectively. This model represents a situation where the tube length is shorter than its hydrodynamic development length. For each location, two profiles are plotted: one with no radiative heat transfer, and the other with a participating medium according to the present model. It is apparent that the velocity profiles are not altered perceptibly due to radiation, suggesting that momentum transport is still dominated by convection-diffusion effect. The temperature profiles, however, show a marked difference with and without radiation. The profiles are significantly flatter near the tube wall, leading to a shallower slope and lower convective heat transfer. Since the wall heat flux is uniform into the fluid, the remaining input flux is transferred into the fluid through radiative absorption.

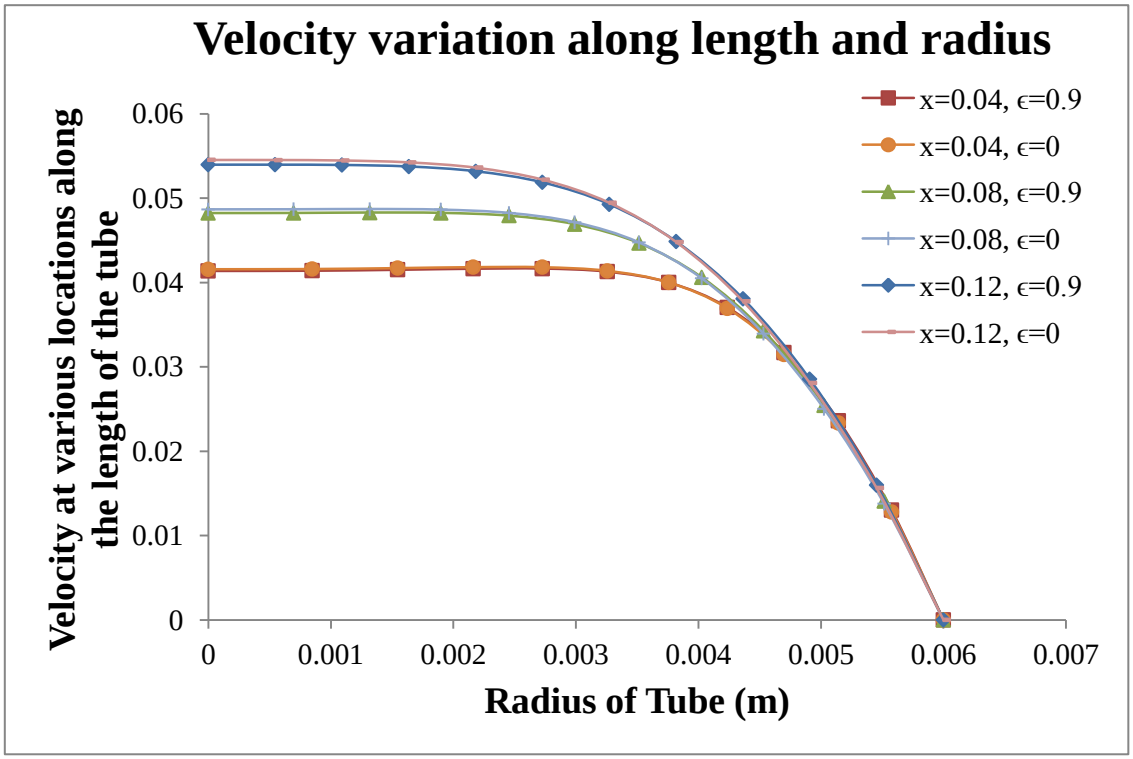

Fig. 3.3: Development of velocity profiles

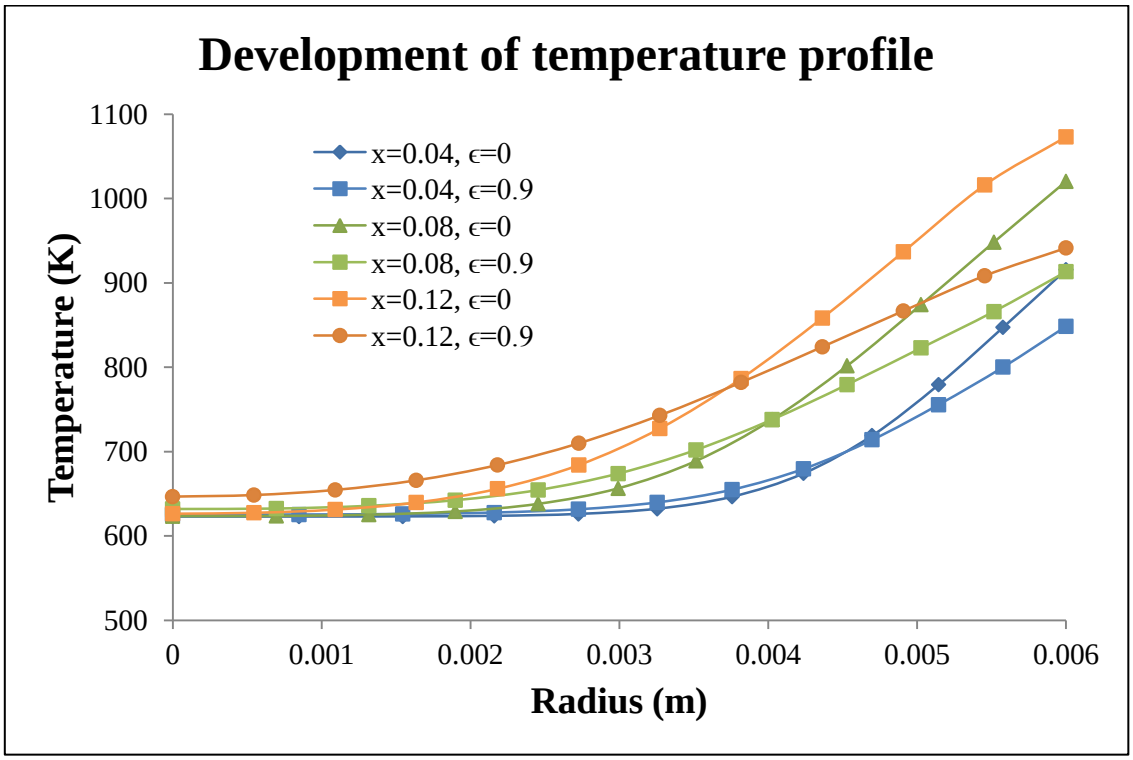

Fig. 3.4: Development of temperature profiles

Depending on whether the gas is optically thick or thin in a band of interest, the absorption will occur close to the wall, penetrate further into the fluid, or will have a significant portion incident on the opposite side. In this case, we notice that as the fluid moves downstream, the temperature smoothening effect begins affecting the centreline temperature as well (refer x=0.12), suggesting that there is significant participation at some wavelength(s). As the fluid moves downstream, radiative transfer increases in significance, contributing to as much as 40% of the overall heat transfer near the tube exit (figure 3.5).

The combined effect of the velocity and temperature profiles, as affected by radiative transport, is reflected in the bulk temperature of the fluid, plotted in figure 3.6. Only a slight effect of radiation is seen here, since the wall heat flux is constant and the effect of radiation is mainly confined to the near-wall regions, where momentum is low.

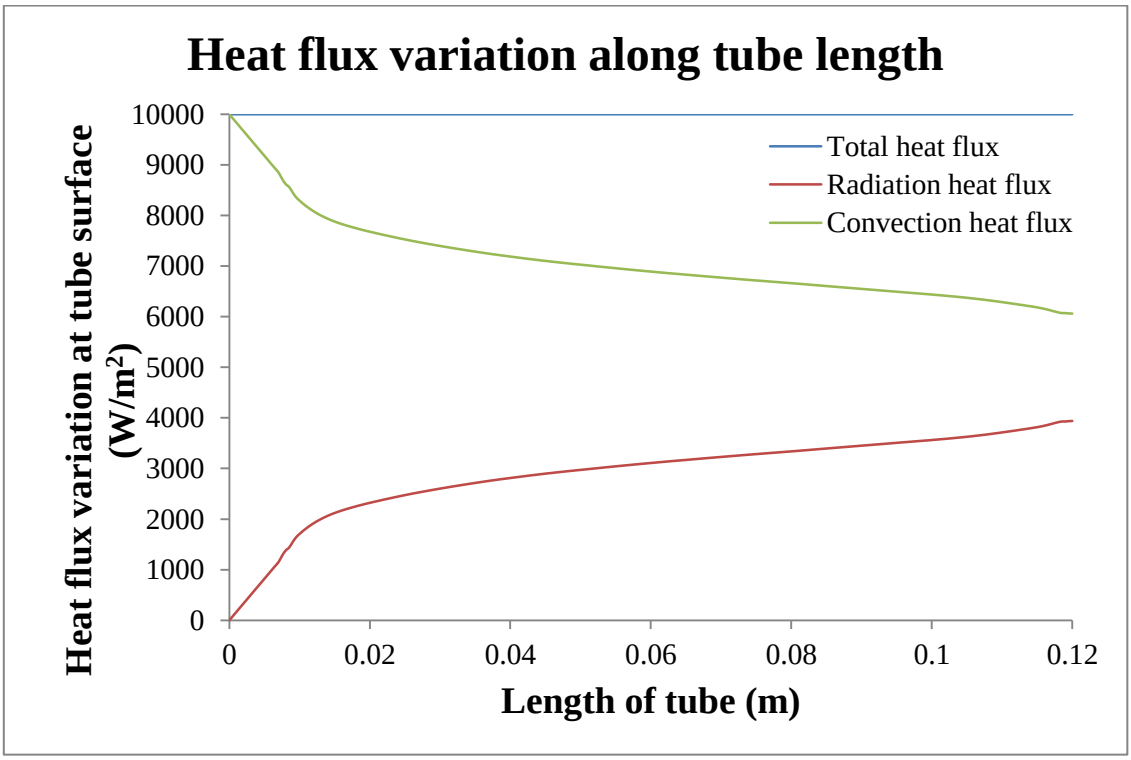

Fig. 3.5: Tube heat flux variation along the length of the tube

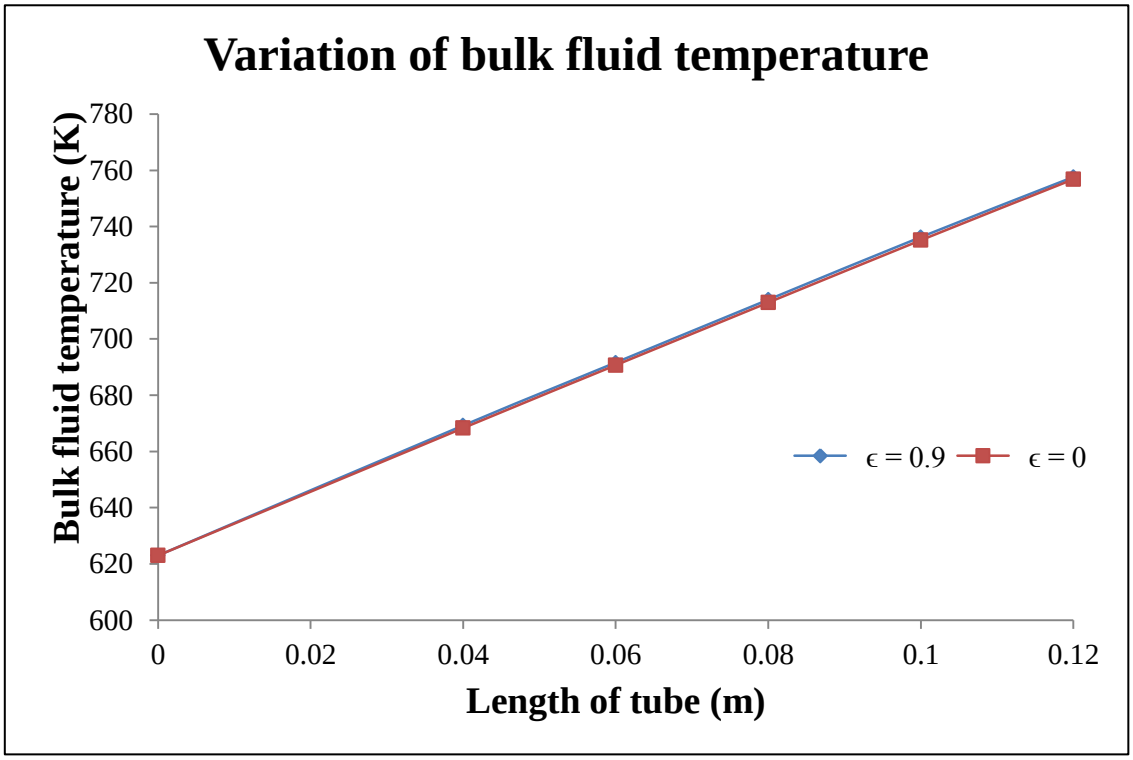

Fig. 3.6: Bulk fluid temperature variation along the length of the tube

It is important to note here that we are investigating not just the effect of including radiative heat transfer in developing flows, but the effect of participating media. In order to show this explicitly, we present data in figure 3.7 for three situations: pure convection, and radiation with and without gas absorption. The stream-wise distribution of tube wall temperatures for these three situations clearly shows that including the effect of gas participation can have significant effects on the overall heat transfer. Radiation alone, without the effects of gas participation, does affect the tube wall temperatures. Including the effect of gas participation makes the wall temperatures come down significantly, by as much as 200 K for the case considered (L=120 mm, D=12 mm, Re=1000).

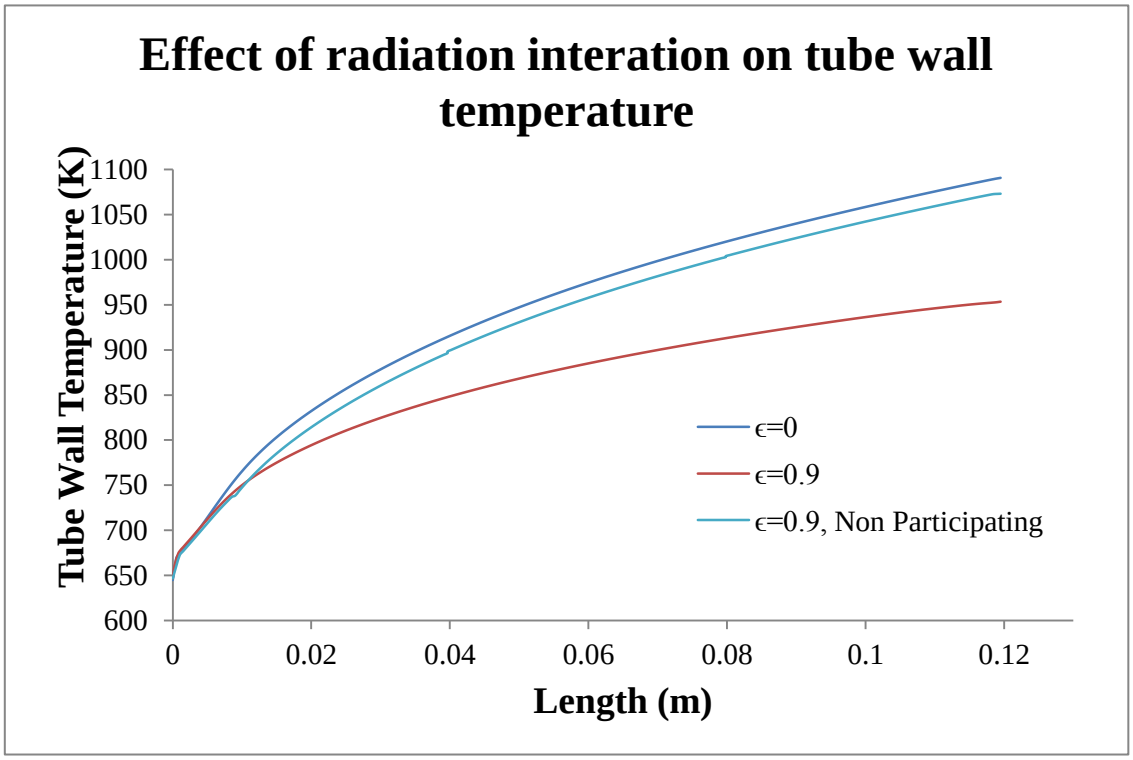

Fig. 3.7: Tube wall temperature variation along the length of the tube for different radiation conditions

The net effect of radiation on the quantities of significance for engineering design, viz. the heat transfer coefficient (h) and Nusselt number (Nu), is shown in figure 3.8 and figure 3.9, respectively. We define an effective heat transfer coefficient based on the total flux and the difference between the wall (T_w) and gas bulk temperatures (T_b):

$$h_{eff} = \frac{q_{total}}{T_w - T_b} \qquad (\ldots \text{Eqn. 3.2})$$

The convective heat transfer coefficient and convective Nusselt number carry their usual definition, based on the diffusive flux in the momentum boundary layer, while the definition of effective Nusselt number is based on the effective heat transfer coefficient given by equation 3.2. While the convection heat transfer coefficient drops as the momentum boundary layer thickens downstream, the increasing contribution of radiative heat transfer results in the effective heat transfer coefficient being nearly constant in the developing flow region. Near the tube exit, the lowering of the wall temperature due to radiative transport has the effect of slightly increasing the overall heat transfer coefficient. The Nusselt number, when calculated using the local thermal conductivity based on local bulk temperature, shows a continuous decrease.

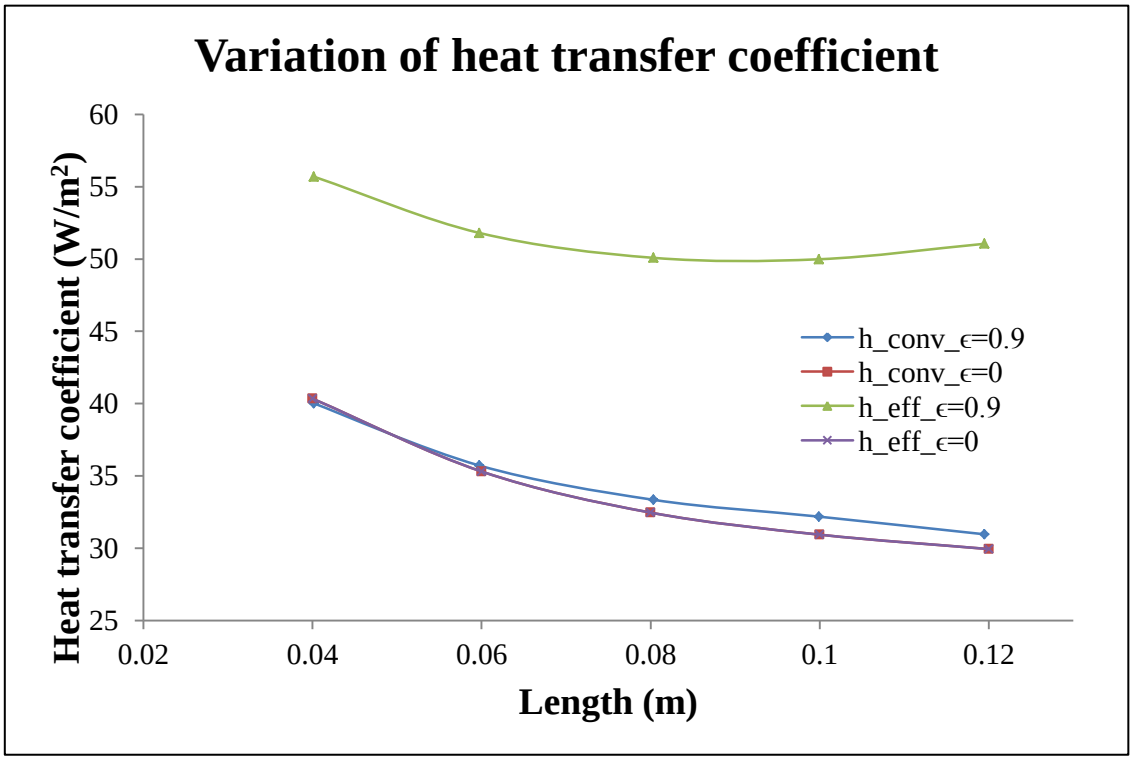

Fig. 3.8: Heat transfer coefficient variation along the length of the tube

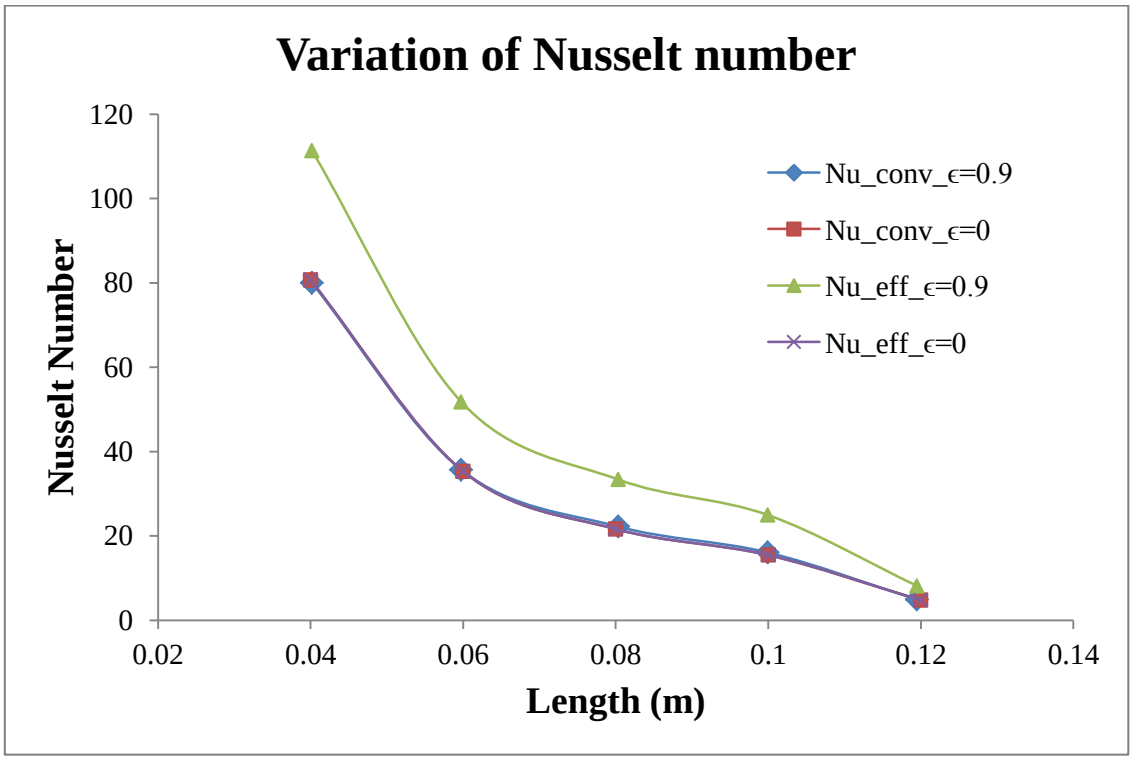

Fig. 3.9: Nusselt number variation along the length of the tube

3.4.1. Effect of Reynolds number

The effect of Reynolds number on the relative contribution of radiation heat transfer to the total heat transfer is shown in figure 3.10 for varying wall emissivity with a fixed total wall heat flux (10 kW/m^2) and geometry (D=12 mm and L=120 mm).

For any value of emissivity, the contribution of radiation heat transfer declines with an increase in Reynolds number. This is due to increase in convection heat transfer coefficient at larger Reynolds numbers. The contribution of radiation heat transfer increases with increasing wall emissivity. The presence of radiative heat transfer considerably alters the temperature distribution of the wall at high values of emissivity (ϵ = 0.9), as opposed to wall emissivity being zero, i.e. absence of radiation. For the same amount of heat flux to be transferred from the wall to the fluid, radiation aids convection in the task of transport of heat from tube wall to s-CO_2 flowing within the tube and the surface temperatures throughout the tube are lowered as the contribution of radiation increases with decreasing Reynolds number and increasing emissivity.

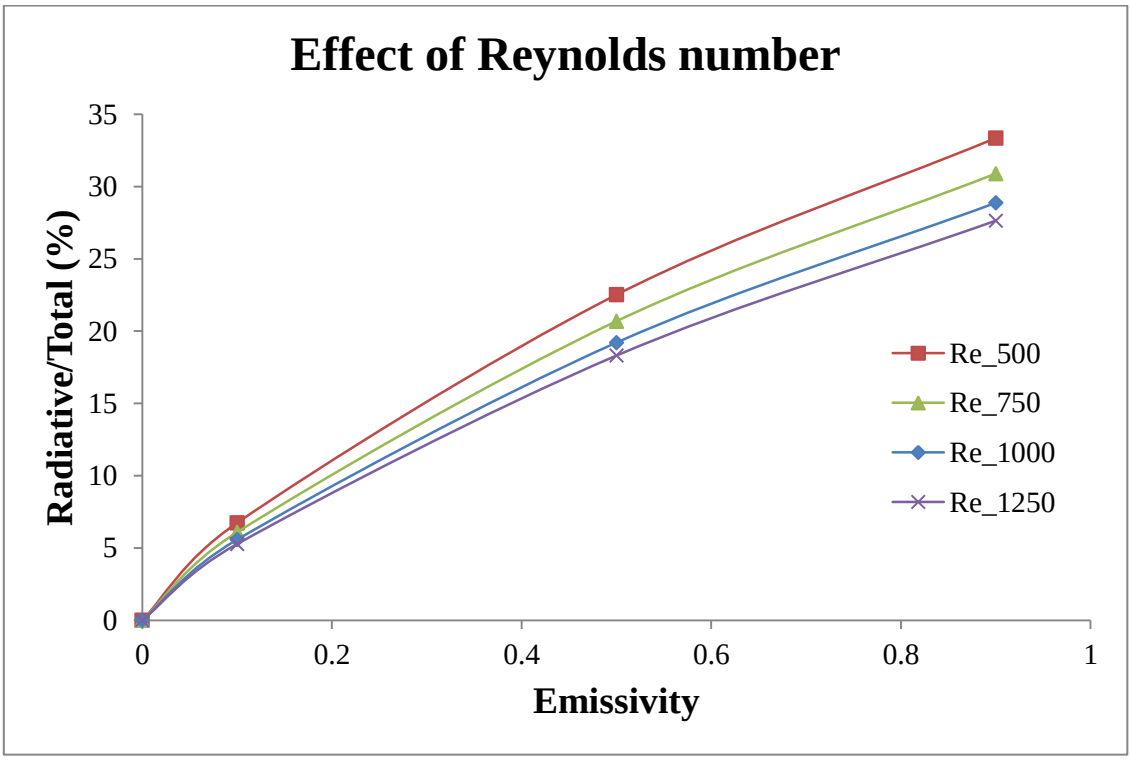

Fig. 3.10: Effect of Reynolds number on contribution of radiation heat transfer

3.4.2. Effect of tube diameter

The effect of tube diameter on the fraction of radiative heat transfer in the total heat transfer is presented in figure 3.11 for varying emissivity with a constant Reynold number (Re = 1000), constant total heat flux (10 kW/m^2) and tube length L = 500 mm.

Figure 3.11 shows that for any value of wall emissivity, the contribution of radiative heat transfer increases with an increase in tube diameter. With an increase in diameter, the tube surface area increases. Consequently, both convective and radiative heat transfer are enhanced due to a larger area. Figure 3.11 shows that the augmentation in radiation is more than that for convection, and hence the contribution from radiation increases with the diameter of tube.

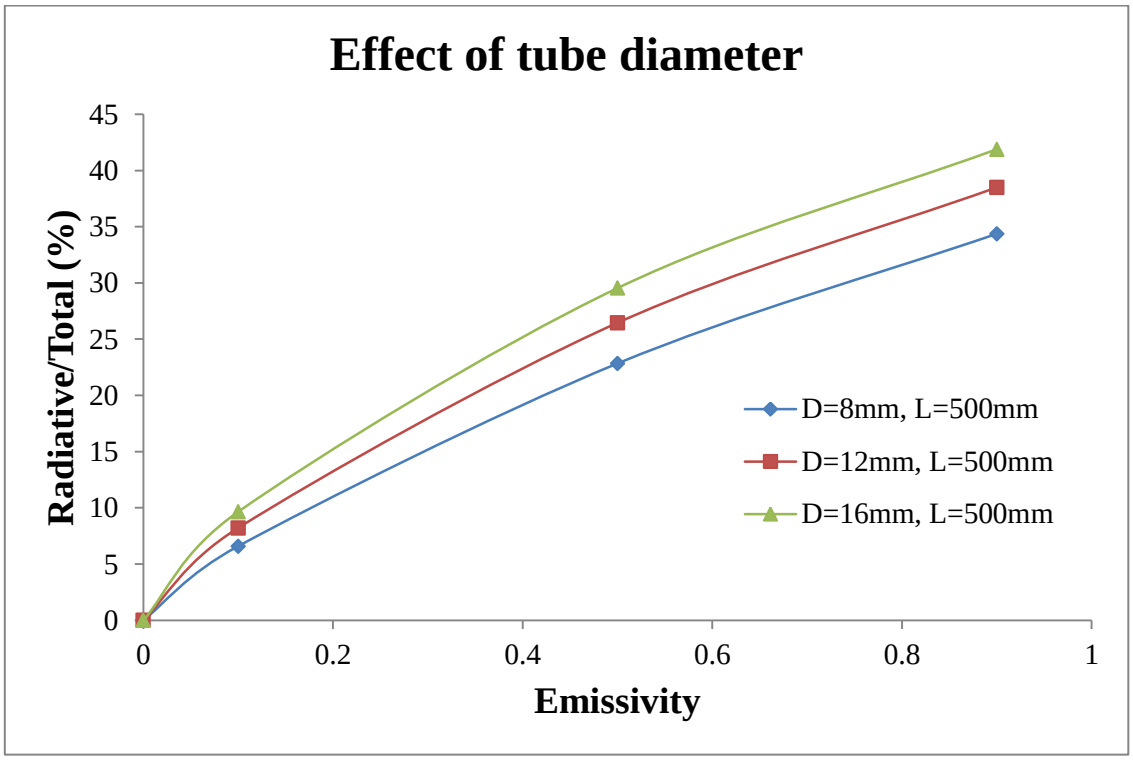

Fig. 3.11: Effect of tube diameter on contribution of radiation heat transfer

Depending on the optical thickness for the wavelength at which the wall emits radiation, s-CO_2 might be optically thick or optically thin for that wavelength. In the optically thin limit, s-CO_2 does not absorb any radiation; while in the optically thick limit, the radiation emitted by the wall is completely absorbed in the vicinity of the point of emission, rendering the contribution of radiative heat flux to be zero in both extremes.

The enhancement in radiation heat transfer with increase in diameter can be attributed to the larger path for absorption by s-CO_2. The effect of radiation in a participating medium is always to thicken the thermal boundary layer, as it offers an additional means of diffusing the thermal energy from wall. Hence, the effect of radiation is similar to decreasing the Prandtl number, thus resulting in a decrease in the convection heat transfer with an increase in radiation heat transfer.

3.4.3. Effect of tube length to diameter (L/D) ratio

The effect of tube length to diameter ratio (L/D) on the fraction of radiative heat transfer in the total heat transfer is presented in figure 3.12 for varying D, L/D, emissivity for a fixed Reynolds number (1000) and fixed total heat flux (10 kW/m^2).

With an increase in the tube length, contribution of radiative heat transfer increases. Strong convection heat transfer can be expected in the entrance region where the thermal boundary layer grows and there is a large temperature differential at the tube walls. For any diameter, as the length of tube increases, the contribution of radiation becomes significant.

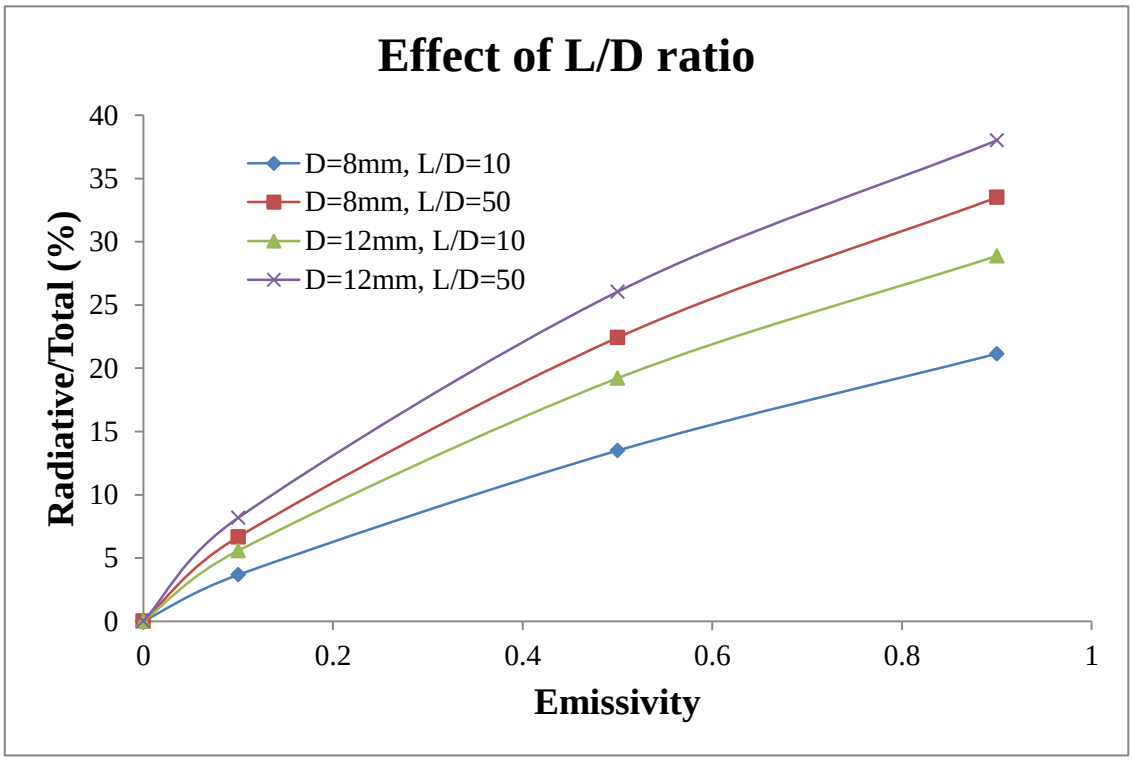

Fig. 3.12: Effect of L/D ratio on contribution of radiation heat transfer

3.4.4. Effect of wall heat flux

Figure 3.13 shows the contribution of radiation heat transfer for different geometric and total heat flux conditions for a fixed inlet Reynolds number (Re=1000).

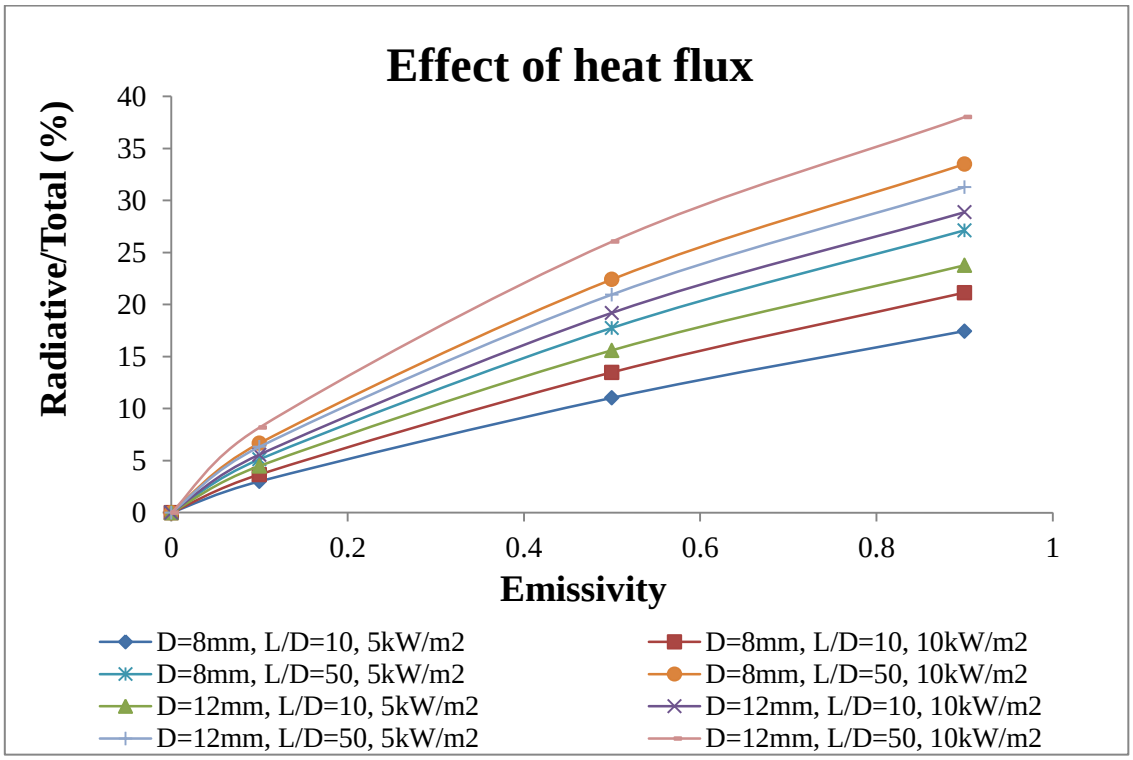

Fig. 3.13: Contribution of radiation heat transfer for varying total heat flux

For all geometric conditions, with increase in total heat flux value, the contribution of radiation heat transfer also increases. This is due to the higher wall temperatures required for transfer of larger amount of heat from wall to fluid. This alters the temperature distribution of the wall and the emission spectrum of the wall. Along with better matching of the emission spectrum of the wall at higher temperatures with the absorption spectrum of s-CO_2, radiation being a function of T^4 while convection being a function of T only is a possible explanation for the observed behaviour.

3.5. SUMMARY

Some of the major inferences that can be drawn from the fundamental investigation (figures 3.3-3.9) and the parametric investigation (figures 3.10-3.13) are as follows:

i. For accurate design and analysis of heat transfer equipment using s-CO_2 as the heat transfer fluid, considering the participation of s-CO_2 in radiation heat transfer is of

paramount importance when certain physical and geometric conditions exist in the equipment, especially in the presence of laminar flow.

ii. For tubular heat transfer equipment, it is found that deviation up to 250 K can be encountered in the prediction of peak and average tube wall temperature, if the participating nature of s-CO_2 is not accounted for during the heat transfer calculations. An important implication of this is that the tube temperatures will actually be quite lower as compared to the convection-conduction only case, and hence use of relatively lower temperature materials or a comparatively lower heat transfer area for transferring a certain amount of flux from the tube to s-CO_2 will be feasible.

iii. The tube geometry and optical properties of the tube inner surface in a s-CO_2 heat transfer equipment can be optimized and the radiation optical thickness can be controlled, thus designing the equipment in such a way that the required heat transfer is achieved using minimum heat transfer area and minimum temperature differential between the heat transfer surface and s-CO_2.

iv. In general, the radiative component in the overall heat transfer is more significant for lower values of Reynolds number and larger values of tube internal emissivity, radiative path length and tube temperature.

4. MEASUREMENT OF RADIATION HEAT TRANSFER IN SUPERCRITICAL CARBON DIOXIDE MEDIUM

4.1. INTRODUCTION

This chapter describes a new method to measure radiation heat flux emitted by s-CO_2, and the contribution of radiative heat flux is compared to that by pure convection heat flux by s-CO_2 under low Reynolds number turbulent conditions. To the best of the author's knowledge, measurement of radiation heat transfer by s-CO_2 and experimentally determined s-CO_2 emissivity has not been reported in the literature. Due to very high pressure, use of conventional spectroscopic methods to measure the radiative properties of s-CO_2 is challenging. In this chapter, a novel experimental method suitable for measurement of radiation emitted by s-CO_2 at such conditions, using appropriate heat transfer measurements in a shock tube, is presented. An estimation of the total emissivity is performed. Numerical simulation using ANSYS Fluent is also performed to evaluate the importance of radiation heat transfer in comparison to convection heat transfer of s-CO_2 for a typical low Reynold number turbulent flow of s-CO_2 in a circular tube. Convection heat transfer rate obtained from numerical simulation is compared with the radiation heat transfer rate obtained from the experiment.

4.2. EXPERIMENT DETAILS

In order to obtain CO_2 at pressure and temperature above critical value, CO_2 is used as the driven gas in a shock tube. A shock wave generated by sudden rupture of a diaphragm passes through the stationary CO_2 on the driven side raising its pressure and temperature. After the shock traverses through the complete driven section and gets reflected from the end flange, the temperature and pressure of the already shocked CO_2 is raised further, resulting in supercritical conditions. The whole process occurs in a few milliseconds, during which radiation heat transfer is measured while the reflected shock is traversing the already shocked CO_2. A thin film platinum sensor is used to measure the temperature rise and the radiation

heat transfer is subsequently calculated using the numerical solution proposed by Cook and Felderman algorithm [66]. The following sections describe some of the important details regarding the experiment.

4.3. SHOCK TUBE DESCRIPTION

A shock tube is a device that generates a normal shock wave by the sudden bursting of a diaphragm that separates a gas at a higher pressure from another at a lower pressure. The high-pressure side is termed as the driver section, and the low-pressure side is called the driven section. In order to raise the pressure and temperature of CO_2 above critical values, CO_2 is used as the driven gas in a shock tube. The generated primary shock traverses the driven section, increasing the pressure and temperature of the gas there. The shock wave then reaches the end flange wall and reflects back, resulting in further elevation of pressure and temperature. This characteristic behaviour of a shock tube is utilized to obtain stagnant s-CO_2 for a short time (~ millisecond). A thin film platinum sensor is used to measure the temperature rise and the radiation heat transfer is subsequently calculated using the numerical solution proposed by Cook and Felderman algorithm [66]. As the gas is stagnant and the time scale is only on the order of a millisecond, it is apparent that the heat flux measured by the sensor is by virtue of radiation only, emitted by the shocked gas at supercritical conditions.

In this experiment, the shock tube portion of the Hypersonic Shock Tunnel-2 (HST-2) at the Laboratory for Hypersonic and Shock Wave Research (LHSR), Indian Institute of Science, is employed to obtain the supercritical conditions. This shock tube consists of a 2 m long driver tube and a 5.12 m long driven tube, both fabricated using stainless steel SS304. The tubes are 12.5 mm thick and are designed to withstand gas pressures up to 27.5 MPa. The shock tube has an inner diameter of 50 mm, an outer diameter of 75 mm and honed inner walls. The driver side is equipped with a port to supply the driver gas from high pressure cylinders using appropriate pressure regulators. The driven side has ports to evacuate the driven part using a vacuum pump and then fill the driven tube to the desired pressure with a test gas. Two fast response piezoelectric pressure sensors (PCB Piezotronics Ltd., USA) are mounted near the end of the driven section, separated by a distance of 0.38 m, to measure speed of the primary shock wave. The second sensor is placed very close to the end wall of the tube so that it records the stagnation pressure labelled as P5 (pressure at state 5, as per standard shock tube

nomenclature). By observing the time difference between the triggering of the two pressure sensors placed at known locations, the primary shock Mach number is calculated. Using the primary shock Mach number and the value of P5, the temperature of the shocked gas (T5) can be calculated from standard shock tube relations, which can be obtained in literature (e.g. Anderson [67], Kumar et. al. [68]). Figure 4.1 shows the HST-2 shock tube schematic and the location of the pressure and thin film platinum sensor used in the present experiment.

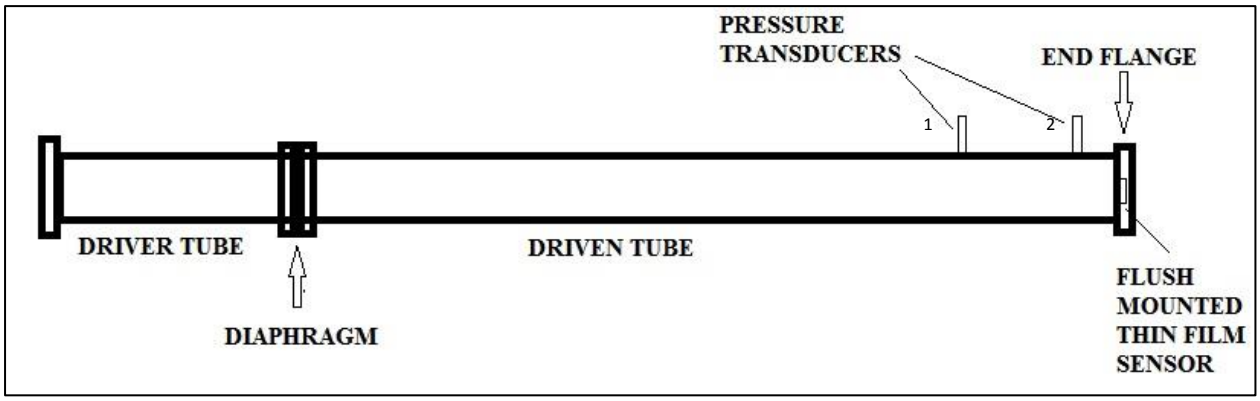

Fig. 4.1: Schematic of HST-2 shock tube

An aluminium diaphragm of 113 mm diameter and thickness varying between 1 to 3 mm (depending on the required shock strength) separates the driver and driven sections. Two perpendicular V-grooves made on the driver side of the diaphragm ensure proper rupture, clean petal formation, consistency and good control of the rupture pressure. The diaphragm used in this experiment is 2 mm thick and grooved to 1/3rd of its thickness. Figure 4.2 shows the ruptured diaphragm after the experiment. The petals open uniformly and remain attached to the body of the diaphragm.

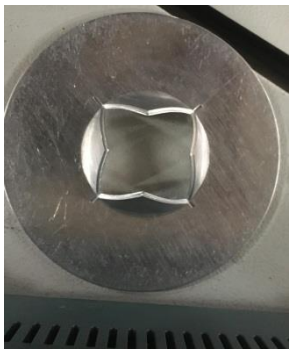

Fig. 4.2: Burst diaphragm after the test

4.4. EXPERIMENTAL CONDITIONS

In order to obtain a strong primary shock resulting in supercritical pressure and temperature of CO_2 after the reflected shock passes over the driven gas, a low molecular weight gas is used as the driver gas. Due to the hazards associated with hydrogen, helium is chosen as it has low molecular weight, is inert as well as cheap. The driven gas in this case is CO_2. Once the driver and driven gases are fixed, the initial pressure of the driven gas and the required primary shock Mach number can be calculated by knowing the final desired conditions for the shocked gas (i.e. P5 and T5). Equations to determine the same are straightforward and available in literature as well as in various existing online resources such as Wisconsin Shock Tube Laboratory Gas dynamics calculator [69]. For the required approximate conditions of pressure (P5 = 90 bar) and temperature (T5 = 1000 K), the following theoretical estimates (table 4.1) are obtained and the same conditions are executed in the shock tube HST-2.

Table 4.1: Shock tube conditions

Driver Gas	Helium
Driven Gas	Carbon Dioxide
Initial Temperature	Ambient (300 K)
Initial Pressure (CO_2)	2 bar
Mach Number	2.75
Pressure (P5)	90 bar
Temperature (T5)	1018 K
Rupture Pressure	36 bar

4.5. PLATINUM THIN FILM SENSOR PREPARATION AND CALIBRATION

Fast response platinum thin film gauges which exhibit typical response time ~5 microseconds are widely used in heat transfer measurements in shock tubes. For the present study, these gauges are prepared by depositing a thin platinum film on a ceramic backing material such as MACOR. The gauge is supplied with a constant current, and when its temperature rises due to heat transfer from s-CO_2, the resistance of the gauge increases. The instrumentation is designed to keep the current constant at the initial supply value despite the rise in resistance. Therefore, the rise in voltage across the gauge recorded by the data acquisition system corresponds to the temperature history of the sensor.

4.5.1. Preparation of the gauge

The base material for the thin film gauge is MACOR, which has good thermal insulation and machinability. MACOR also has a high melting point and maintains the integrity of its properties at elevated temperatures. For MACOR, with a thermal diffusivity of 7.94×10^{-7} m^2/s, the thickness of the sensor should be greater than 5 mm [70]. Once the MACOR is shaped according to the mounting arrangement on the end flange cavity, the location of platinum deposition is finalized. Holes of 0.9 mm diameter are drilled at appropriate locations on the substrate for drawing electrical leads. On the top surface, the drilled holes are given a countersink of 1.5 mm diameter to facilitate electrical connection. Presence of dust particles and other impurities on the MACOR surface affects the adhesiveness of platinum. Before the platinum layer is applied, the MACOR is cleaned thoroughly using an acetone bath inside an ultrasonic vibrator. After cleaning, platinum is deposited on the MACOR by hand painting. Thin strips of metallo-organic platinum ink (N.E. Chemcat Corporation, Japan) are applied directly onto the MACOR surface using a sharp tip. This ink comprises of platinum in liquid form along with a chemical binding agent. Once painted, the MACOR piece is transferred to an oven in which it is initially dried at a temperature of 398 K, at which point the chemical binding agents evaporate. After about 10 minutes, the temperature is raised to 893 K for curing. At this higher temperature, the surface of MACOR softens and the platinum gets embedded into the molecular structure of the backing material. The sensor is then left to cool down to room temperature naturally, which leaves a thin film of platinum of negligible

thickness on the MACOR substrate. Normal application of one such layer of platinum results in a gauge of initial resistance of around 30 – 50 Ω.

After platinum is deposited on MACOR, a thin layer of conducting silver paste procured from Hanovia Gold (USA) is coated within the countersink of each drilled hole, so that it makes good contact with the cured platinum. The sensor is again heated in an oven to a temperature of 723 K and allowed to cool down naturally. Electrical leads are then soldered to the silver coating and the wires are drawn from the back face of the sensor, passing through the drilled holes. Care is taken to ensure that the solder filled the countersunk holes on the MACOR surface and does not protrude out. Figure 4.3 shows a typical gauge consisting of three identical hand-drawn sensors.

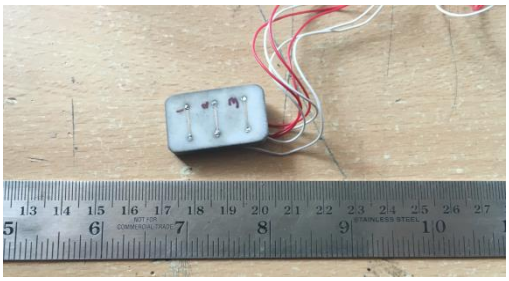

Fig. 4.3: Typical gauge with three sensing elements

4.5.2. Calibration of the gauge

Temperature coefficient of resistance (α) is an important parameter in deducing the temperature data from platinum thin film sensors. It is defined as the change in resistance per unit change in temperature. The set-up to measure α for our sensor consists of an empty beaker placed in an oil-filled chamber. The gauge and an attached thermometer are suspended into the empty beaker and the sensor is heated by natural convection using hot air. This arrangement is used to attain a gradual change in temperature of the sensor. The voltmeter connected across the gauge measures the change in voltage due to a change in temperature when a constant current is applied across the gauge. The temperature of the gauge is increased from room temperature to 373 K, and the corresponding voltage is noted after every 5 K rise in temperature. The alpha calibration curve and the final value is presented in section 4.8.

Another important parameter required for post-processing the measured signal (voltage) from a thin film gauge is β, which is defined as $\sqrt{\rho C k_s}$. The parameter β represents a combination of properties related to the backing material (MACOR). The value of β for MACOR used in the present experiment is taken from Srinivasa [71]. For this purpose, a similar platinum thin film sensor was located in the stagnation line of a cylinder in cross flow, placed at the end of the driven section of a low Mach number shock tunnel. At these flow conditions, the stagnation point heat flux can be predicted accurately using the expression given by Fay and Riddell [72]. By substituting the theoretically predicted value of convection heat flux in equation 4.1 given below, along with a known value of α, the numerical value of $\sqrt{\rho C k_s}$ was calculated to be 1700 W/m^{2}Ks$^{1/2}$ [71]. As the MACOR used in the present experiment is same as that used in [71], the same value of β is used here.

Knowing α for the thin film gauge and β for the MACOR, the voltage signal measured from the sensor can directly be converted into heat flux using the Cook and Felderman algorithm [66]. The algorithm is applied to the heat transfer equation obtained from 1-dimensional semi-infinite heat conduction analysis of the gauge, as detailed by Kumar [73].

The final form of the transient heat conduction equation, obtained from Kumar [73], is given as equation 4.1:

$$\dot{q}(t) = \frac{\beta}{\sqrt{\pi}\alpha E_f}\left[\frac{E(t_n)}{\sqrt{t_n}} + \sum_{\iota=1}^{n-1}\left\{\begin{array}{c}\frac{E(t_n)-\dot{E}(t_\iota)}{\sqrt{(t_n-t_\iota)}} - \frac{E(t_n)-E(t_{\iota-1})}{\sqrt{(t_n-t_{\iota-1})}} \\ +2\frac{E(t_\iota)-E(t_{\iota-1})}{\sqrt{(t_n-t_\iota)}+\sqrt{(t_n-t_{\iota-1})}}\end{array}\right\} + \frac{E(t_n)-E(t_{n-1})}{\sqrt{\Delta t}}\right] \qquad (\ldots\text{Eqn. 4.1})$$

The procedure for iteratively solving equation 4.1 is programmed in MATLAB to calculate the heat flux at *n* discrete points in the time interval (0, t). E_f is the initial voltage for the platinum sensor which is recorded before the diaphragm ruptures, while α and β and are determined using the methods described above.

4.6. SENSOR MOUNTING

Due to mechanical failure of the thin film sensor, three geometric configurations of sensor mounting were attempted to obtain the radiation heat flux. The three configurations are discussed in the following sub-sections.

4.6.1. Configuration 1

The first configuration of the flange is shown in figure 4.4. It is a circular aluminium flange with an outer diameter of 240 mm and thickness of 26 mm. A 7 mm deep hole was milled at the centre of the flange to accommodate the platinum sensor and a thin quartz glass piece was used to separate the sensor from CO_2. An adhesive was used to fill the gap between the walls of the sensor and the cavity to ensure sealing. After mounting the quartz glass, the system was covered with Kapton tape and the experiment was conducted. Due to the large exposed area and the impact of shock, quartz glass was shattered and the sensor cracked as seen in figure 4.5.

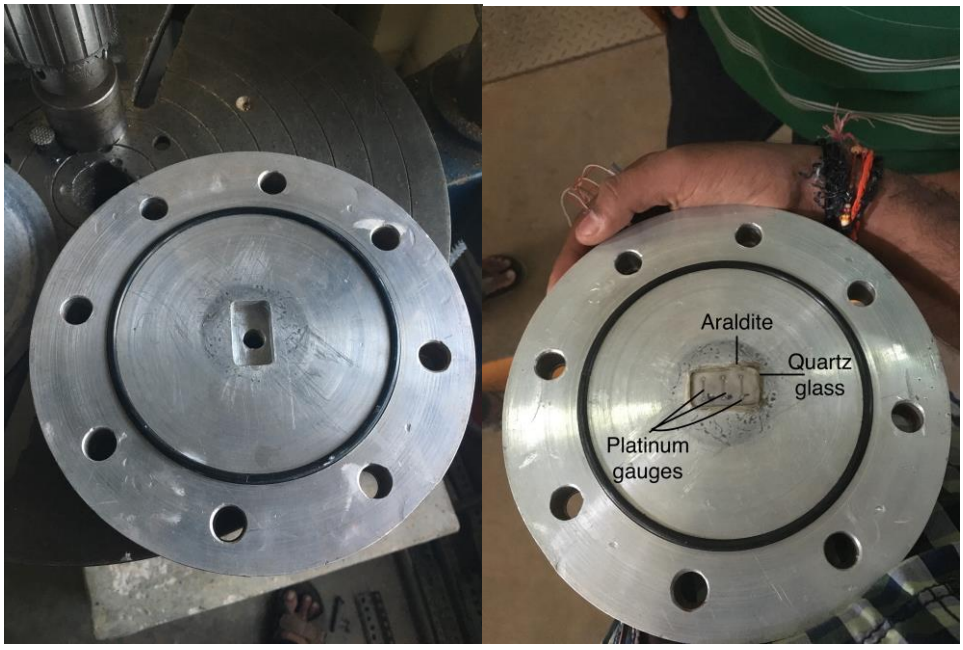

Fig. 4.4: End-flange with cavity for mounting sensor and assembled flange

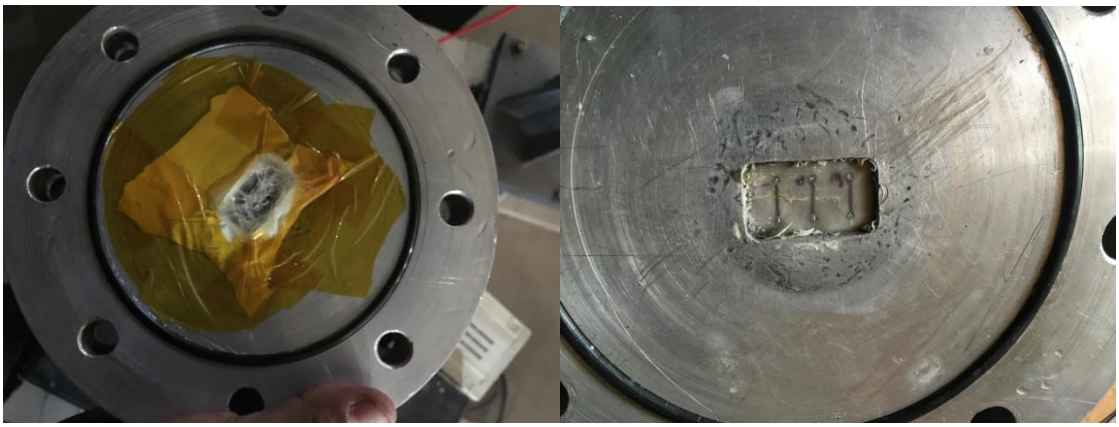

Fig. 4.5: Shattered quartz glass and cracked sensor after removal of tape and quartz

4.6.2. Configuration 2

After the first configuration failed mechanically, the next design incorporated a smaller area of quartz along with a metal adapter and rubber padding to absorb the impact of the shock. The adapter was modelled in CATIA and the fabricated adapter is shown in figure 4.6. Figure 4.7 shows the end flange system and the assembled system.

Configuration 2 was tested and the quartz glass shattered due to the metal adapter and glass contact, but the sensor was intact.

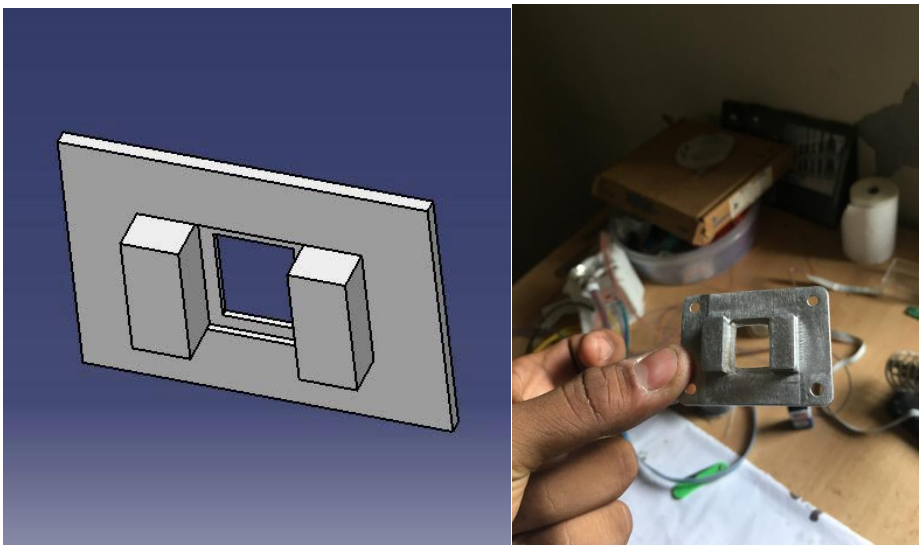

Fig. 4.6: Adapter design for configuration 2

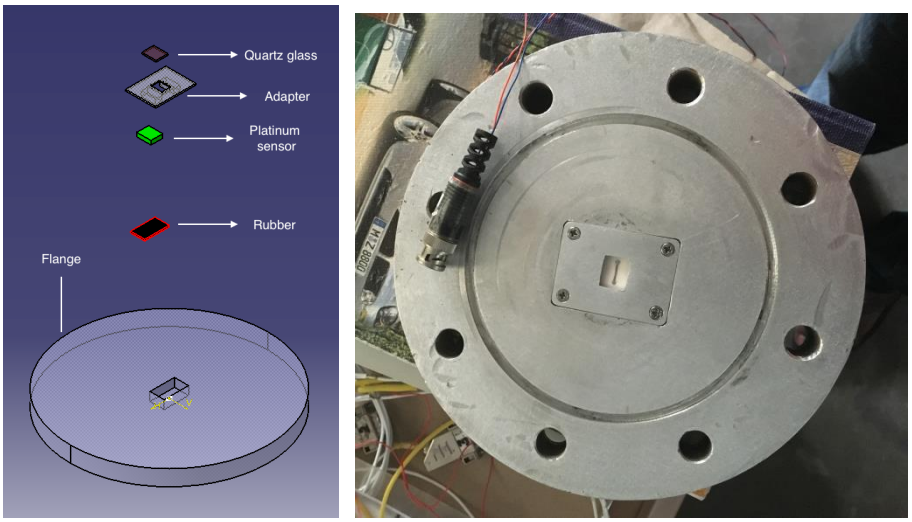

Fig. 4.7: Configuration 2 concept and assembled flange

4.6.3. Configuration 3

In this attempt, a new flange with a mounting port and a bolt-adapter (figure 4.8) was designed such that a protective O-ring could be placed between the sensor and the metallic part of the adapter. Also, the exposed area of quartz and sensor assembly was reduced.

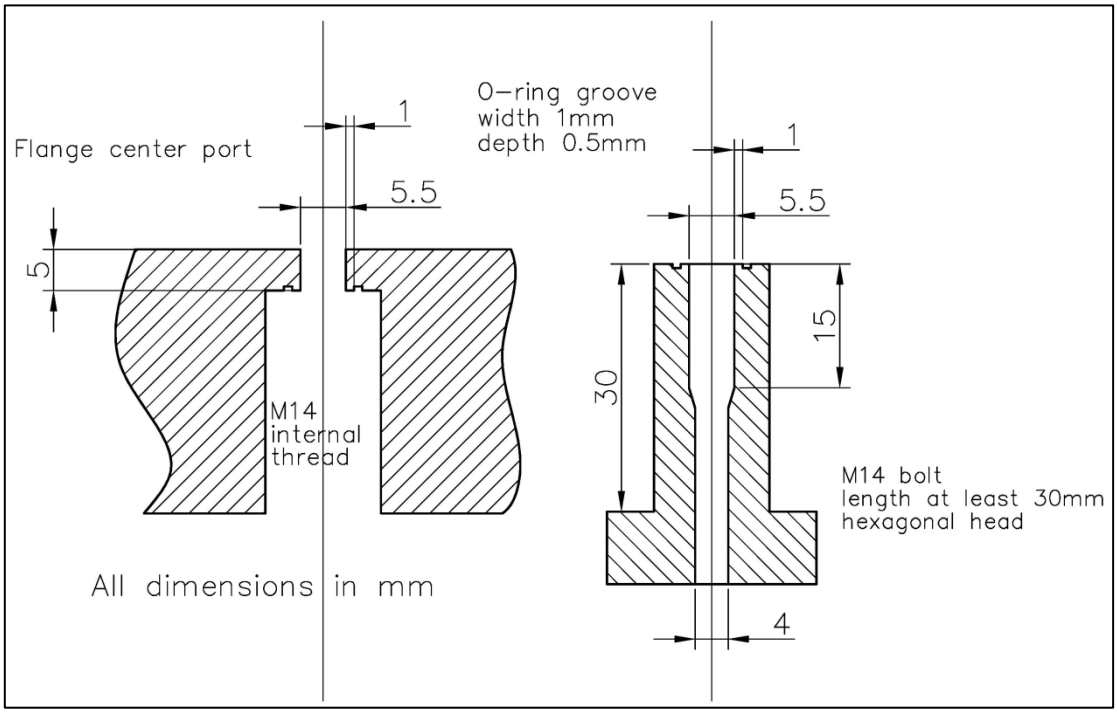

Fig. 4.8: Flange centre port and bolt-adapter for sensor mounting

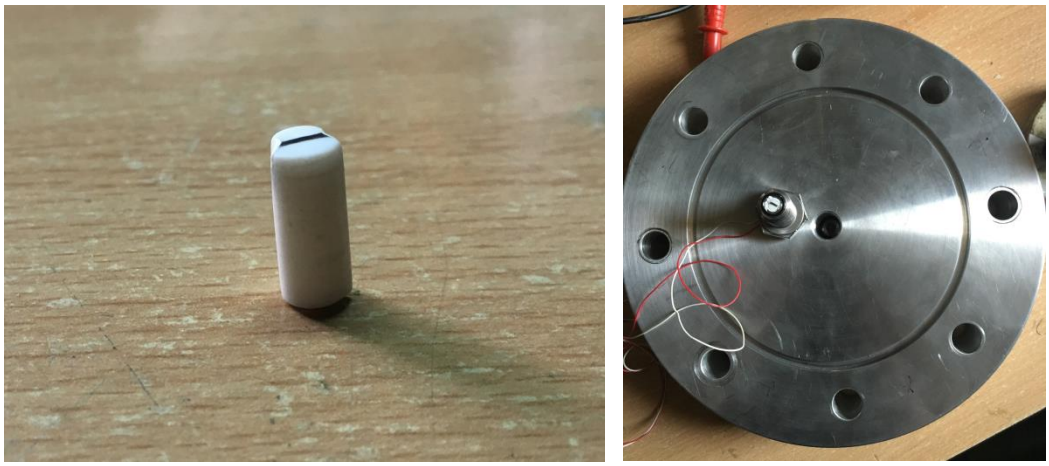

Fig. 4.9: Platinum thin film sensor and sensor-flange unit

This aluminium flange has an outer diameter of 240 mm and is 34 mm thick. Quartz glass with a diameter of 7 mm and thickness 2 mm is used. The circular exposed area has a diameter of 5.5 mm. The MACOR piece is circular with 5 mm radius and 13 mm cylindrical height. Figure 4.9 shows the platinum thin film sensor and the sensor-flange unit. Configuration 3 is used to perform the experiment to obtain radiation heat flux data.

4.7. NUMERICAL MODELLING

For estimating the contribution of radiative heat flux as a percentage of the total heat flux (radiation + convection), the measured radiation emission by s-CO_2 in the present experiment is compared with the typical convective heat flux value for a low Reynolds number turbulent flow obtained using a Computational Fluid Dynamics (CFD) model. A circular geometry of the tube is chosen as it is a common configuration element used by researchers to design high pressure receivers and heat exchangers for use in the s-CO_2 Brayton cycle. Low Reynolds number turbulent flow with Re = 6000 is chosen for the comparison as flow through receiver tubes and compact heat exchangers in s-CO2 Brayton cycle are typically within this range of Reynolds number Also, previous studies have revealed that radiation heat transfer may be comparable to convection for low-speed flows as seen in chapter 3, while it has a negligible impact for highly turbulent flows [58].

A 2-dimensional axisymmetric section of a circular tube (figure 4.10) is modelled and meshed in ANSYS ICEM CFD. The length and diameter of the tube are fixed at 600 mm and 12 mm, respectively. A constant temperature (300 K) boundary condition is applied on the outer wall of the tube. Appropriate inlet velocity (based on Re) and pressure outlet boundary conditions are specified for the tube inlet and tube outlet, respectively.

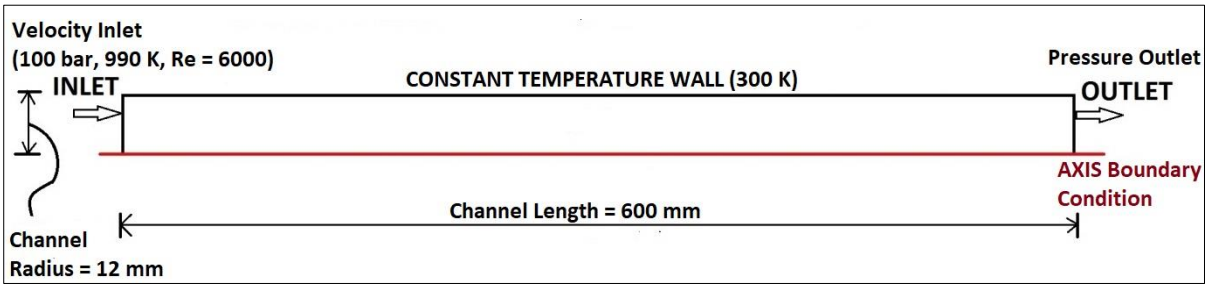

Fig. 4.10: Geometry and boundary conditions for the 2-D axisymmetric model

A non-uniform structured quadrilateral mesh is generated by using the 'blocking' technique in ICEM CFD. Grid independence study is performed and the grid system is refined until doubling the number of control volumes yields negligible difference in the solution of parameters of interest.

Coupled and discretized conservation equations for transport of mass, momentum, energy and turbulence are solved by ANSYS Fluent, which uses the finite volume method to discretize the transport equations [62]. The steady state, pressure based solver using SIMPLE algorithm and second-order upwind for spatial discretization is employed. Mass flux, energy flux and scaled residuals are continuously monitored as the solution developed, and convergence is assumed when the quantities of interest exhibit negligible variation and the scaled residuals for the governing equations drop below 10^{-3} and remained constant thereafter.

To obtain accurate thermo-physical properties for s-CO_2, ANSYS Fluent is linked to a database called as REFPROP, viz. provided by NIST [63]. The equation of state for CO_2 provided by Span and Wagner is used by this database [64].

The radiative transport equation is not solved in the numerical model and participation of s-CO_2 is hence, neglected. The hot high-pressure s-CO_2 loses heat to the colder tube wall by convection and diffusion only. The effect of gravity is ignored and s-CO_2 at the 'velocity inlet' boundary is specified to enter at a pressure and temperature of 10 MPa and 990 K, respectively. The standard k-ε turbulence model with enhanced wall functions is implemented to model the turbulent flow.

4.8. RESULTS AND DISCUSSION

4.8.1. Thermal coefficient of resistance (α) calibration

The α-calibration for the sensor used in configuration 3 is performed by the method discussed in section 4.5.2. Figure 4.11 shows the alpha calibration data. The change in voltage as a response to change in temperature is recorded and the thermal coefficient of resistance is calculated using equation 4.2:

$$\alpha = \frac{1}{IR}\frac{\Delta V}{\Delta T} \qquad (\ldots \text{Eqn. } 4.2)$$

where I and R are the constant current supplied to the gauge and the initial resistance, respectively. The value of $\Delta V/\Delta T$ is the slope of the graph in figure 4.11.

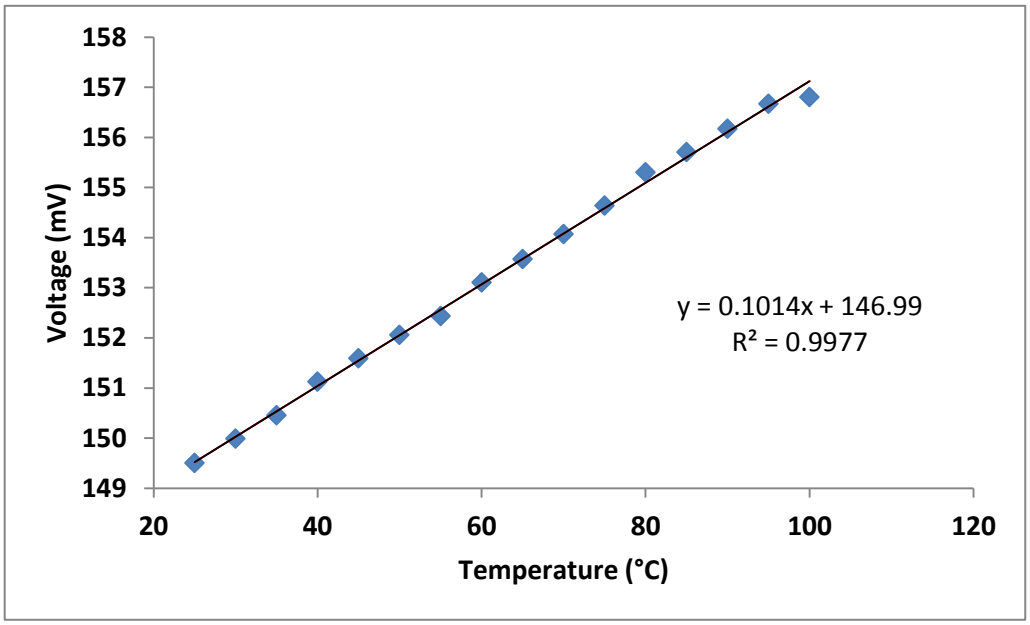

Fig. 4.11: Thermal coefficient of resistance calibration

The value of thermal coefficient of resistance calculated from equation 4.2 is 0.00085 K^{-1}.

4.8.2. Variation of Pressure in Driven Section

The pressure variation in the driven section as measured by the two fast response pressure transducers mounted in the driven section is shown in figure 4.12. The first sensor (Pressure Sensor 1, shown in figure 4.1) is triggered when the primary shock wave passes it, raising the pressure and temperature of the gas. As the shock wave moves forward, the second sensor (Pressure Sensor 2) is triggered.

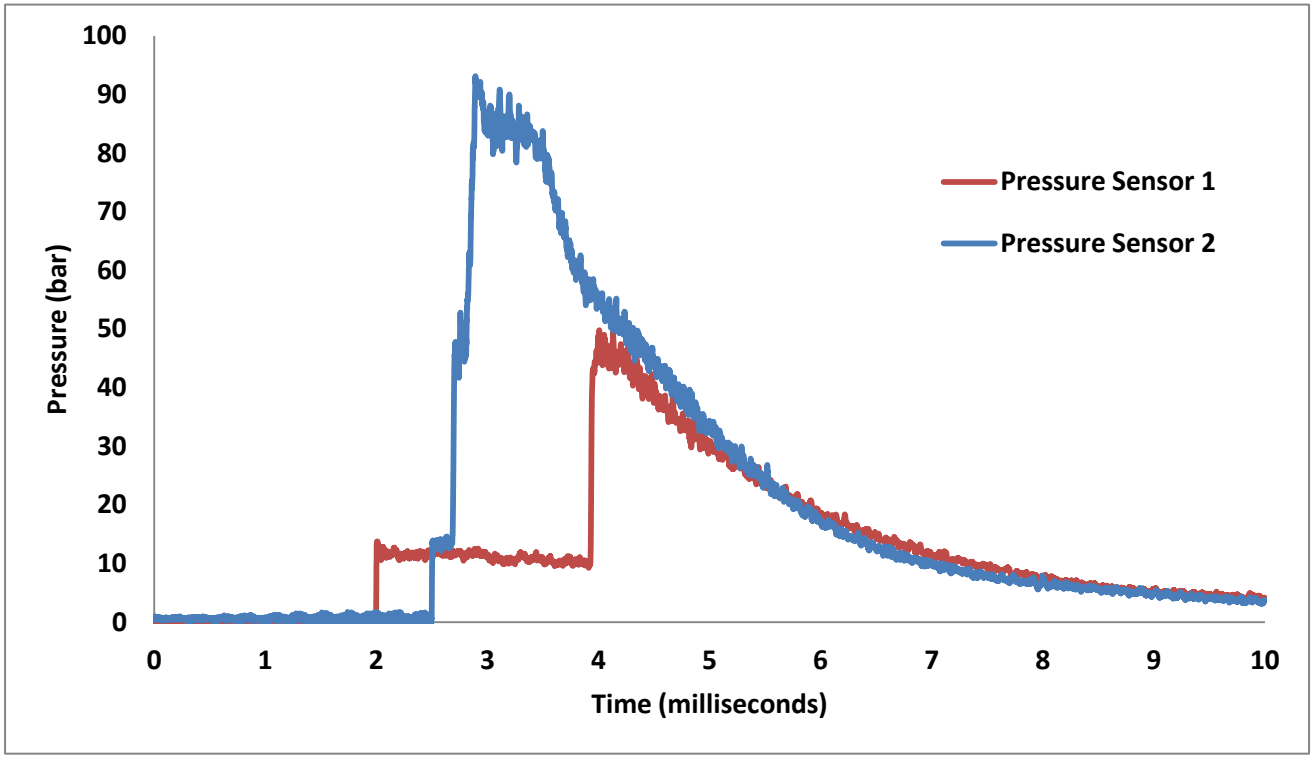

Fig. 4.12: Pressure Variation for s-CO_2 in the driven section

The second jump in Pressure Sensor 2 happens when the reflected shock traverses it, raising the pressure (P5) to 85 bar. The Mach number is 2.75 and the temperature of the shocked gas is calculated from equation 4.3, as given in Kumar et. al. [74].

$$\frac{T_5}{T_{initial}} = \frac{[2(\gamma_1-1)M_1^2+(3-\gamma_1)][(3\gamma_1-1)M_1^2-2(\gamma_1-1)]}{(\gamma_1+1)^2M_1^2} \quad \text{(…Eqn. 4.3)}$$

where, $T_{initial}$ is the initial temperature of CO_2, viz. 300 K, $\gamma_1$is the ratio of specific heats of CO_2 at initial pressure (2 bar) and temperature (300 K), viz. 1.297 and M_1 is the primary shock Mach number (2.75).

The temperature (T5) of the shocked gas calculated from equation 4.3 is 990 K. Within a few milliseconds of peaking, the pressure and temperature of s-CO_2 drop due to diffusion of helium and CO_2, giving an effective test time of about 600 microseconds for measuring the radiation heat flux. The heat flux is measured after CO_2 reaches supercritical conditions (85 bar and 990 K) and before the onset of diffusion, as reported below.

4.8.3. Radiation Heat Flux Measured by the Thin Film Sensor

The heat flux variation with time measured by the platinum sensor is shown in figure 4.13.

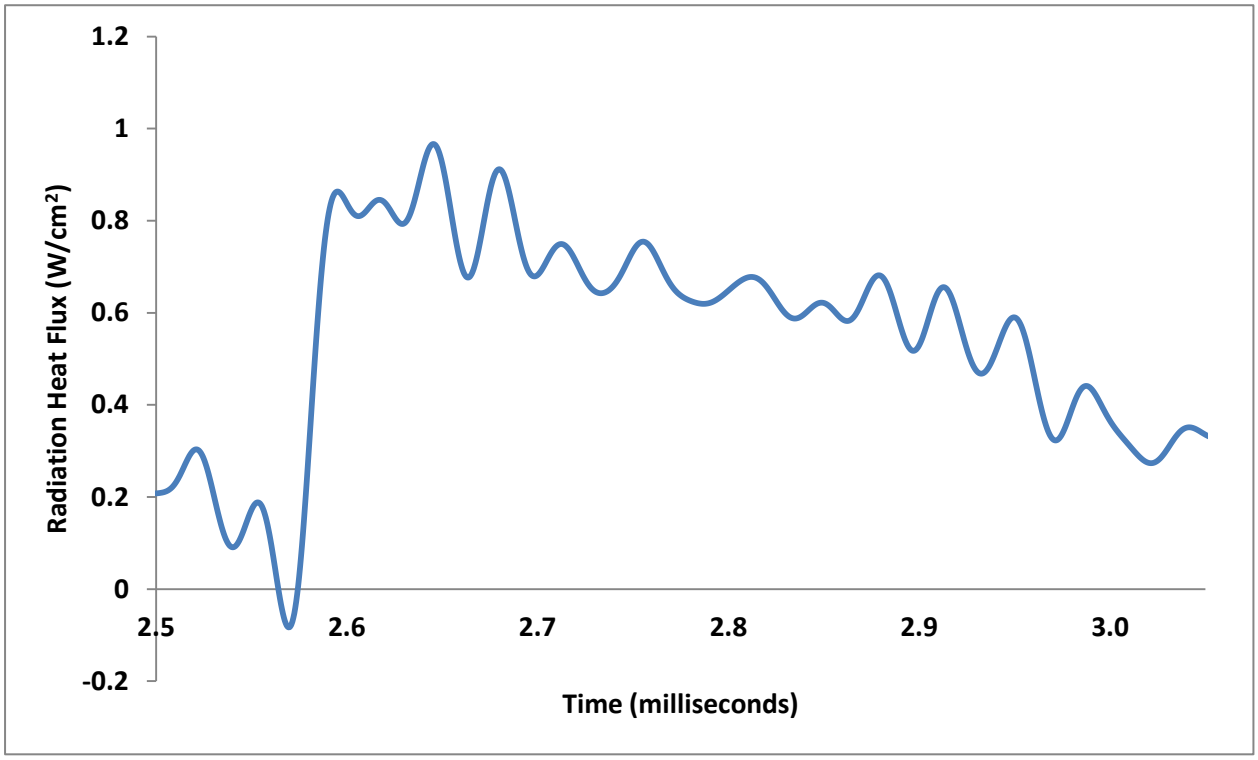

Fig. 4.13: Measured radiation heat flux

This measured value of heat flux is derived from the numerical solution of equation 4.1, using the Cook and Felderman algorithm as outlined in section 4.5.2. The absorptivity of the sensor is also taken into account. As seen in figure 4.13, a peak radiation heat flux value of about 0.95 W/cm^2 was measured by the sensor.

4.8.4. Estimation of emissivity for s-CO_2

The emissivity of s-CO_2 is estimated by comparing the radiation heat flux measured by the thin film platinum sensor with the blackbody emissive power corresponding to the temperature of s-CO_2, i.e. 990 K. The total emissivity value is calculated as:

$$\varepsilon_{s-CO_2,total} = \frac{Radiation\ Heat\ Flux\ of\ Gas}{\sigma T_b^4} \qquad (\ldots \text{Eqn. } 4.4)$$

where σ is the Stefan Boltzmann constant (5.67 × 10^{-8} W/m^{2}K^4) and T_b is the blackbody temperature.

Based on the above formulation, the emissivity of supercritical carbon dioxide at 85 bar and 990 K is calculated to be 0.17. The radiation heat flux variation shown in figure 4.13 is measured over a very short time period of about 0.4 milliseconds. The estimated reflected shock speed for the current shock tube conditions is about 250 m/s, the shocked gas path length when the radiation heat flux is measured is 4 cm.

The emissivity value for a gas is typically specified along with the pressure (bar), temperature (K) and the product of pressure, p, and path length, L [i.e. product pL (bar-cm)] for which the measurement/calculation of emissivity is performed. For the current measurement, the pressure is 85 bar and the path length is about 4 cm when the radiation heat flux peak value is measured. The pL product is obtained as:

$$pL = 85(bar) * 4(cm) = 340\ bar - cm \qquad (\ldots \text{Eqn. } 4.5)$$

For a pressure of 1 bar, temperature of 1000 K and a pL product equal to 340, the value of total emissivity for CO_2 is predicted using an analytical method by Farag and Allam [75]. The data from this reference is reproduced in figure 4.14. For 1 bar, 1000 K and 340 bar-cm, the value of emissivity is estimated to be about 0.2.

For an elevated pressure of 85 bar at the same temperature (1000 K) and pL (340 bar-cm), the prediction of total emissivity can be obtained from the following equation given in Modest [65]:

$$\frac{\varepsilon(pL,p,T_g)}{\varepsilon(pL,1\ bar,T_g)} = 1 - \frac{(a-1)(1-P_E)}{a+b-1+P_E}\exp\left(-c\left[\log_{10}\frac{(pL)_m}{pL}\right]^2\right) \qquad (\ldots\text{Eqn. 4.6})$$

where P_E (effective pressure), a, b, c and $(pL)_m$ are correlation parameters which are described in Modest [65]. Using the values of pressure, temperature and the pL product for the present case, equation 4.6 predicts that the emissivity at the present elevated pressure is found to be almost same as that at 1 bar. Thus, the measured value of emissivity (0.17) in the present work is in close agreement to the theoretically predicted value.

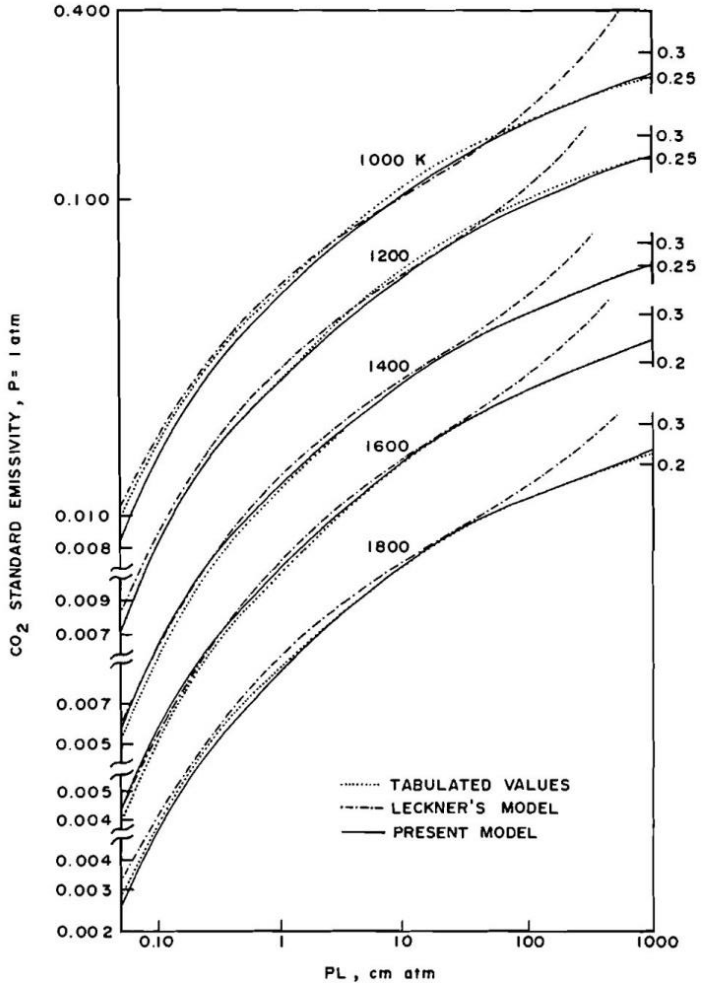

Fig. 4.14: Emissivity of CO_2 for 1 bar at varying temperature and pL [75]

4.8.5. Comparison of radiation with convection heat flux

For the numerical model described in section 4.7, as the hot s-CO_2 at 990 K enters the circular tube and loses its energy to the constant temperature wall at 300 K, its temperature drops gradually along the axial length of the tube. The transfer of heat from s-CO_2 to the wall is purely by convection-diffusion in the simulated case. The purpose of this simple numerical experiment is to provide a reference convection heat flux with which the radiation heat flux measured experimentally can be compared. The centre line temperature variation of s-CO_2 is plotted along with the wall temperature, which is constant at 300 K (figure 4.15).

As seen in figure 14, the fluid cools and decelerates as it travels along the tube. Post-processing in ANSYS Fluent reports an average convection heat flux along the length of the tube to be 55 kW/m^2**.** Hence, the magnitude of the measured radiation heat flux is estimated to be about 17.4% of the corresponding simulated convective heat flux.

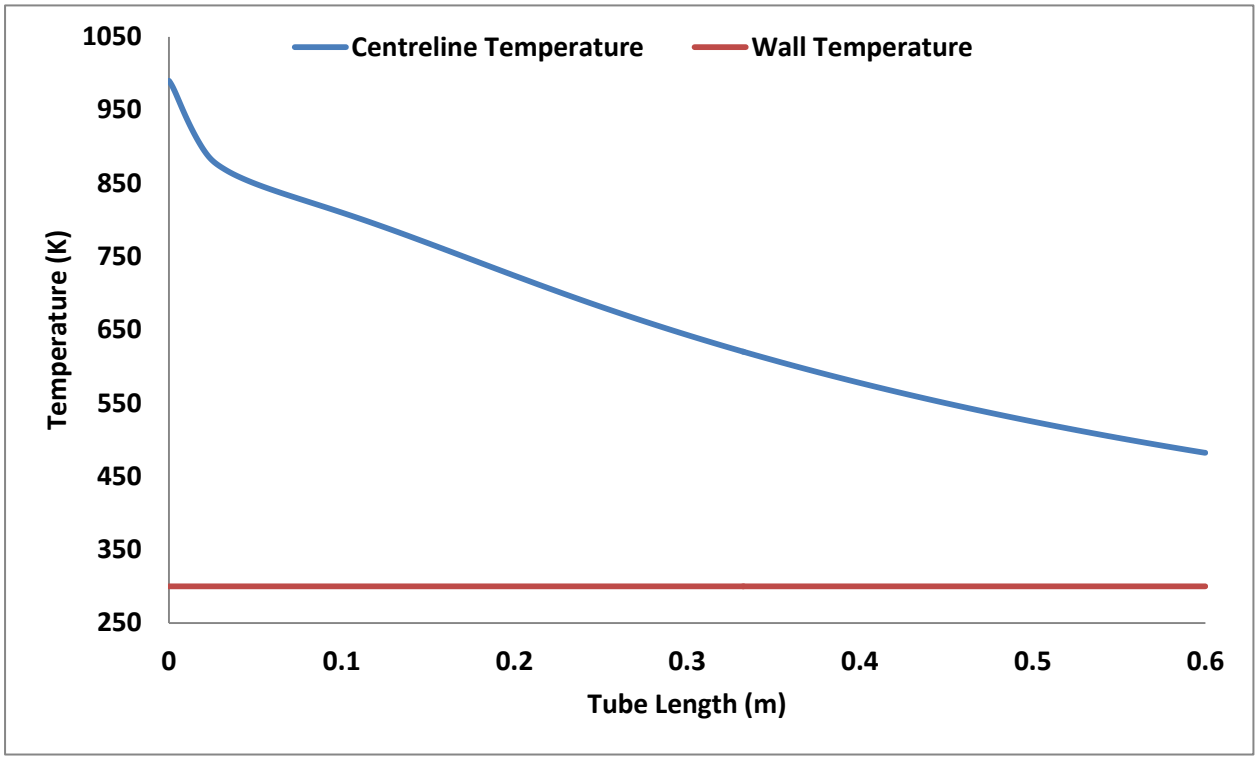

Fig. 4.15: Variation of centreline fluid temperature and tube wall temperature along the length of the tube

4.9. REMARKS

A new experimental technique for investigating the radiative properties of s-CO_2 as a participating medium is presented in this chapter. It is found that s-CO_2 acts as a participating medium, and the percentage contribution of radiation towards the total heat exchange in a typical heat transfer equipment can be significant. Traditionally, such effects were not considered in the design of heat exchangers used in s-CO_2 based power cycles involving high temperatures. Hence, the results of the present work will have tremendous implication in such designs.

However, it is important to note that any estimation of total emissivity value of s-CO_2 under such extreme conditions will have a good deal of uncertainty [65]. Hence, the value estimated using the present method should be considered only as an approximate one, and it opens up a wide scope for making more accurate and detailed measurements of spectral radiative properties of s-CO_2 for different path lengths. Nevertheless, the present study serves the important objective of making researchers consider s-CO_2 as a participating medium in radiation heat transfer calculations.

5. OPTICAL – THERMAL - FLUID ANALYSIS AND DEVELOPMENT OF TUBULAR RECEIVER FOR S-CO_2

5.1. INTRODUCTION

As discussed in chapters 1 and 2, the tubular receiver configuration is the most suitable option for direct heating of s-CO_2 in a central tower system. It is desirable that the receiver comprises of multiple panels which have tubes as the building elements. Such a modular arrangement has an advantage of ease of assembly, transport and repair/replacement of the receiver panels.

In this chapter, a design methodology for accurate coupled optical-thermal-fluid analysis is presented and the proposed methodology is then utilized for design of the panels which constitute the s-CO_2 receiver. The design and analysis of the panels is presented in two stages to evaluate the performance of the tubes and panels.

In the first set of analysis, details of the novel methodology for coupled analysis is presented and the effect of using a staggered arrangement of tubes to increase the effective absorptance and reduce the reflective losses by utilizing better geometry from radiation point of view is explored. A single panel receiver comprising of 5 tubes of length 2 m is analysed in this study. This analysis establishes the methodology/procedure and provides estimates for the tube wall temperature and efficiency for a typical incident flux distribution on the receiver tubes in conjunction with flow of s-CO_2 within the tubes.

For the second set of analysis, a detailed optical-thermal-fluid design of s-CO_2 tubular receiver panels is presented. Four panels consisting of ten tubes each are analysed with emphasis on possible flow arrangements with and without recirculation, different aim point strategies and power levels of operation. The aim point strategy refers to clusters of heliostats focussing on different points on the receiver, in contrast to all heliostats focussing on the centre of the receiver aperture. A series of simulations is performed to cover all possible combinations of flow recirculation configurations, aim point strategies and power levels (peak fluxes) to complete the design of panels for s-CO_2 receiver.

5.2 Development of Coupled Modelling and Initial Receiver Analysis

To incorporate a s-CO_2 Brayton power cycle in a solar power tower system, the development of a solar receiver capable of providing an outlet temperature greater than 900 K is necessary. The cycle analysis shows that s-CO_2 will undergo a temperature rise of around 150-200 K as it passes through the solar receiver. This requirement is for a s-CO_2 Brayton cycle with recuperation and recompression. In this study, an optical-thermal-fluid model is developed to design and evaluate a tubular receiver with a heat input ~2 MW_{th} from a heliostat field. The receiver consists of a single panel with 5 tubes of length 2 m each. The ray-tracing tool SolTrace is used to obtain the heat-flux distribution on the surfaces of the receiver. Computational Fluid Dynamics (CFD) modelling using the Discrete Ordinates (DO) radiation model is used to predict the temperature distribution and the resulting receiver efficiency. The effect of flow parameters, receiver geometry and staggered arrangement of tubes on the efficiency of the receiver is evaluated. In the following sub-sections, details of this study are presented along with the main results.

5.2.1. Material Considerations

As prescribed by Dostal et al [76], a turbine inlet pressure around 20 MPa and turbine inlet temperature greater than 923 K is required for approaching the 50% cycle thermal efficiency target. At these pressure and temperature conditions at the receiver exit, use of super alloys such as Inconel and Haynes is required for the receiver. For the studies in this chapter and in the following one, Haynes 230 and Inconel 625 are used as the candidate materials for receiver. These materials display superior maximum allowable stresses in the anticipated operation range of temperature compared to conventional metals. While previous receivers in the literature use stainless steel as the receiver material, it is not possible to use stainless steel in the case of s-CO_2 due to the combined presence of high temperature and pressure.

5.2.2. Modelling Methodology

Traditionally, researchers have used uniform flux or assumed approximate simple variation of heat flux as the input for receiver design. This approach can result in gross errors in

estimation of the peak temperature on the receiver surface. To overcome this issue, a coupled optical-thermal-fluid model is developed using SolTrace, MATLAB and ANSYS Fluent to design and evaluate the performance of the tubes of the receiver using CFD. The results obtained in SolTrace are coupled with ANSYS Fluent using a MATLAB code that generates a file which is used as a boundary condition (heat flux/heat generation) in ANSYS Fluent.

The novel coupled modelling methodology is demonstrated in figure 5.1 and is explained in further detail in the optical modelling sub-section of this study. Note that the tube shape in figure 5.1 is for representation of the methodology only.

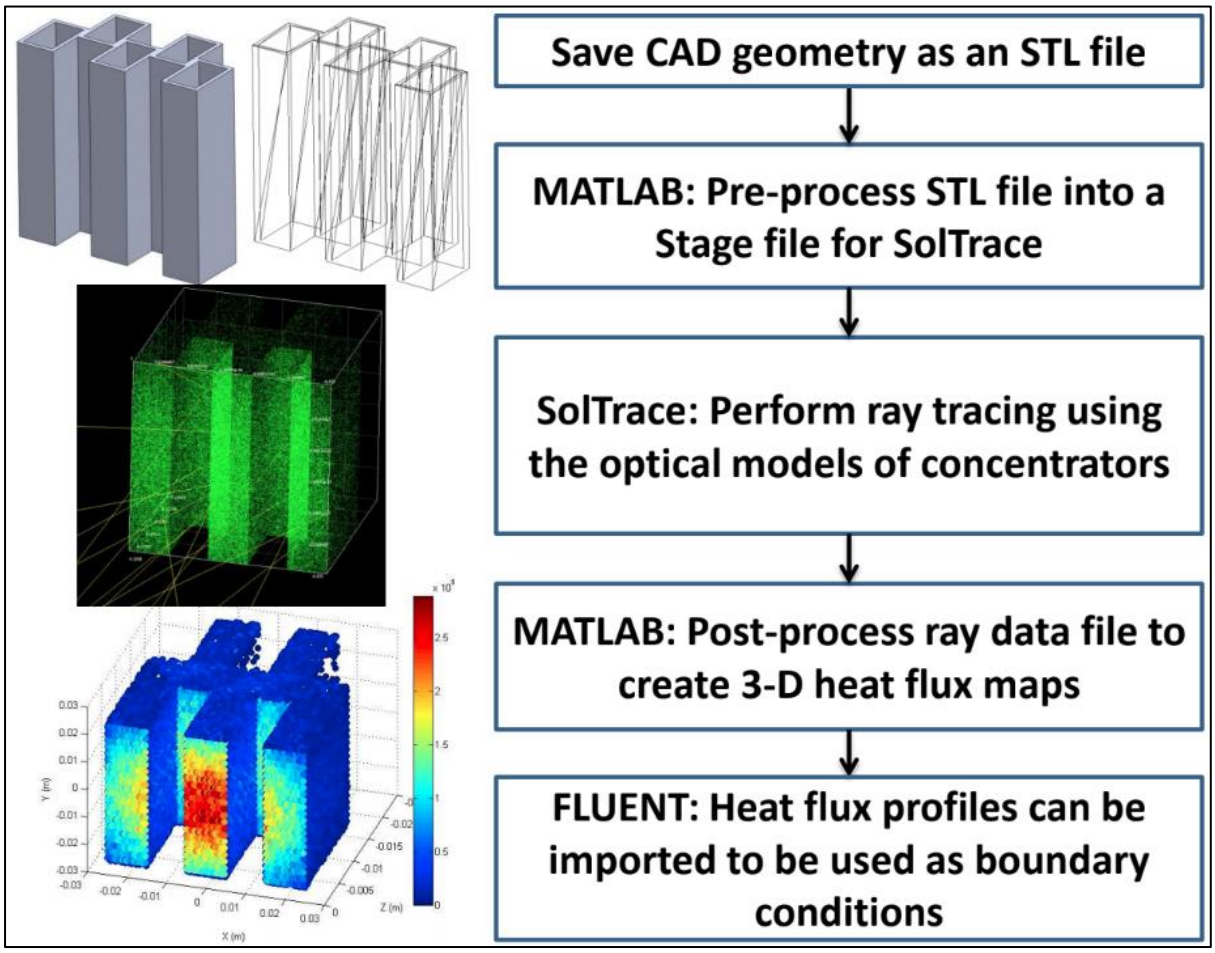

Fig. 5.1: Coupled modelling methodology for accurate mapping of real heat flux on receiver surface

5.2.3. Geometry

The receiver geometry consists of 5 straight parallel tubes placed next to each other; each tube of length 2 m. The effect of having a staggered arrangement is studied using the geometry shown in figures 5.2-5.5. Every alternate tube is shifted in the front so as to form some angle with the tubes at the rear. Offsets of 0, 15, 30 and 45 degrees are analysed in this study. All tubes have an outer diameter of 12.7 mm and a thickness of 2.76 mm. The gap between the outer walls of the tube is ignored for modelling purposes.

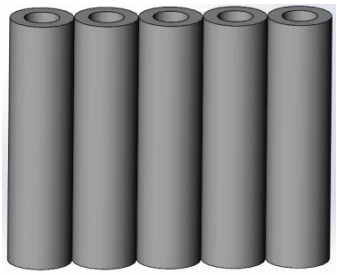

Fig. 5.2: Tubes with 0 degree offset

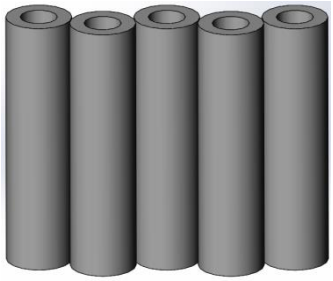

Fig. 5.3: Tubes with 15 degree offset

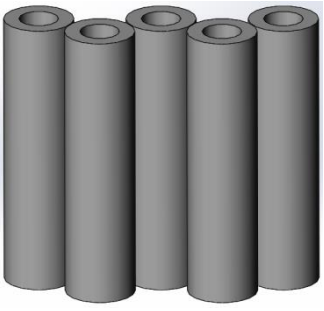

Fig. 5.4: Tubes with 30 degree offset

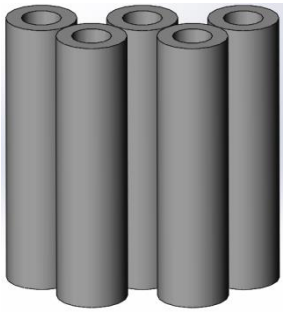

Fig. 5.5: Tubes with 45 degree offset

5.2.4. Optical Model

The heliostat field in the National Solar Thermal Test Facility (NSTTF) at Sandia National Laboratories, Albuquerque, US has been modelled in SolTrace, along with the receiver geometries mentioned in the previous section. SolTrace is an optical modelling software developed by NREL, which uses the Monte-Carlo Ray tracing methodology for prediction of intensity distribution of ray intersections on a surface [77]. The results of a typical ray trace for the full receiver and a typical heat flux distribution on a single receiver tube surface are shown in figures 5.6 (a) and 5.6 (b), respectively. The reflectivity of the tubes is specified as 0.04, assuming that Pyromark 2500 coating is applied [3]. The flux profiles obtained as a result of this optical modelling are manipulated using a MATLAB code. The MATLAB code operates on the planar flux profile obtained from SolTrace and maps it to the actual 3-dimensional geometry (figure 5.7). The Direct Normal Insolation (DNI) from the sun is assumed to be constant at 1000 W/m^2.

This is the first time that ray-trace results have been coupled to Fluent for analysis of a direct tubular receiver. Such coupling is expected to yield highly accurate prediction of results and bridge the gap between modelling and reality, as opposed to a constant heat flux distribution which has been conventionally used by researchers.

5.2.5. CFD Modelling

A hybrid mesh with hexahedral and tetrahedral elements is generated using ANSYS 14 Workbench. Equations describing mass, momentum and energy transport, the 2 equation SST k-ω turbulence model and the Discrete Ordinates Method (DOM) for radiation are solved

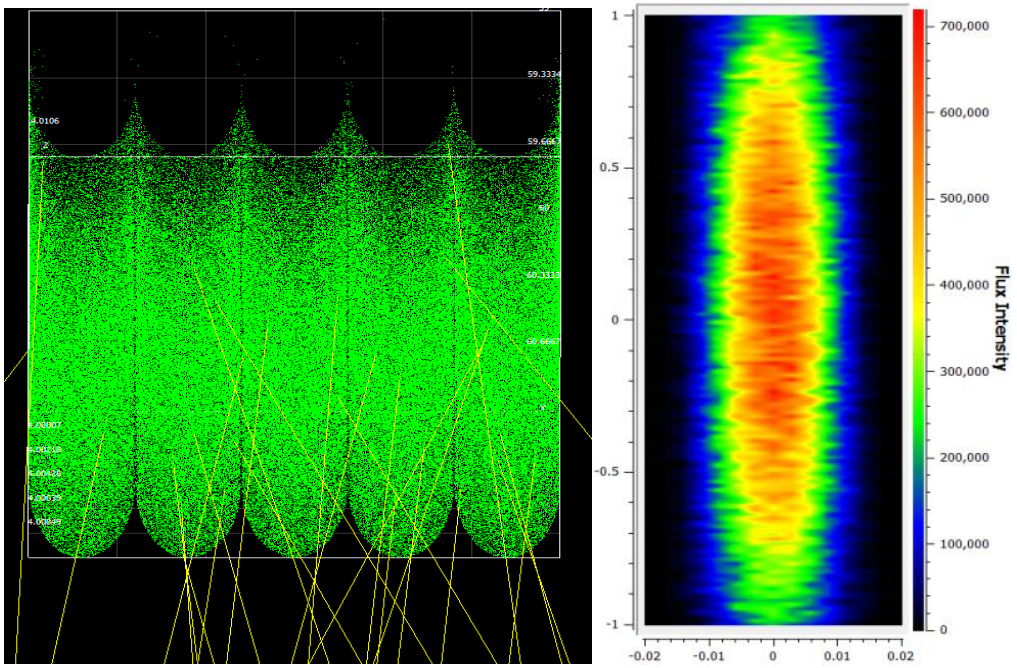

Fig. 5.6: a) SolTrace ray intersections and b) typical heat flux distribution on a tube surface

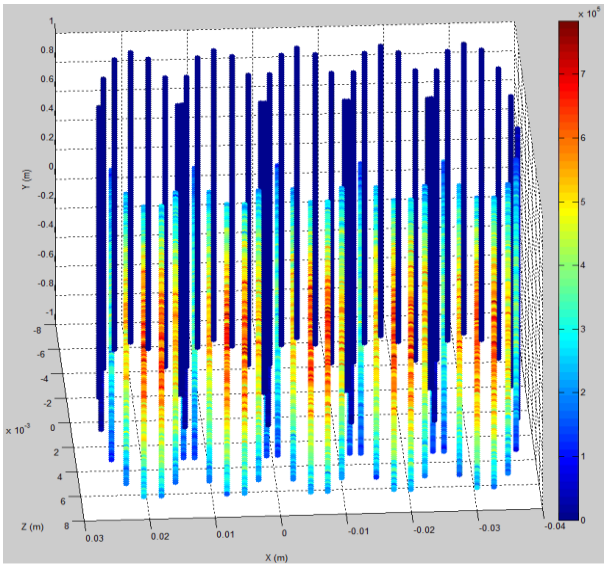

Fig. 5.7: Heat flux bins mapped from 2-D to 3-D space

using ANSYS Fluent 14, which uses the finite volume method to discretize the transport equations. The steady state, pressure based solver using SIMPLE algorithm and second-order upwind for spatial discretization is used for the simulation. The grid is refined until doubling the number of grid points yielded less than 0.2% difference in the solution parameters. Figure 5.8 shows the final grid consisting of ~$3.3x10^6$ cells. Mass flux, energy flux and scaled residuals are continuously monitored as the solution developed, and convergence is assumed only when the quantities of interest exhibit negligible variation and the scaled residuals for all equations dropped to at least below 10^{-3} and remained constant thereafter.

To obtain accurate thermo-physical properties for s-CO_2, Fluent is linked to REFPROP, which is a database provided by NIST [63]. The equation of state for CO_2 provided by Span and Wagner is used by this database [64].

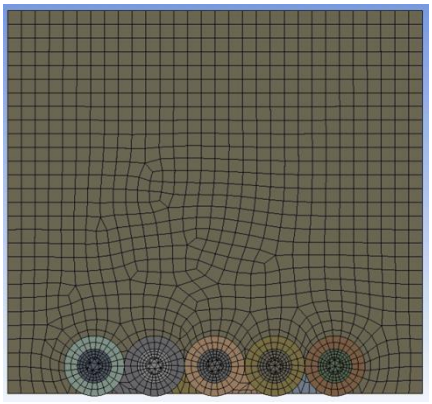

Fig. 5.8: Mesh (Top view of domain)

The SST k-ω model is more accurate and reliable for a wider class of flows because the wall boundary conditions for the k equation in the k-ω models are treated in the same way as the k equation is treated when enhanced wall treatments are used with k- ε models. This means that all boundary conditions for wall-function (coarse) meshes will correspond to the wall function approach, which is the mesh type used as shown in figure 5.8.

A grey-body model is implemented to capture the radiation interaction between the tubes and the environment. The outer walls of the tube are assumed to have a constant average emissivity of 0.86 assuming that a Pyromark 2500 coating is applied [3]. The inner surface of

the tubes is assumed to have a constant emissivity of 0.8, and the participation effect of s-CO_2 is neglected on account of the relatively high Reynolds number turbulent flow.

The actual flux distribution profile obtained from the processing of SolTrace output in MATLAB is applied as a heat generation profile boundary condition on the heated walls of the tube. This enables the coupling of the external air domain with the internal domains of the tube thickness and fluid domain containing s-CO_2.

Three different cases are analysed for the four geometries, and are described in table 5.1. A uniform constant mass flow rate is specified to each tube and its value is calculated such that the bulk average outlet temperature for different irradiances is obtained around the desired value. All simulations are carried out for an operating pressure of 20 MPa and receiver inlet temperature of 763 K.

Table 5.1: Conditions for the three different cases

Case	Mass Flow Per Tube (kg/s)	Peak Flux (kW/m^2)	Target Inlet/Outlet Temperature (K)
1	0.0294	~400	763/923
2	0.0526	~700	763/923
3	0.0769	~1000	763/923

The boundary conditions can be observed in figure 5.9. Note that the left side figure is the top view while the right side figure is an isometric view of the domain. The convective and radiative losses to the atmosphere are modelled using natural convection in the outer domain and the DOM radiation model in ANSYS Fluent. The ambient temperature is assumed as 300 K. Both, ambient cooling air and the heat transfer fluid (s-CO_2) molecules are assumed to be non-participating in the wavelength range of interest.

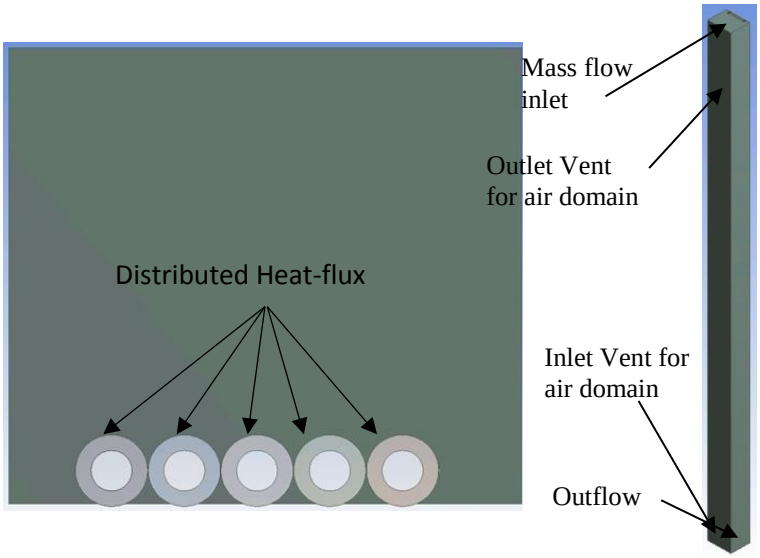

Fig. 5.9: Boundary conditions

5.2.6. Results and Discussion

The heat-flux distributions in figures 5.10-5.12 correspond to the NSTTF model from SolTrace, using a single aim-point strategy in the center of the receiver. By applying more aim points, the heat-flux distribution can be controlled, resulting in a more monotonously varying temperature distribution on the surface.

From figures 5.10-5.12, it can be observed that even though the outlet temperature is kept constant by increasing the mass flow rate proportionally to the applied heat flux, the wall-temperature increases due to the increase in heat flux for the same heat transfer area. This means that the heat transfer coefficient does not increase proportionally with the flow rate and with increasing incident power. The peak tube wall temperature predicted in this study is 1150 K.

Three different cases are analyzed for the four geometries which have different offsets. As previously mentioned, the idea behind employing the staggered arrangement is to increase the receiver efficiency by light trapping using the tubular surfaces. Figures 5.13 (a) and 5.13 (b) show the receiver efficiency and the corresponding radiative and convective losses for each case.

Radiative losses account for approximately 10-19% while convective losses account for approximately 1-10% of the total heat transfer as observed in figure 5.13 (b).

A receiver efficiency as high as 85 % is predicted for the peak concentration of 1000 kW/m^2. Although this concentration is achievable, most likely this would lead to tube surface temperatures above the temperature limits at the high pressure under consideration for s-CO_2. Therefore, an optimal peak flux must be determined. It is important to consider the material limitations at high temperatures to avoid creep rupture.

By selecting a stronger material or increasing the thickness of the tubes, the life of the receiver can be extended. Nonetheless, increasing the thickness of the tubes increases the thermal gradient on the tube wall, resulting in an increase in the thermal stress while reducing the absorbed heat.

As observed from figure 5.13, staggering of tubes did not yield improvement in the receiver efficiency. In fact, the efficiency values for any power level are lowest for the 45 degree offset case. This is due to the fact that the staggered tubes exhibit a strong shielding effect for the tubes at the back. Rather than recapture of re-radiation from emission to adjacent tubes, the optical efficiency is instead hampered due to staggering and there is a risk that the tubes at the front may get overheated. To avoid overheating, the tubes in front would need to have a larger flow rate compared to the tubes at the back.

For 0 degree offset with a DNI of 1000 W/m^2, a case with constant heat flux instead of the non-uniform distribution from SolTrace is simulated. The total power input is specified to be same, but the value of peak flux intensity is only about 40 % in the uniform distribution case in comparison to the non-uniform real distribution obtained from SolTrace for the NSTTF heliostat field.

The predicted receiver efficiency is higher in the case of the uniform flux distribution case only by 0.5 %. An important observation is that the predicted peak temperature on the uniformly heated walls is 1087 K, while in the case of actual heat flux distribution from SolTrace, it is 1153 K. In different conditions, the need to map actual heat flux instead of using a constant heat flux approximation might be even more significant if an accurate prediction of the temperature distribution is desired.

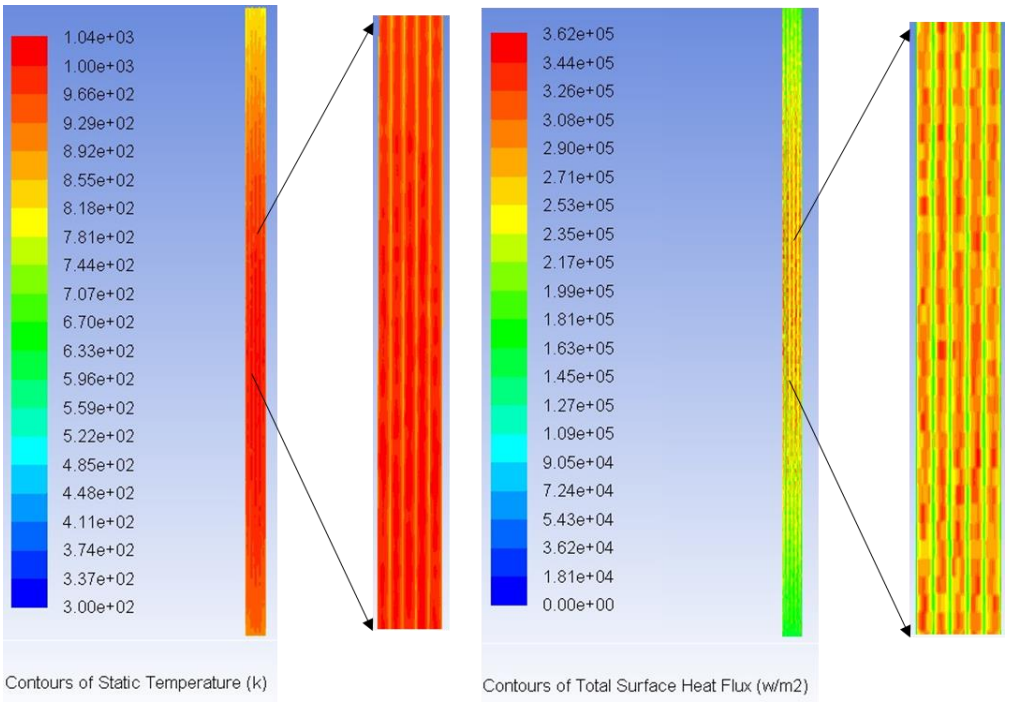

Fig. 5.10: Temperature and heat flux contours for 0 degree offset and ~400 kW/m^2 peak flux

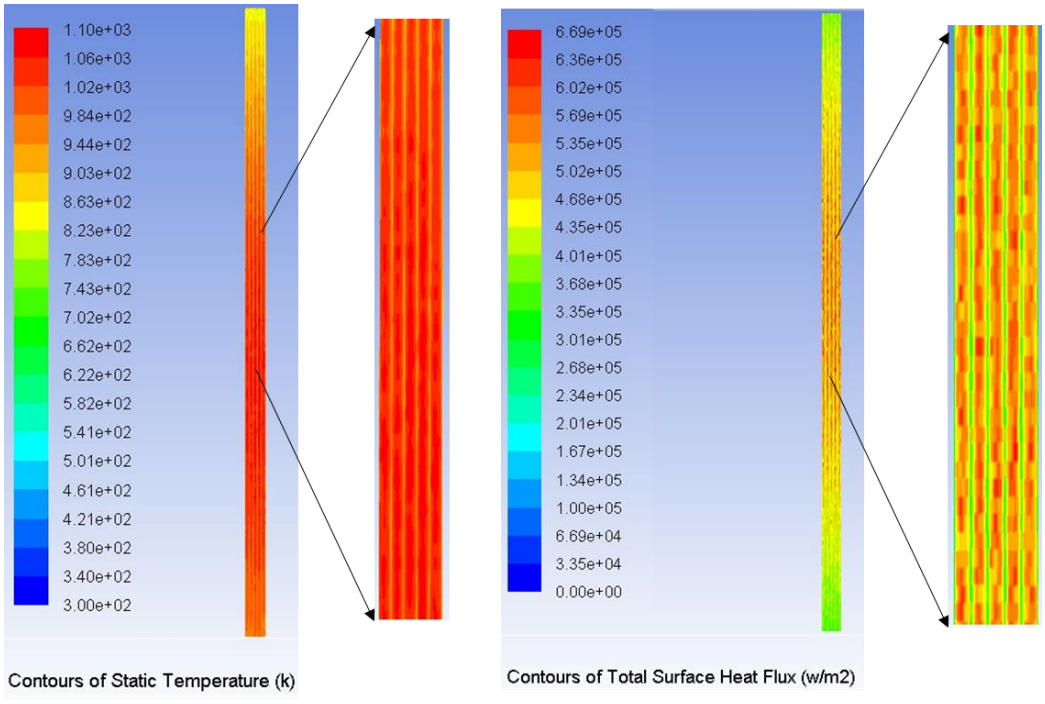

Fig. 5.11: Temperature and heat flux contours for 0 degree offset and ~700 kW/m^2 peak flux

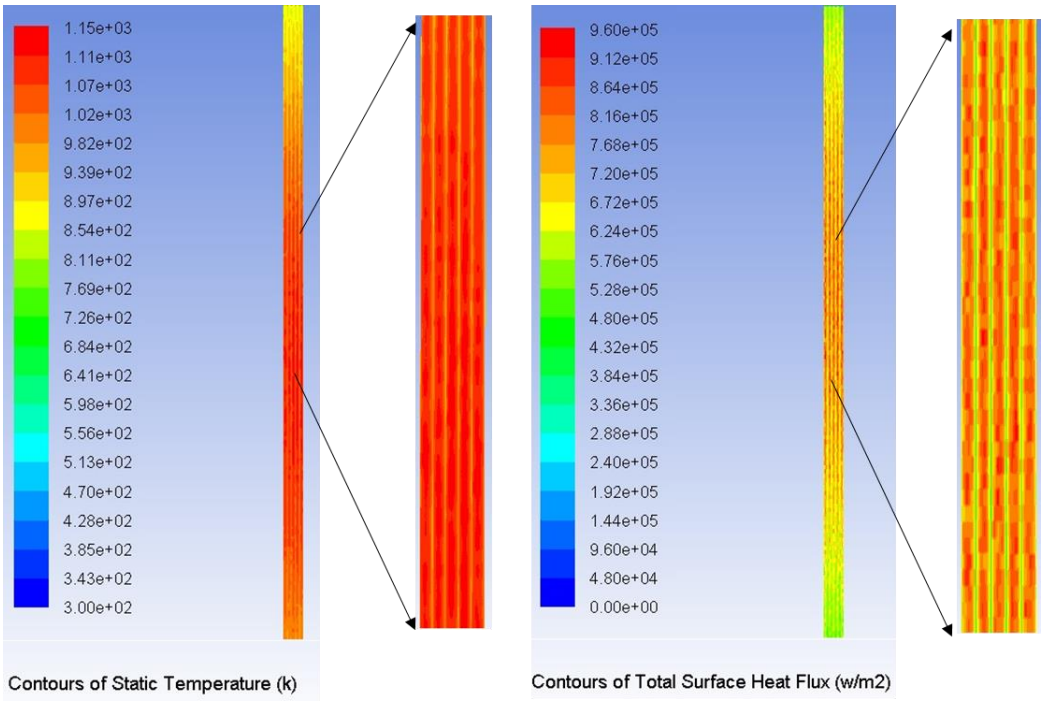

Fig. 5.12: Temperature and heat flux contours for 0 degree offset and ~1000 kW/m^2 peak flux

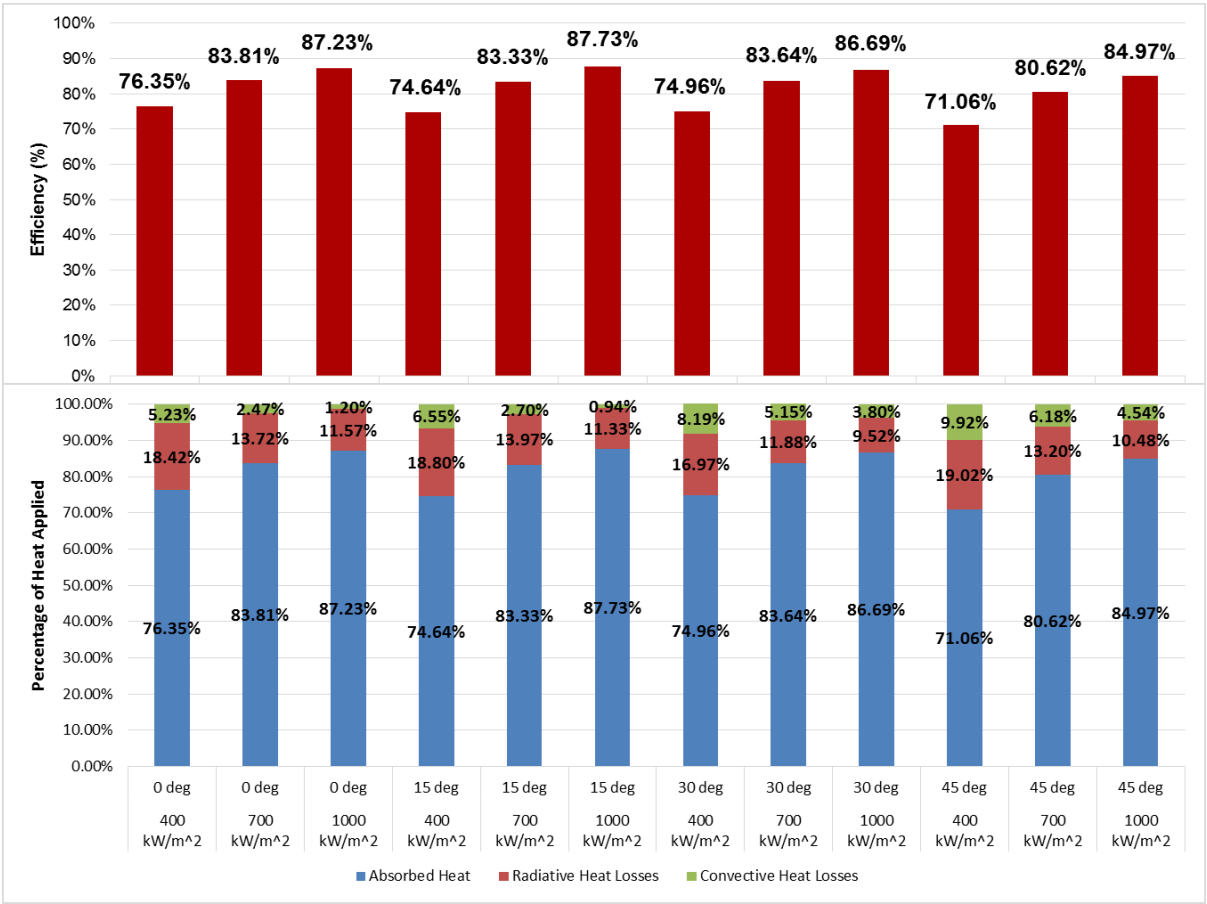

Fig. 5.13: a) Thermal efficiency of the twelve cases and b) Heat losses of the twelve cases

5.3. DETAILED ANALYSIS AND DESIGN OF s-CO_2 TUBULAR RECEIVER PANELS

In this study, the coupled optical-thermal-fluid modelling methodology discussed in the preceding analysis is used to evaluate the direct tubular s-CO_2 receiver thermal performance when exposed to a concentrated solar input in the power range of 0.3-0.5 MW. Ray tracing is performed using SolTrace to determine the heat flux profile on the receiver and CFD analysis is used to determine the thermal-fluid performance of the receiver under the specified heating conditions. The MATLAB code developed for coupling SolTrace and ANSYS Fluent is utilized to obtain appropriate boundary condition file. CFD modeling is performed using ANSYS Fluent to predict the thermal performance of the receiver by evaluating radiation and convection heat loss mechanisms for four receiver panels placed adjacent to each other, each panel containing 10 tubes, as detailed in the following sections. Understanding the effects of variation in heliostat aiming strategy, recirculation of flow within panels, and flux levels on the thermal performance of the receiver is achieved through parametric analyses in this study.

5.3.1. Geometry

The simplified receiver geometry (figure 5.14) is obtained from the actual receiver geometry (figure 5.15) for performing the optical-thermal-fluid analysis. The simplified geometry consists of 80 straight parallel tubes, each of length 1 m, having an outside diameter of 12.5 mm and a wall thickness of 2.1 mm. Use of 80 tubes is intended to maintain an aperture of 1 m^2. As found in the initial study in the preceding sections, staggered tube arrangements did not exhibit a favorable effect on the receiver efficiency; the tubes are arranged in a straight line without offset. The 80 tubes are divided into groups of 20 for representing the four panels with 20 tubes each. Figure 5.15 shows that each panel consists of 20 tubes attached to headers at the top and bottom, whose function is to distribute the total s-CO_2 flow evenly amongst the panel tubes. Figure 5.15 shows the complete receiver geometry consisting of 4 panels. Recirculation amongst panels is investigated to generate several flow patterns which could lead to higher receiver efficiency.

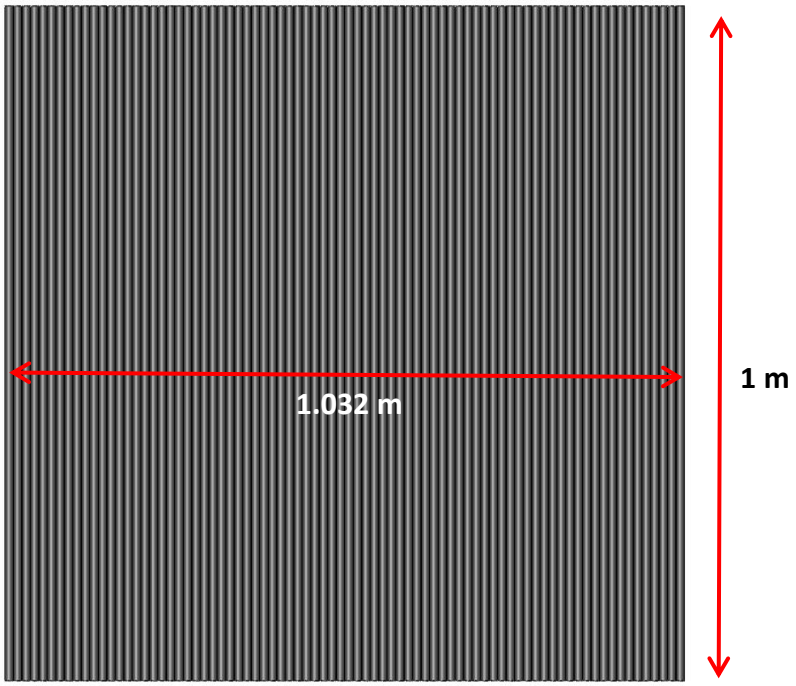

Fig. 5.14: Simplified receiver geometry for analysis

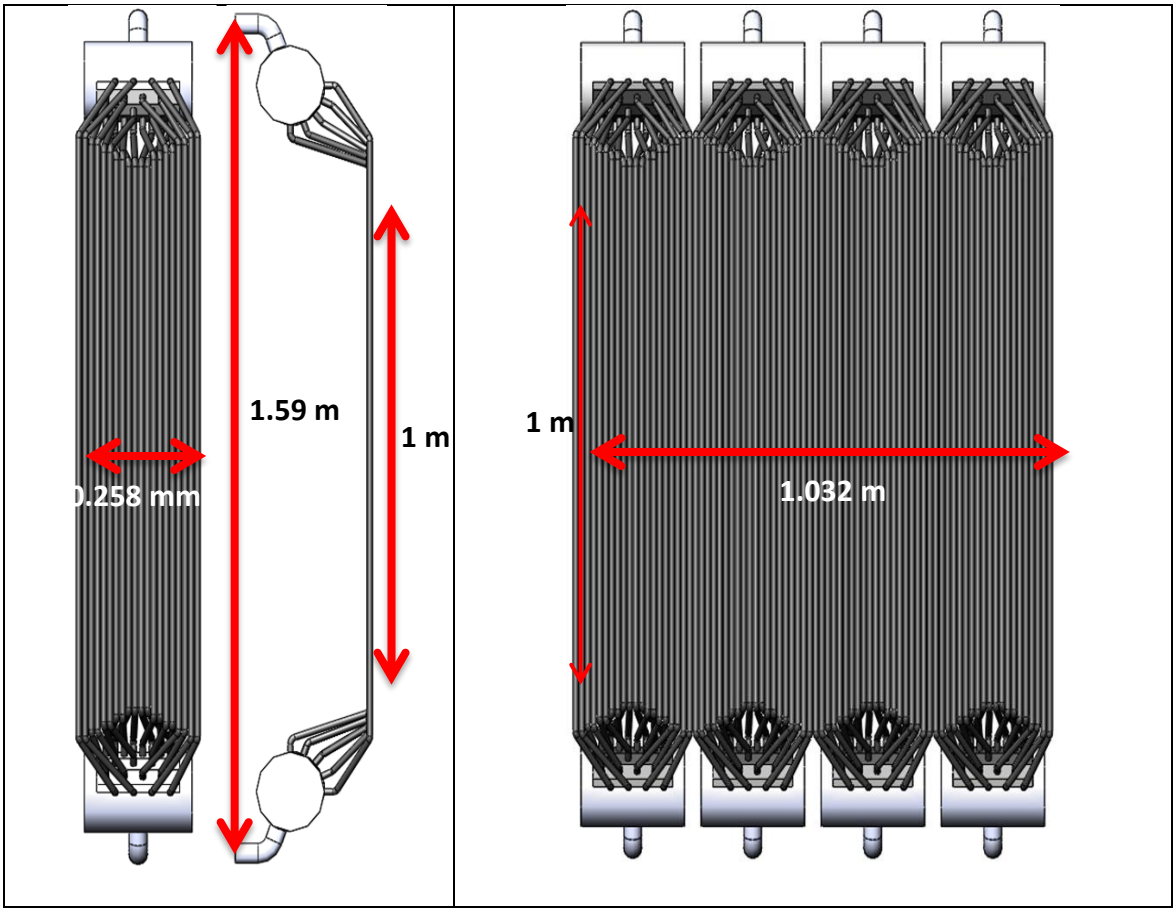

Fig. 5.15: a) Dimensions and connectivity of tubes and headers, b) Full receiver

5.3.2. Optical ray-tracing modelling

Figure 5.16 shows the heliostat field from the NSTTF, Sandia National Laboratories; US modelled in SolTrace, along with the receiver geometry at the focal target. A large number of random rays are generated in SolTrace to simulate the incoming rays from sun, interaction with heliostat field and receiver. The rays can undergo multiple reflections within the domain and simulate complex optics.

Due to size of the receiver considered, the amount of irradiance spillage is not considered for the calculation of optical efficiency which is calculated using equation 5.1:

$$\eta_{\text{opt}} = \frac{\dot{Q}_{surf}}{\dot{Q}_{in}} \qquad \text{(…Eqn. 5.1)}$$

where η_{opt} is the optical efficiency which represents the effective absorptance of the receiver, $\dot{Q}_{surf}$ is the power absorbed by the receiver surface and $\dot{Q}_{in}$ is the incident power on the receiver surface.

The reflectivity of the receiver surface is specified as 0.1, assuming the surface to be oxidized Inconel [78]. Figure 5.17 shows the locations of the aim-points with respect to the aperture. Two extreme aim point strategies are chosen to observe the effect on receiver efficiency, one with a central aim point, while the second strategy involving 4 aim points close to the four corners of the aperture. Figure 5.18 shows the results of ray tracing based heat flux distributions on a flat receiver aperture for the specified aiming strategies and two different power levels under consideration.

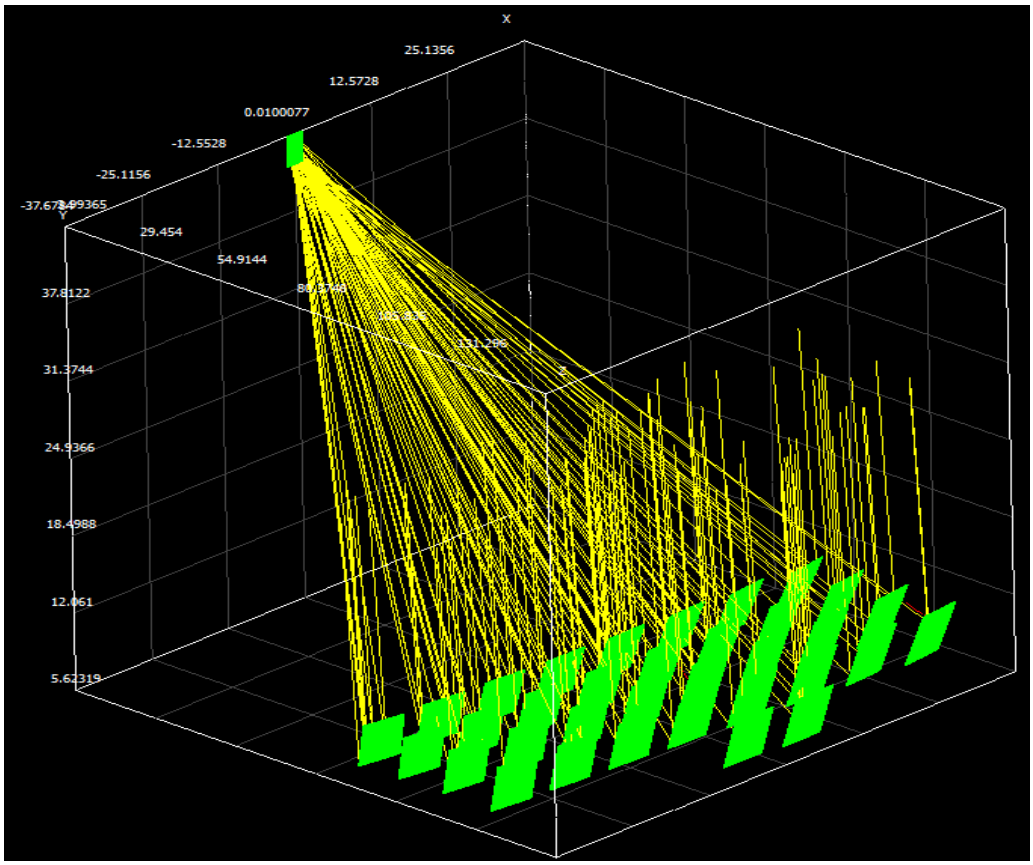

Fig. 5.16: Ray-trace analysis performed using the NSTTF heliostat field

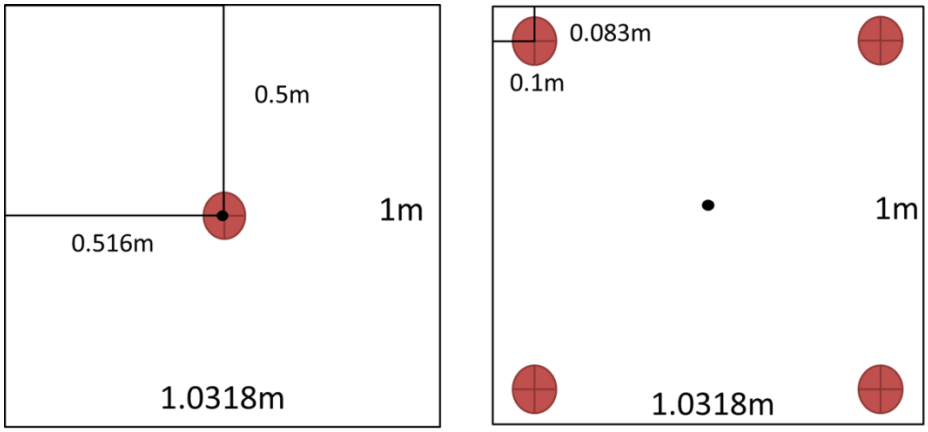

Fig. 5.17: Single aim-point and four aim-point strategies

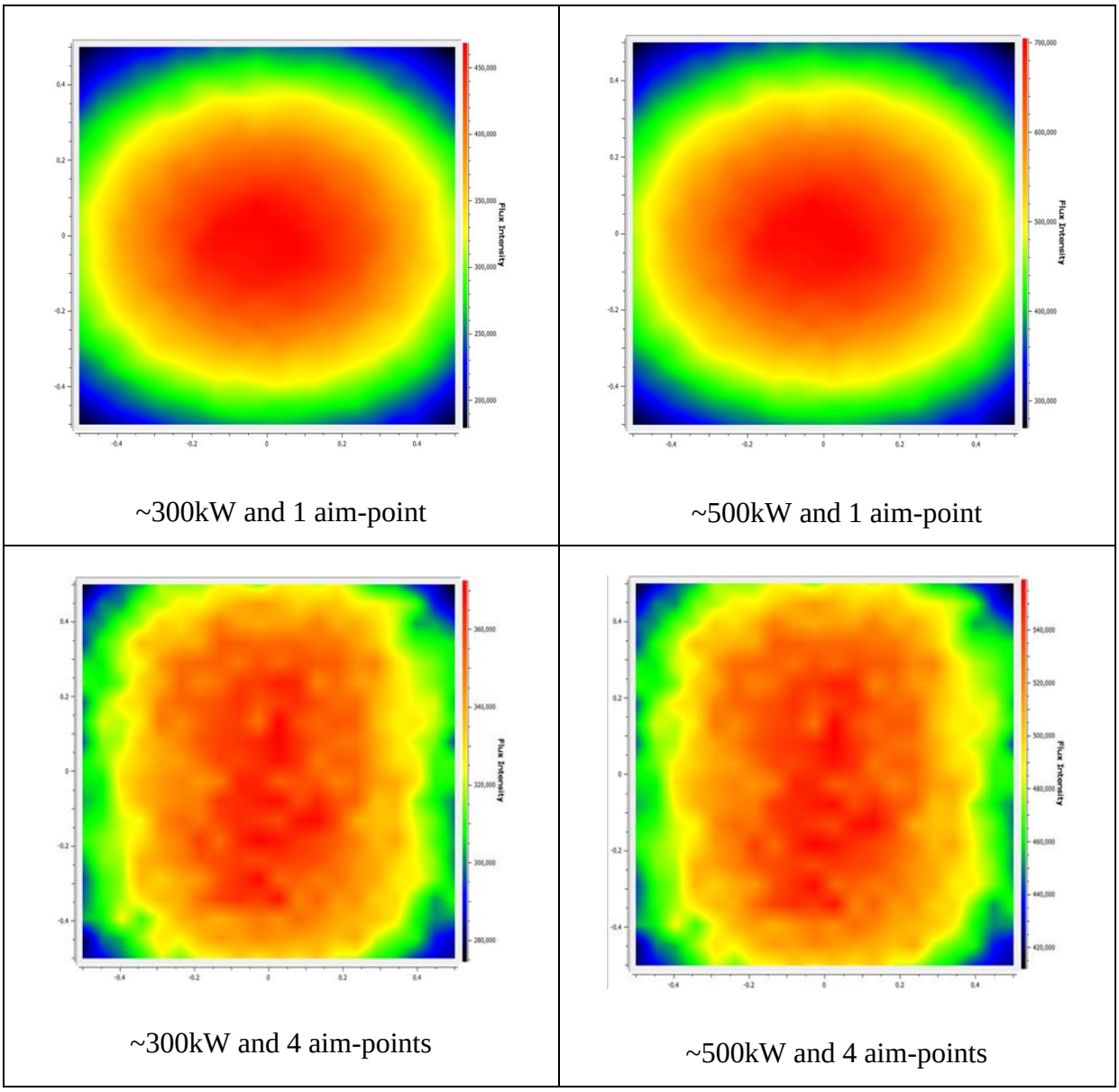

Fig. 5.18: Heat flux distribution for two selected aim-point strategies and power levels

The ray-tracing is completed using the geometries of the actual receiver tubes and the novel methodology described in the preceding analysis.

5.3.3. Computational Fluid Dynamics (CFD) Modeling

A non-uniform hexahedral mesh consisting of around $5x10^6$ cells is generated using ANSYS 16 meshing, as shown in figure 5.19. The grid has two special characteristics:

a) 2 elements are used along the thickness of the tube to account for accurately modeling the conduction heat transfer through the tube wall (considering conjugate heat transfer).
b) a single inflation layer is used to model the near-wall region of the tube and fluid.
The equations describing mass, momentum and energy transport, and the two-equation SST (Shear Stress Transport) k-ω turbulence model are solved using ANSYS Fluent 16, which uses the finite volume method to discretize the transport equations. The steady state, pressure based solver using SIMPLE algorithm and second-order upwind for spatial discretization is used for the simulation. Mass flux, energy flux and scaled residuals are continuously monitored as the solution develops, and convergence is assumed only when the quantities of interest exhibit negligible variation and the scaled residuals for all equations drop to at least below 10^{-3} and remained constant thereafter.

The thermo-physical properties of s-CO_2 are incorporated in the analysis in Fluent using the database provided by NIST [63]. The equation of state for CO_2 provided by Span and Wagner is used by this database [64].

5.3.3.1. Fluid Flow

Since the receiver has several panels, different flow configurations are designed to study the possibility of enhancing the receiver efficiency. The mass flow rate for each of the flow configurations is determined under the requirement of temperature rise ~160 K (i.e. 813 K inlet to 973 K outlet, approximately).

The SST k-ω turbulence model is used to solve for the turbulent flow inside the tubes. The model is more accurate and reliable for a wider class of flows because the wall boundary conditions for the k equation in the k-ω models are treated in the same way as the k equation is treated when enhanced wall treatments are used with the k- ε models. This means that all boundary conditions for wall-function (coarse) meshes will correspond to the wall function approach. Since the range of $30 \leq Y+ \leq 300$ is so extensive, a single element inflation layer can be used as long as the Y+ value is still inside the range. The mesh used for the analysis is shown in figure 5.19.

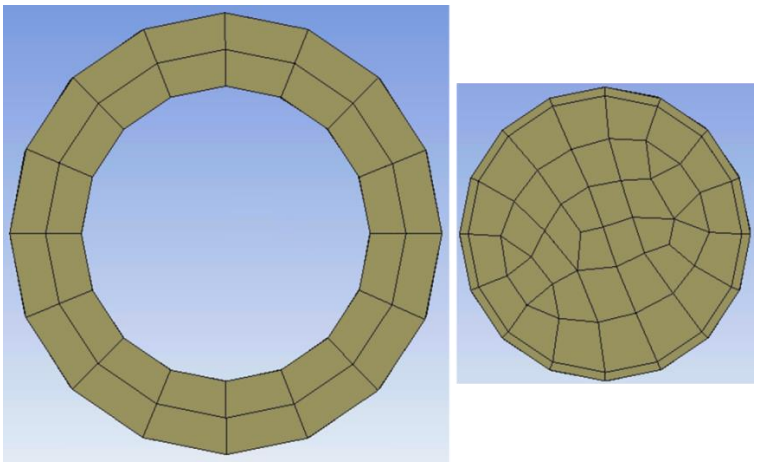

Fig. 5.19: a) Wall thickness mesh, b) Interior (fluid) region mesh

Figure 5.20 illustrates the six flow configurations that are analyzed in this study. Since the simplified geometry is modeled, the manifolds are not included and an equivalent recirculation boundary condition is used. However, a flow distribution effectiveness study for the headers is performed separately in order to confirm that the fluid flow is uniformly distributed in the manifold, and the findings are discussed in the results section. The pressure drop is investigated to ensure that the pressure drop is not substantial and within permissible limits. The importance of maintaining a low pressure drop from numerical analysis point of view is that the thermo-physical properties largely become functions of temperature change only. This is important because the recirculation boundary condition in ANSYS Fluent 16 cannot be used with the density based solver, which would have been a necessity if the pressure drop is significant.

The approximate mass flow rates of s-CO_2 mentioned in figure 5.20 vary depending on the incident power and the recirculation flow pattern. As seen in figure 5.20, flow 3 has no recirculation (four inlets and four outlets), flow 1 and flow 2 have two inlets and two outlets, while flow 4, flow 5 and flow 6 have only one inlet and one outlet for the receiver, employing maximum recirculation.

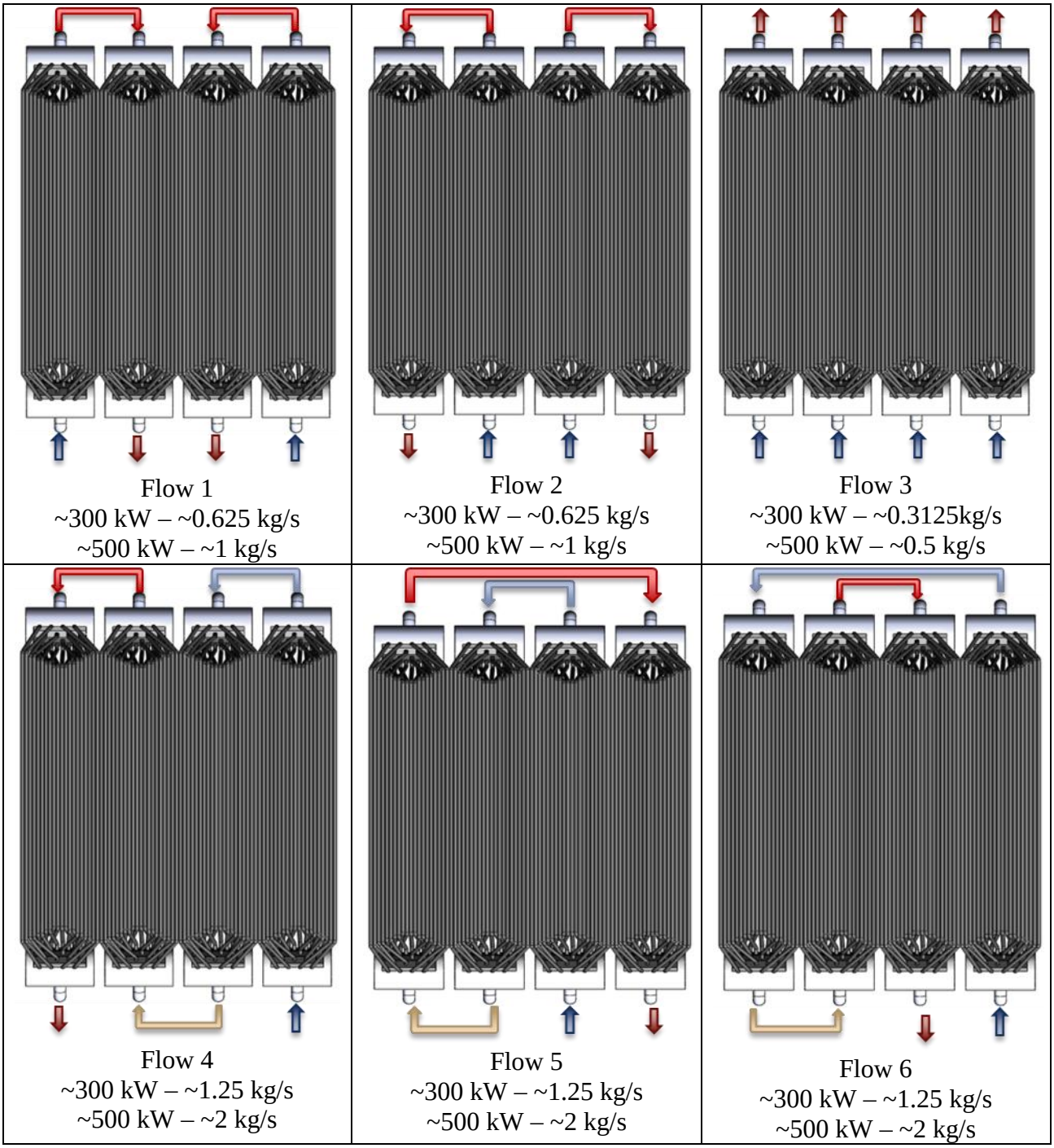

Fig. 5.20: Six recirculation patterns under investigation: Cold inlet (Blue) and Hot outlet (Red)

5.3.3.2. Conjugate Heat Transfer

A grey-body model is implemented to approximate the radiative losses between the tubes and the environment. The outer walls of the tube are assumed to have a constant emissivity of 0.76 assuming oxidized Inconel [78]. The model considers the radiative interaction between the tubes to be negligible. Two-elements on wall are found to be sufficient to yield grid independence for thermal conduction. The inner surfaces of the tubes are assumed to have a constant emissivity of 0.7. As the flow in the tubes for the current condition is high Re turbulent flow, radiation effects of s-CO_2 are neglected. Hence s-CO_2 is considered as a non-participating medium. Convective losses by natural convection are calculated by assuming a constant heat transfer coefficient of 10 W/m^2-K (estimated from analysis presented in section 5.2) at ambient conditions.

The heat flux distribution profile obtained from the processing of SolTrace output is applied as a heat generation profile boundary condition on the heated walls of the tube. This enables the coupling of mixed thermal losses boundary condition with the internal domains consisting of tube thickness and fluid volume containing s-CO_2.

5.3.4 Results and Discussion

In this section, the results for flow distribution through manifolds and pressure drop through s-CO_2 tubes is presented first, followed by discussion on numerically obtained receiver efficiency and temperature distribution on the irradiated surface of the tubes.

5.3.4.1. Flow distribution at the manifolds

As mentioned in section 5.3.1, the receiver panels require a set of headers that distribute the flow to the 20 tubes connected to them. Figure 5.21 shows the manifold design used for the analysis. The goal of the flow distribution study is to determine the average distribution in each of the 20 tubes to ensure validity of simplified model suggested in figure 5.14.

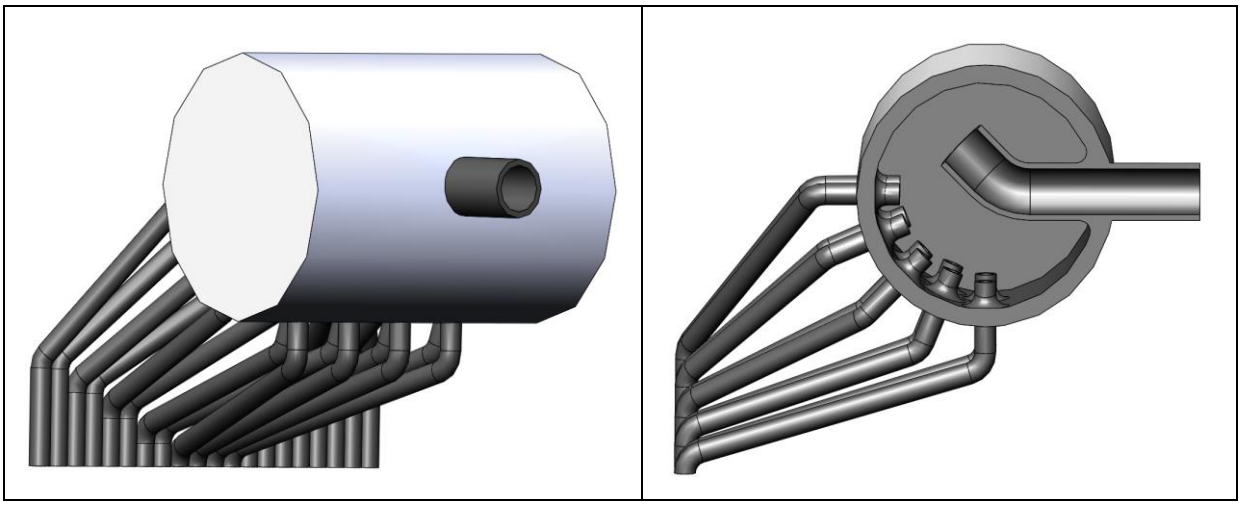

Fig. 5.21: Manifold (header) design used for the receiver panels

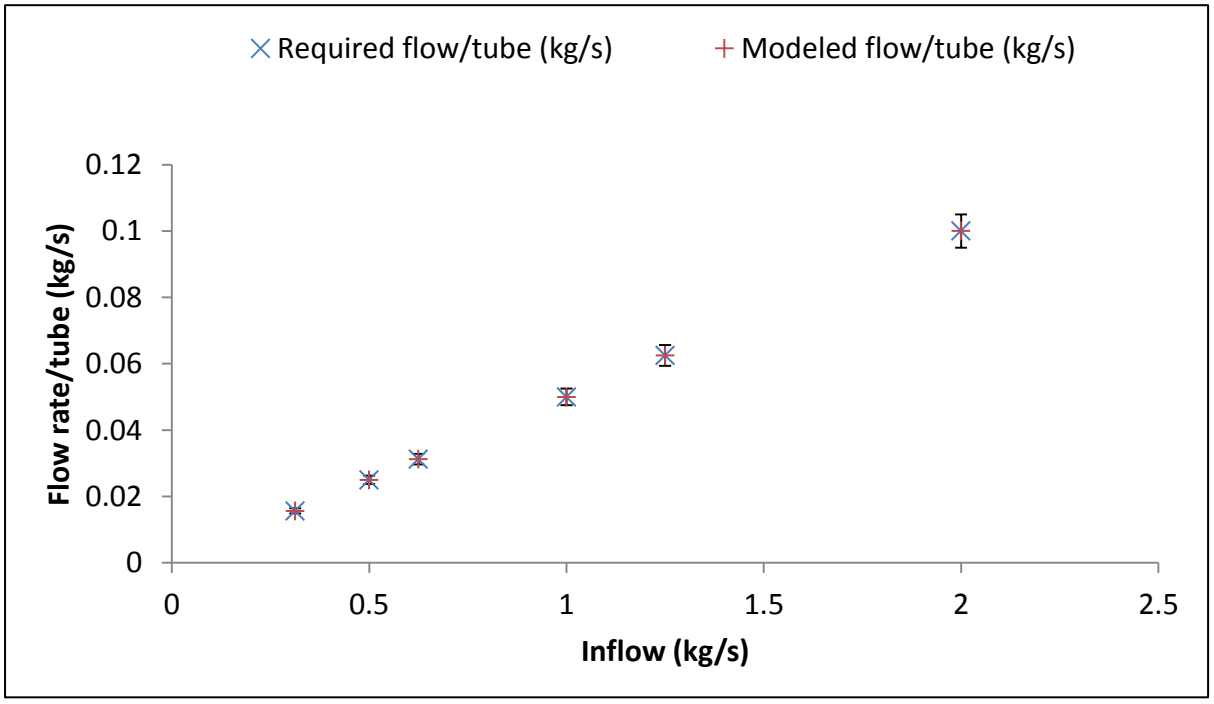

Fig. 5.22: Flow distribution across the manifold with one inflow and 20 outflow tubes

Figure 5.22 compares the required flow rate per tube for a given inflow mass flow rate and the average mass flow rate per tube from the model. The results confirm the validity of the simplified version of the geometry which assumes uniform mass flow distribution in a single panel, i.e. 20 tubes. The required flow rate per tube in figure 5.22 is obtained by dividing the total inflow mass flow rate by the number of tubes attached to the panel (i.e. 20). It is found

that the maximum variation in flow rates does not exceed 10% of the average value for every case, and is represented in figure 5.22 using the error bars.

5.3.4.2. Pressure drop across the receiver

The pressure drop across the inflow and outflow manifolds is investigated to find the relationship of the pressure drop across the manifold as a function of the inflow and outflow mass flow rates. For the study, s-CO_2 is at its maximum expected temperature (973 K), since this will yield the worst case scenario for the pressure drop. Figures 5.23 and 5.24 display the relationships of pressure drop to inflow and outflow flow rates, respectively. It must be noted that these values are for only one flow across the inlet and outlet header.

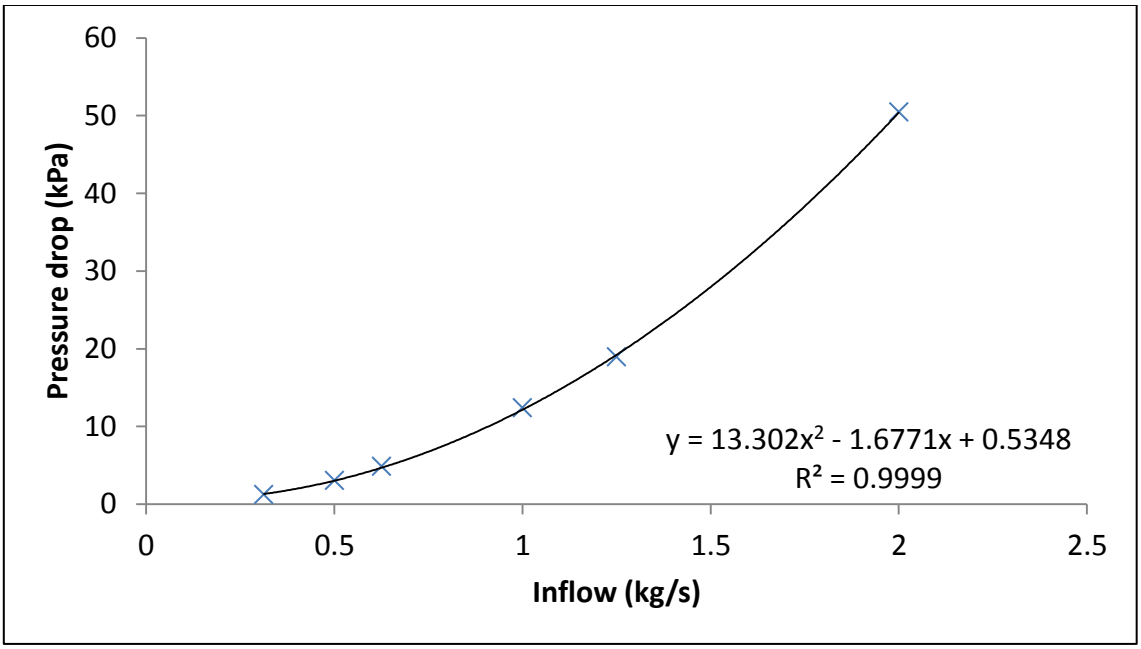

Fig. 5.23: Pressure drop across the manifold with a single inflow and 20 outflow tubes

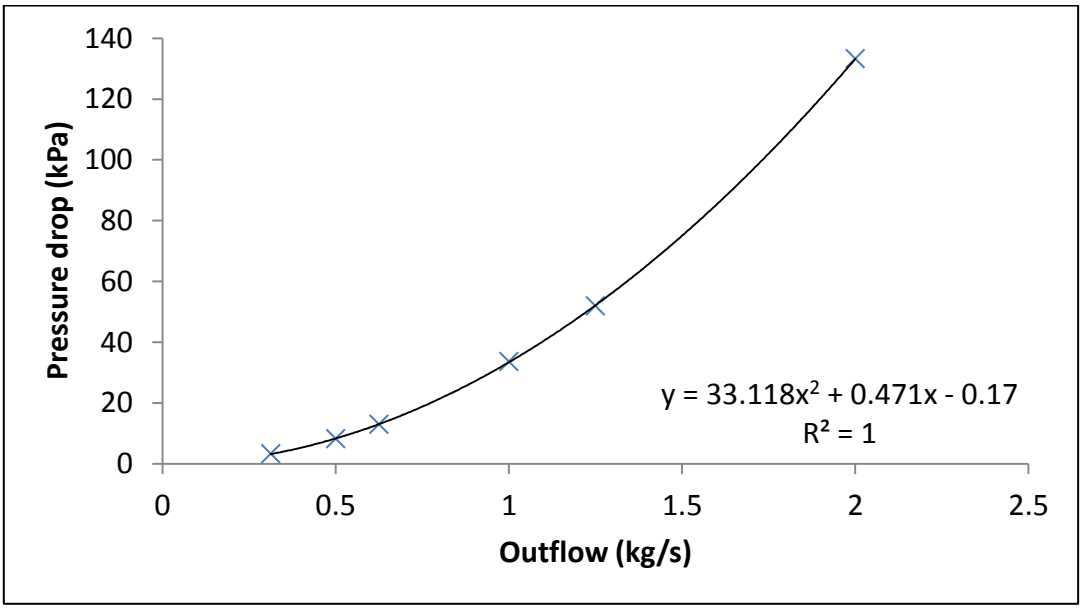

Fig. 5.24: Pressure drop across the manifold with 20 inflow tubes and a single outflow

The frictional losses inside each tube are estimated assuming s-CO_2 at its maximum temperature (973 K). Figure 5.25 shows the relationship of the pressure drop and the mass flow rate per tube.

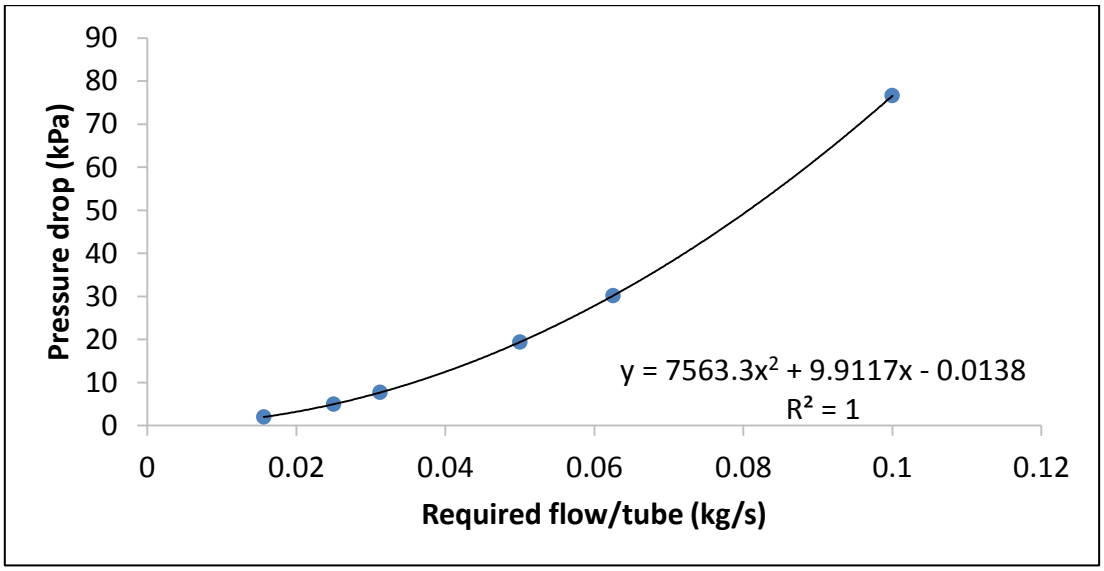

Fig. 5.25: Pressure drop across a single tube as function of the required flow rate

The results of the pressure drop analysis provide a conservative (i.e. upper limit) insight of the pressure drop across the elements of a single panel. It is obvious that applying the least amount of recirculation from panel to panel yields the lowest pressure drop across the receiver for a fixed flow rate.

5.3.4.3. Receiver Efficiency

The thermal efficiency is calculated using equation 5.2:

$$\eta_{\mathrm{th}} = \frac{\dot{Q}_{abs}}{\dot{Q}_{surf}} \qquad (\ldots \text{Eqn. 5.2})$$

where η_{th} is the thermal efficiency of the receiver, $\dot{\mathrm{Q}}_{\mathrm{surf}}$ is the power absorbed by the receiver surface and $\dot{\mathrm{Q}}_{\mathrm{abs}}$ is the power absorbed by the heat transfer fluid.

Consequently, $\dot{\mathrm{Q}}_{\mathrm{abs}}$ is defined by the difference of the power absorbed by the receiver surface and the radiative and convective losses as functions of the surface temperature, as described in equations 5.3-5.5 below:

$$\dot{Q}_{abs} = \dot{Q}_{surf} - \dot{Q}_{rad} - \dot{Q}_{conv} \qquad (\ldots \text{Eqn. 5.3})$$

$$\dot{Q}_{rad} = \varepsilon\sigma A\left({T_{surf}}^4 - {T_{\infty}}^4\right) \qquad (\ldots \text{Eqn. 5.4})$$

$$\dot{Q}_{conv} = hA\left(T_{surf} - T_{\infty}\right) \qquad (\ldots \text{Eqn. 5.5})$$

where $\dot{Q}_{rad}$ is the heat radiated to the environment, $\dot{Q}_{conv}$ is the heat lost due to natural convection, ε is the thermal emissivity, σ is the Stephan-Boltzmann constant, A is the surface area, h is the heat transfer coefficient and T is the temperature at the surface and environment respectively. Following equations 5.3-5.5 and using the area-weighted average wall temperatures from ANYS Fluent, the heat losses are estimated. Figure 5.26 shows the thermal efficiency for different flow configurations, power levels and aim point strategies; it must be noted that these values represent the receiver thermal losses only.

To account for the reflective losses, the thermal efficiency must be multiplied by the optical efficiency to yield the overall receiver efficiency (figure 5.27)

$$\eta_{\mathrm{receiver}} = \eta_{\mathrm{opt}}\eta_{\mathrm{th}} \qquad (\ldots \text{Eqn. 5.6})$$

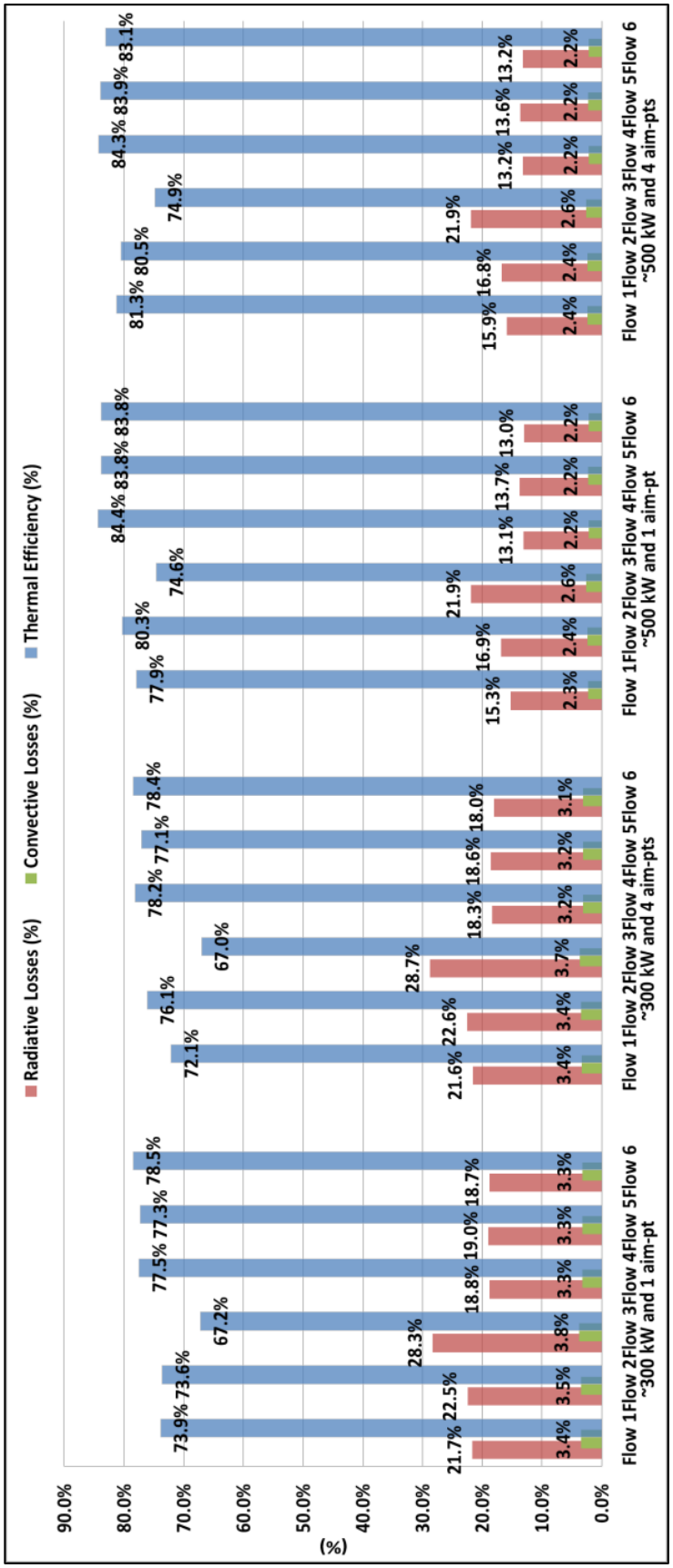

Fig. 5.26: Receiver Thermal Efficiency

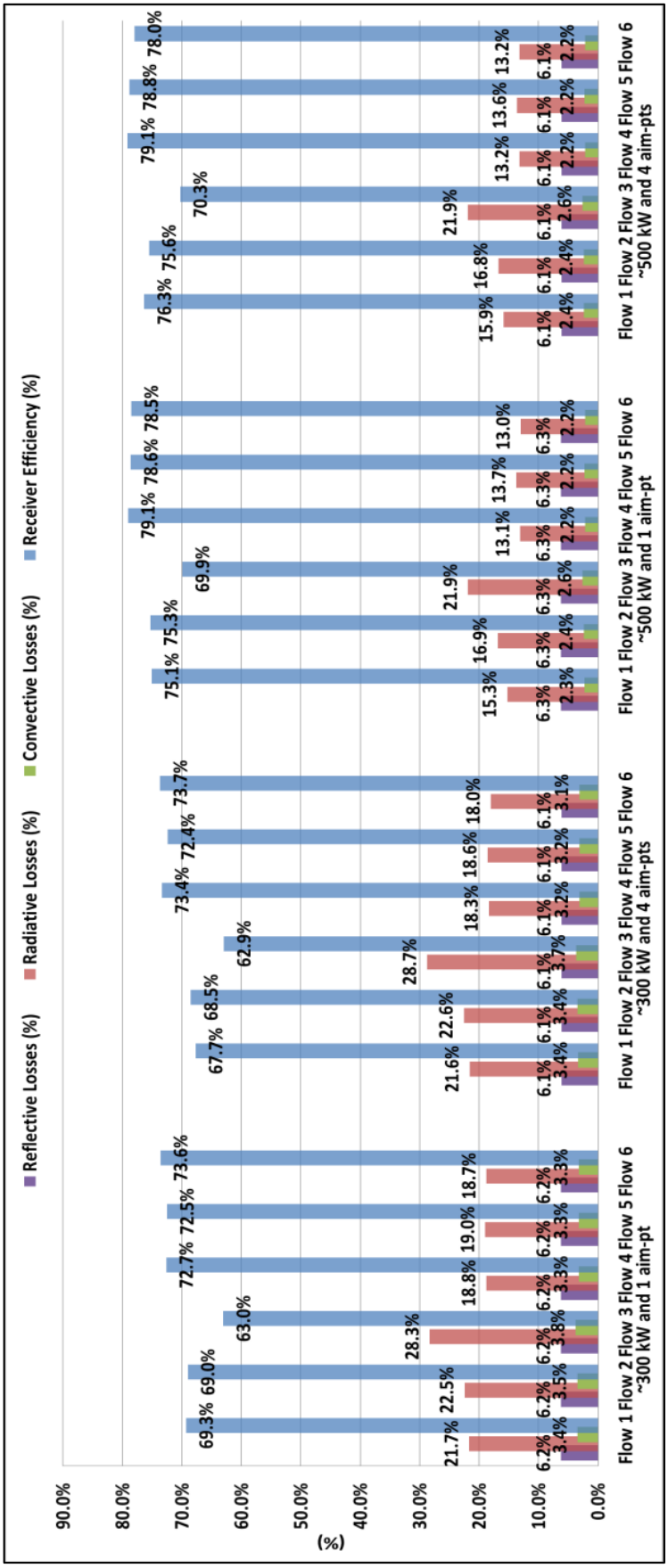

Fig. 5.27: Receiver Overall Efficiency (without considering spillage losses)

5.3.4.4. Temperature Contours

The temperature distribution along the receiver plays a very significant role in the thermal efficiency calculation. It is observed that using recirculation flow patterns can be advantageous for the thermal efficiency of the receiver. Figures 5.28 and 5.29 show the comparison of two cases where a 9% thermal efficiency increase is shown as a result of the flow recirculation conditions in flow 4.

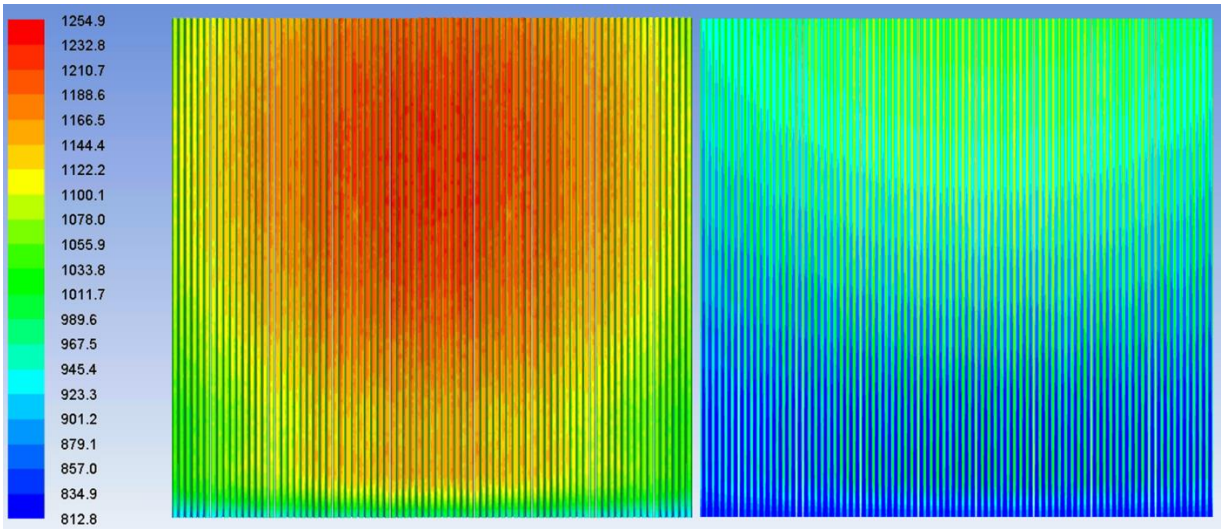

Fig. 5.28: Wall (left) and Center-Plane (right) Temperature Contours (in Kelvin) for Flow 3 with ~500 kW input and 4 aim-points

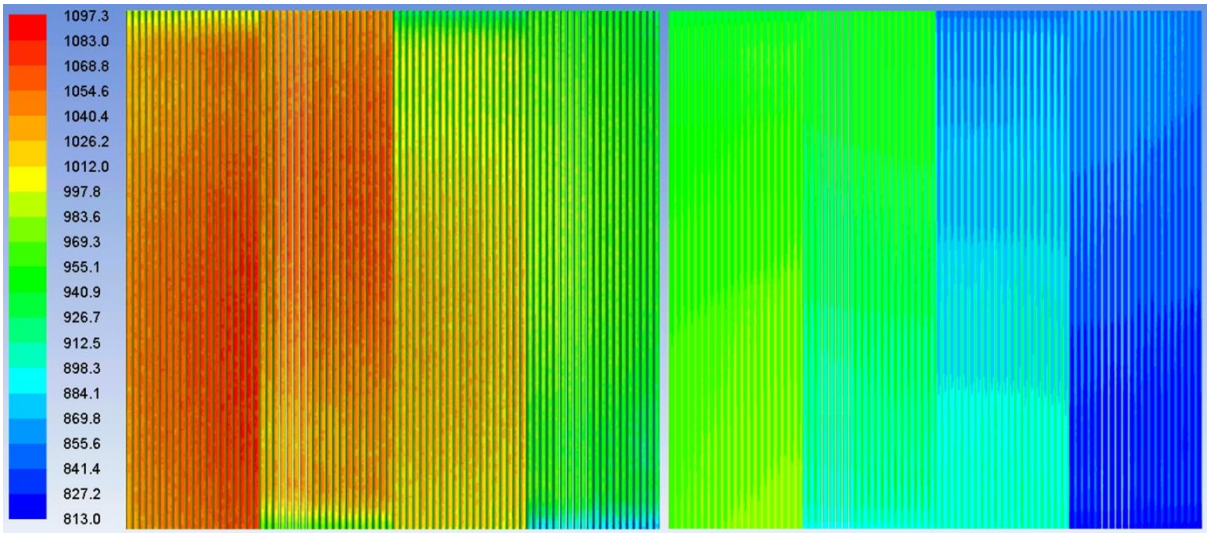

Fig. 5.29: Wall (left) and Center-Plane (right) Temperature Contours (in Kelvin) for Flow 4 with ~500 kW input and 4 aim-points

It is observed that the best thermal and overall receiver efficiencies are obtained for the cases which yielded the highest pressure drop across the receiver panels. This pressure drop is about 5% of the absolute pressure for the cases in which the flow pattern had many recirculation flow passes (Flow 4-6). A maximum pressure drop of about 1 MPa, which is estimated at the highest outlet temperature, yields a ~5% reduction in density, while the reductions in heat capacity, viscosity and thermal conductivity are ~0.5%. Even though the change in density is significant due to the pressure change, the effect on heat transfer coefficient inside the tubes is nearly negligible (about 0.1 %) for a given flow rate.

The highest thermal efficiency corresponds to the cases with flow patterns that have the most recirculation. This is due to the higher heat transfer coefficient that the flow exhibits inside the tubes when the mass flow rate is greater and the Reynolds number is higher. It is also shown that the maximum outer wall temperature is ~ 1100 K for the cases with high power input. These high temperatures are within the operating limits of the material under consideration.

Although there is a visible difference in the enhancement of the thermal performance of the s-CO_2 receiver which has a higher power input, the distribution of the aim-points on the receiver did not show any sign of improvement towards the thermal efficiency. The main limitation identified is the size of the receiver which makes the distribution of a single aim-point sufficient to encompass the foot print of the receiver. Nonetheless, for a larger-scale receiver, the aiming strategy might be crucial.

6. TESTING AND EXPERIMENTAL VALIDATION OF TUBULAR RECEIVER USING AIR AS HEAT TRANSFER FLUID

6.1. INTRODUCTION

Based on the analysis presented in chapter 5, a receiver consisting of panels constituted by circular tubes is a viable option for use in a solar tower for direct heating of supercritical carbon dioxide (s-CO_2). Such a receiver is found to heat s-CO_2 subjected to power inputs up to a few MW's and would safely deliver the fluid at temperatures up to 1000 K at pressures up to 20 MPa. The pressure drop for such a receiver is estimated to be within allowable limits. It is also inferred from the analysis in chapter 5 that staggering of tubes in order to enhance the absorptivity and reduce the reflective and emissive losses does not have a positive effect on the efficiency of the panels/receiver. It is found that recirculation of the working fluid through an appropriate arrangement of panels can result in significant enhancement of the receiver efficiency.

In this chapter, an appropriate arrangement of the panels designed in chapter 5 is discussed. The final arrangement is then modelled using the coupled methodology outlined in chapter 5 using air as the working fluid. The receiver is manufactured and tested on-sun with air as the heat transfer fluid. Compressed air is chosen as the working fluid for on-sun testing, as there is no existing solarized s-CO_2 test loop. The main goals of the on-sun tests are to validate the computational (optical and CFD) models by subjecting the receiver to high heat flux during on-sun tests and confirm the structural integrity of the receiver panels at high temperatures. Following sections will provide details of the final design and modelling of the receiver with air as the heat transfer fluid. Manufacturing details of the panels along with the on-sun test procedure, instrumentation and testing procedure details will be discussed followed by results.

6.2. BLADED RECEIVER CONFIGURATION

Typical tubular receivers consist of flat panels, composed of multiple tubes arranged in some formation, such as the Solar One and Solar Two receivers mentioned in the literature review. A novel approach to enhance the receiver efficiency is to control the receiver geometries to enhance the thermal efficiency by increasing the absorptance by the receiver and reducing radiative losses from the receiver. Garbrecht et al. [79] proposed a pyramidal structure of the receiver to enhance the optical behaviour, but reported hot spots at the peaks of the pyramidal structures due to low flow conditions. Rocketdyne [80] evaluated star shaped receiver geometry concepts, but the manufacturing difficulties render this configuration impractical.

In a typical receiver design where panels are arranged next to each other, the reflected and emitted radiation is lost to the surrounding due to a view factor equal to unity. If the receiver panels are arranged to render smaller external view factors, the reflected and emitted radiation can be re-captured by the panels that see one-another.

In a very recent work, Sandia National Laboratories (SNL) innovated [81] a series of light-trapping receiver designs which render lower external view factors aimed at increasing the efficiency of external tubular receivers. Christian et. al. [82-83] from SNL has performed detailed optical analysis and optimization of the invented geometric configurations and found that a bladed receiver configuration (figure 6.1), which consists of a louvered finned structure where certain panels are arranged horizontally at an angle to the vertical plane, like in the case of a razor blade is the most efficient design to enhance the optical behaviour of the receiver.

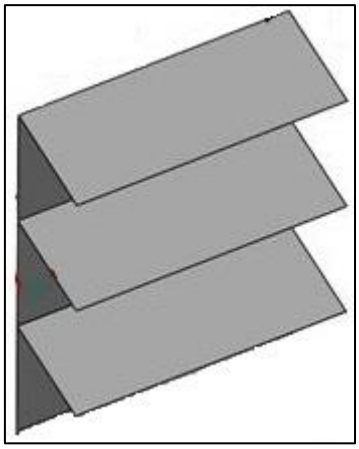

Fig. 6.1: Bladed receiver configuration [82]

The optical optimization study by Sandia National Labs utilizing their National Solar Thermal Test Facility (NSTTF) heliostat field revealed that for an aperture of about 0.5 m × 0.5 m, three blades consisting of 18 tubes each should be arranged at an angle of 50 degrees to the vertical plane for optimum optical performance. This configuration is adapted in the current study for use with the panels designed for s-CO_2 in chapter 5. Christian et. al. [82-83] have found that the use of such an optically efficient arrangement of the panels can enhance the overall s-CO_2 receiver efficiency presented in chapter 5 (for flat receiver) by up to 5 %. Modeling, manufacturing and testing of the adopted design with air is presented with the aim of validating the computational modelling and demonstration of the tubular receiver design for high temperature application. It is anticipated that the receiver will deliver very low efficiency for on-sun test with air due to the mediocre heat transfer properties of air, in comparison to the actual fluid for which the receiver is designed, which is s-CO_2. Another reason why the receiver efficiency is expected to be low is that the testing is at a low power input, whereas losses are high due to the high temperature test strategy which is adopted and explained below.

Before discussing details of the modelling, manufacturing and testing, some of the key points related to the overall procedure will now be outlined. These points justify the choice and procedure of modelling and illustrate the synergy between the experiment and modeling technique. For a demonstration of the receiver performance, it is tested at the NSTTF, SNL using compressed air bottles with concentrated solar input of varying power levels. The use of compressed air bottles restricts the test time with fluid flow to about 15 minutes, but provides a an inexpensive way of testing with the flexibility of performing multiple repeatable tests by simply replacing the bottles. In order to attain a high fluid outlet temperature, the receiver is first preheated slowly at a low power input without flow for about an hour, followed by a relatively high power input to the receiver with flow of air.

6.3. RECEIVER GEOMETRY AND FLOW CONFIGURATION

The receiver design concept which is modelled and tested is shown in figure 6.2. It consists of 3 vertical panels (13 tubes per panel) at the back with 3 blades aligned at an angle of 50 degrees to the vertical. Each blade consists of two panels. There are 9 tubes in each blade panel, i.e. total 18 tubes per blade. Each tube has an outer diameter of 12.7 mm and a

thickness of 1.65 mm. Comments on structural integrity of the s-CO_2 receiver tube and header will be briefly discussed in section 6.6. While detailed structural analysis of the current design considering combined effect of static stresses, thermal stresses, creep and fatigue response of the tubes has been done by structural mechanics experts [84], these aspects will not be discussed in detail in this thesis. Flow path for the working fluid and the receiver dimensions are shown in figure 6.3. It can be clearly seen that there are three similar flow paths to cool the receiver; each flow path starts with entry of fluid from the left side of the front bladed header, followed by recirculation in the bladed panel towards the back and the fluid finally entering the back panel through bottom and exiting at the top.

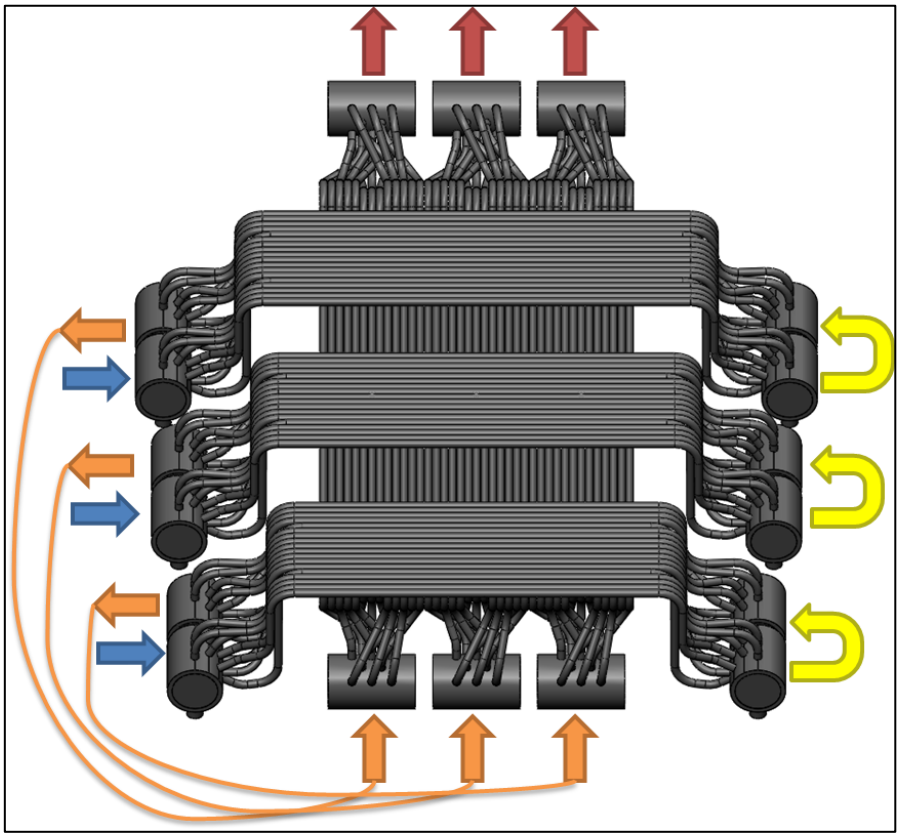

Fig. 6.2: Bladed receiver design concept and flow pattern

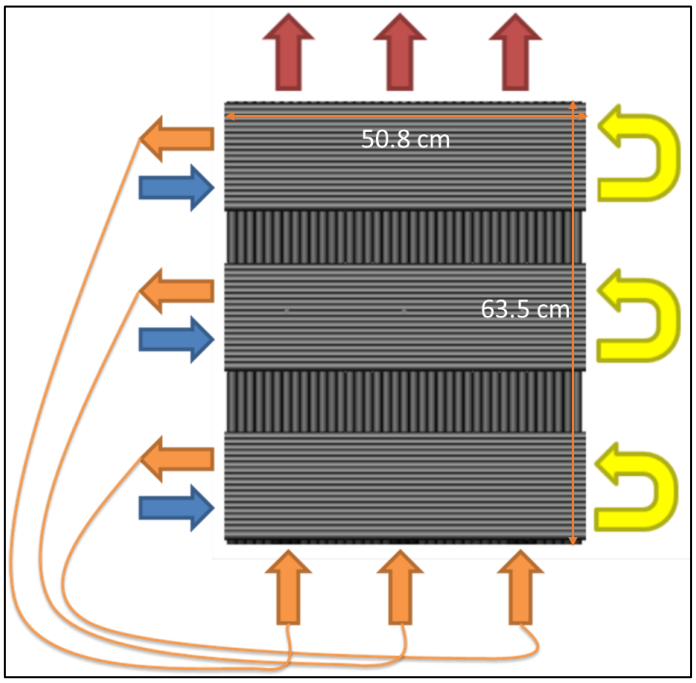

Fig. 6.3: Receiver geometry and model for optical-thermal-fluid analysis

As evident from figure 6.3, the headers for any of the panels are not modeled in the detailed CFD models, but the flow distribution, pressure drop, and heat transfer coefficient through the header is modelled separately to ensure that the flow distribution amongst the tubes is uniform. The findings for the same will be discussed in the results section. Another important implication of the presence of headers in the real on-sun experiment is the addition of thermal mass not exposed to the irradiation from the heliostat field. A modified efficiency to account for the transient heating and energy transfer from fluid to headers is proposed and will be discussed in detail in the results section.

6.4. OPTICAL MODELING

To obtain the heat flux for the thermal-fluid modeling, SolTrace, a ray-tracing based optical modeling software developed by NREL is used, as mentioned in chapter 5. The heliostat field at NSTTF is modeled in SolTrace and the receiver geometry created in SOLIDWORKS is imported in SolTrace. The typical ray intersections in SolTrace are shown in figure 6.4.

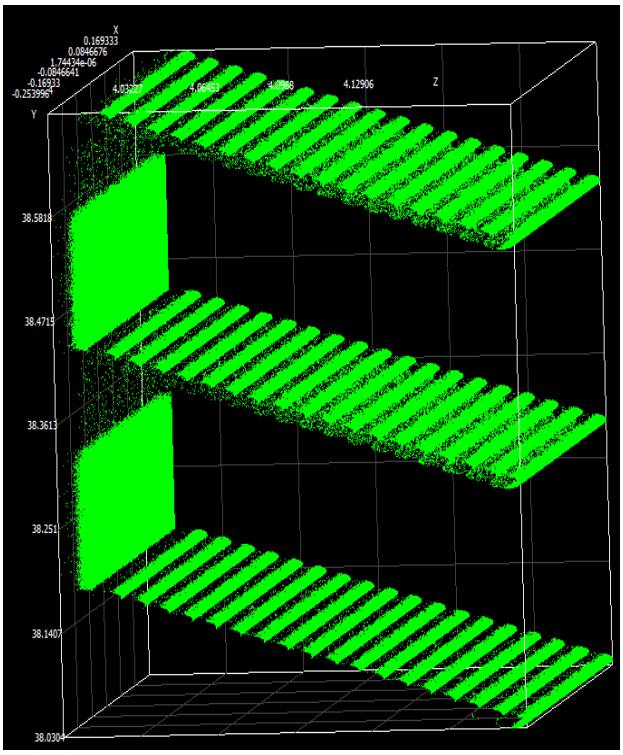

Fig. 6.4: Typical ray intersections for bladed receiver from SolTrace

The results obtained in SolTrace are coupled with ANSYS Fluent using a MATLAB code that generates a file which can be used as a boundary condition in ANSYS Fluent as described in chapter 5. The preheating heat flux profiles are generated using 8-10 heliostats, while the heat flux profiles for on-sun test with flow are obtained using 10-16 heliostats from the SolTrace model of the NSTTF for three peak flux levels of 90, 120 and 150 kW/m^2. These flux levels correspond to a total power input of 23, 32, and 43 kW, respectively.

6.5. COMPUTATIONAL FLUID DYNAMICS (CFD) MODELING

ANSYS Fluent is used for detailed investigation of the thermal fluid performance of the receiver using air as the heat transfer fluid. The CFD modeling is performed for two transient periods, preheating without flow and heating with air flow (with a relatively higher heat flux compared to preheating). After the preheating of receiver is simulated, the full power heat flux profile is imposed on the receiver and air flow with receiver heating is simulated for 900 seconds, which is close to the actual on-sun heating with flow test time. Three different power levels are simulated, as in the on-sun tests, corresponding to peak fluxes of 90, 120

and 150 kW/m^2. The power imposed on the receiver surface during the 900 seconds of flow time is approximately 23 kW, 32 kW and 43 kW for the three cases, respectively. Figure 6.5 shows some of the important thermal boundary conditions imposed on the receiver.

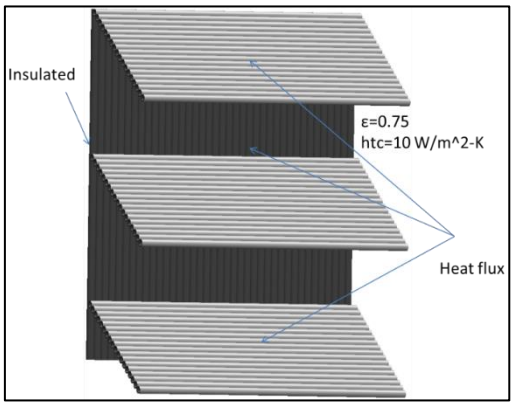

Fig. 6.5: Thermal boundary conditions

The back side of the receiver is modelled as adiabatic, and the convective and radiative heat losses from the other surfaces are modelled using an emissivity of 0.75 and a convection heat transfer coefficient of 10 W/m^2-K. Recirculation boundary condition is used to connect the flow paths in the model without modeling the headers which exist in the actual receiver. Effect of gravity is considered along the axial direction of the vertical tubes. Mass flow rate of air through each flow path is ~15 g/s and the pressure at receiver inlet is slightly above atmospheric pressure (~250 kPa). Temperature varying thermo-physical properties of air (thermal conductivity, specific heat and density) are considered. The tube is modeled using Inconel 625 material properties and the tube thickness is modeled to evaluate the effect of conduction through the tubes. The heat flux profile is imposed as a boundary condition. Surface-to-Surface (S2S) radiation model is implemented in ANSYS Fluent to model the radiation heat exchange between tube surfaces, which can be significant due to the spatially varying temperature distribution. Turbulent flow inside the receiver tubes is modeled using the SST k-omega turbulence model with standard model constants. The SIMPLE scheme is used for the pressure-velocity coupling and second-order upwind method is used for momentum and energy equation along with first order implicit transient formulation. Standard relaxation factors from ANSYS Fluent are used and convergence for each time step is ascertained by monitoring the residuals until they drop and remain constant. Fifteen

monitors are setup to observe the temperatures at 3 inlets, 3 outlets, 6 recirculation and 3 points on the receiver back surface at 20 cm from the top-most point of the model. In the experiment, thermocouples have been placed at exactly same locations in the on-sun test.

6.6. PANEL DESIGN AND FABRICATION

The structural design of bladed receiver is performed by following the requirements for a pressure vessel in the American Society of Mechanical Engineer Boiler and Pressure Vessel Code (ASME BPVC) Section VIII. Inconel 625 is selected for the final analysis and fabrication of the receiver, as the allowable stresses for the desired operating temperature are comparable to that of Haynes 230, but the easy availability of Inconel 625 makes it suitable for solar receiver application.

The required minimum wall thickness and corresponding maximum allowable working pressure is determined using the UG-27 and UG-34 equation of ASME BPVC Section VIII [85]. Based on the sizes available in stock commercially, 3" schedule 80 pipe with ¾" end caps is used for the headers, ¾" schedule 40 tube is used for the inlet/outlet tubes connecting the panels, and 1/2" tubes are used for the receiver tubes. The minimum thickness requirements from calculations indicate that the header size used to manufacture the receiver can safely sustain pressure up to 15.2 MPa, while rest of the components can sustain pressures above 20 MPa. Hence, the header is the weakest component of the receiver. The unavailability of 3" schedule 160 pipes resulted in acceptance of this limitation and use of 3" schedule 80 pipe with upper limit of 15.2 MPa at the target operating temperature.

For welding the tubes to the header, the weld design requirements for the area of reinforcement can be found in UG-37 while the weld strength analysis is available in UG-41 of Section VIII. The header pipes are cut into two longitudinal halves and holes are drilled on the curved surface to insert the receiver tubes and perform the tube welds internally. This procedure does not affect the integrity of the headers as long as the seam weld to join the halves back is fully penetrating as per UW-12 requirements of the ASME BPVC Section VIII.

As the receiver is a pressure vessel and the material (Inconel 625) has special machining requirements, the bending and cutting is done by certified machine shops, Springs Fabrication and Albina Inc, USA.

Fig. 6.6: Headers cut by Springs Fabrication

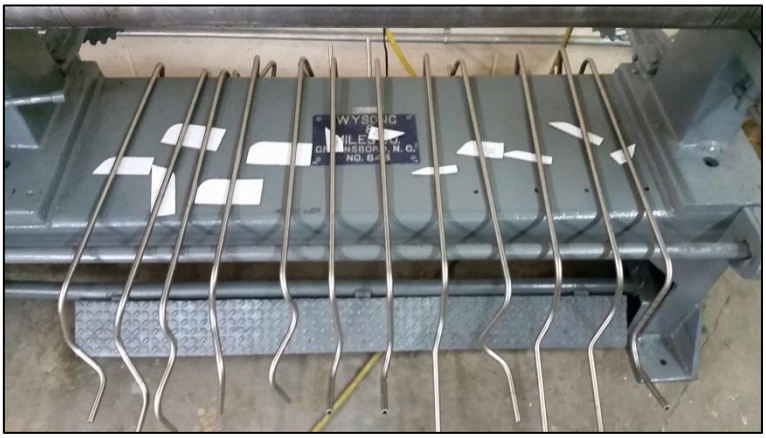

Fig. 6.7: Tubes needed for the back panels, bent by Albina, Inc

Figure 6.8 shows a typical header with tube inserts along with the header cap in place before welding, while figure 6.9 shows the assembled and tacked panels just before welding. As discussed earlier, the back panels have 13 tubes each panel, while each blade consists of two panels of 9 tubes each panel.

Fig. 6.8: Header with inserted tubes and header caps in place before welding

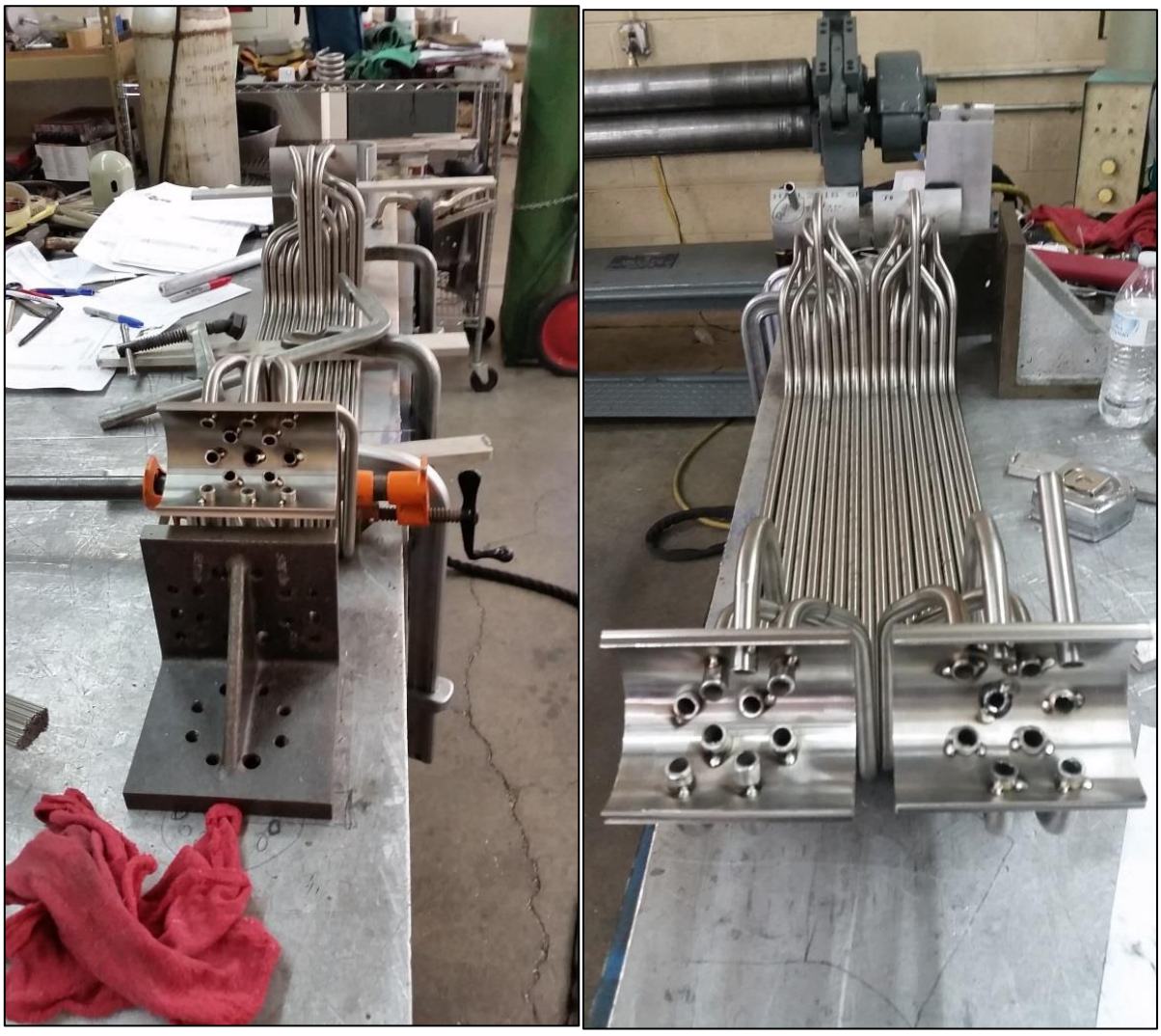

Fig. 6.9: Back panels (13 tubes) and fin panels (9 tubes/panel) assembled and tacked

The welding is done by certified high precision welding shop, Saavedra Precision Welding, Albuquerque, USA and figures 6.10, 6.11, and 6.12 show the type of weld for receiver tubes, header caps and header halves respectively.

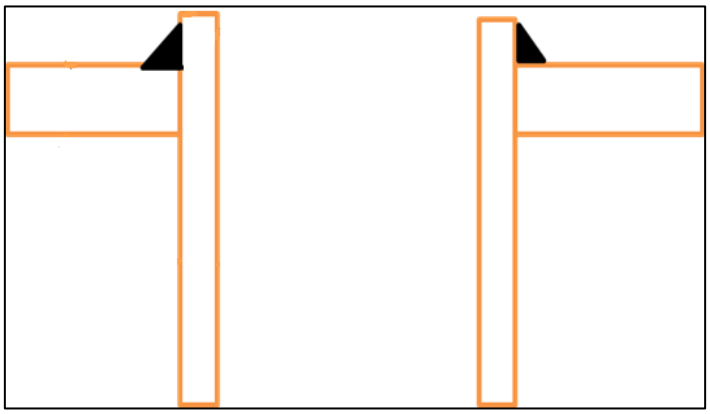

Fig. 6.10: Internal weld for receiver tube inserted in header

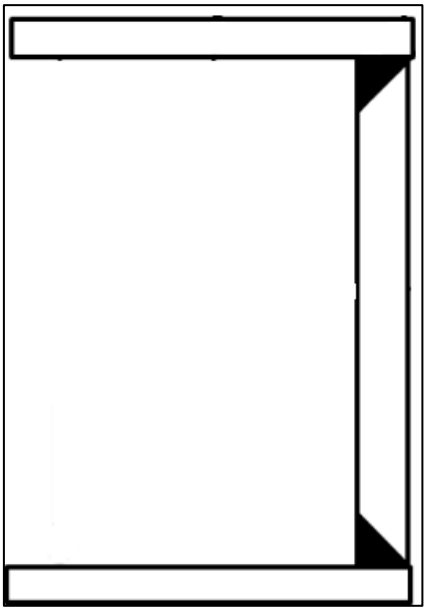

Fig. 6.11: Single-butt partial-penetration weld for header cap and header

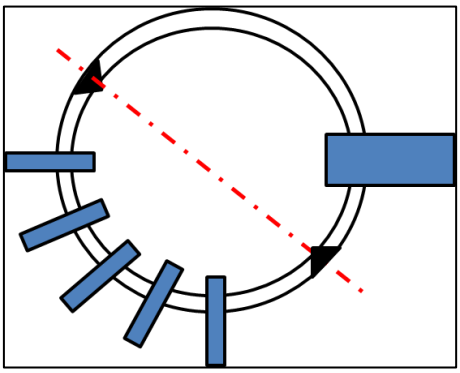

Fig. 6.12: J-groove full-penetration weld for the header halves

Figure 6.13 shows a typical assembled panel delivered by the welding shop after pressure testing and certification.

Fig. 6.13: Assembled panel

6.7. PANEL OXIDATION AND LEADING TUBE FAILURE PREVENTION

In order to obtain high absorptivity of the receiver, the Inconel panels are oxidized in an open furnace at 1073 K for 24 hours. This results in development of an oxide coating on the

receiver surface with intrinsic reflectivity of about 0.1. The reflectivity is measured on the flat surface of the header caps.

The optical analysis predicts that there is a very high chance that the front-most tube of the bladed panel will be subjected to very high local fluxes resulting in possible failure of the leading tube. In order to prevent damage to the receiver, the front-most tube of the three blades is coated white with very high temperature VHT flame proof paint.

6.8. BLADED RECEIVER ON-SUN TESTING

The experiments described in this chapter were conducted in the summer of 2017 at the NSTTF at Sandia National Laboratories, Albuquerque, US. The receiver is tested at the lowest test bay of the solar tower, which is at 120 feet (~36.5 m) above ground level (figure 6.14).

The incident flux on the receiver is measured using a "calibration panel". The calibration panel consists of aluminium rectangular tubing arranged in a serpentine manner, while water/glycol is flowing through the panel tubes. At the centre of the panel is a Kendall radiometer (figure 6.15) capable of accurate heat flux measurements. This gauge (which is also cooled by water/glycol) is used to calibrate images of the flux panel captured when it is irradiated. An image is captured and scaled according to the measurement of the radiometer as per standard flux measurement technique established at the NSTTF. The flux image is then used to determine the incident power on the target. The receiver is located to the right of the flux calibration panel. The incident power is measured using this technique just before and after the on-sun flow test of the receiver.

Fig. 6.14: NSTTF solar tower and heliostats during test

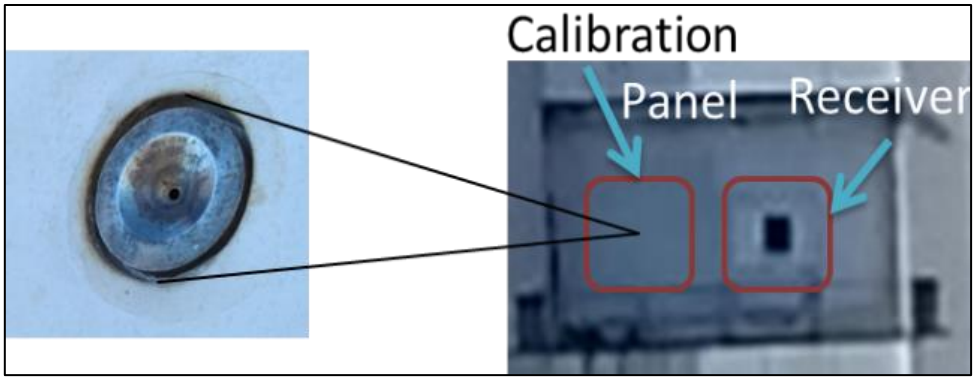

Fig. 6.15: Kendall radiometer and its relative position to receiver

Figure 6.16 shows a typical flux measurement where the receiver is still under the preheat beam, while 16 heliostats are focused on the flux panel, just before starting the flow test.

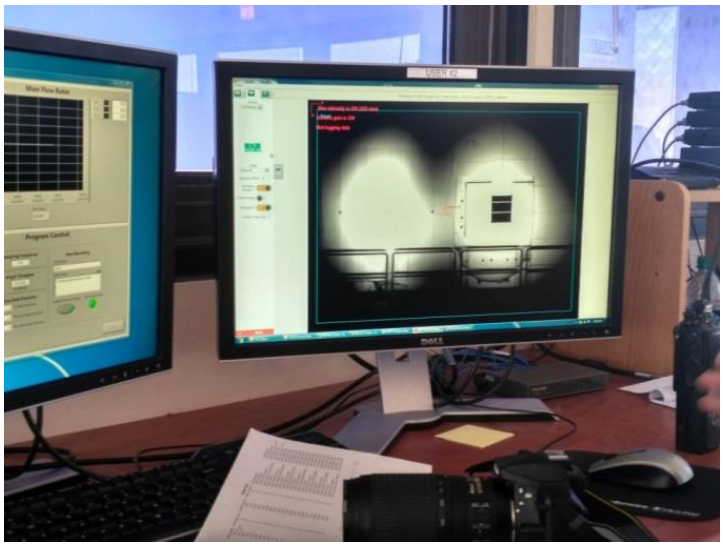

Fig. 6.16: Preheat flux on the receiver and 16 heliostats focused on the flux calibration panel

6.9. FLOW LOOP AND INSTRUMENTATION DETAILS

Three identical compressed gas loops are built to connect 18 bottles of air to three flow paths in the receiver (6 bottles per flow path). Each loop comprises of, in sequence, gas bottles, pigtails and cross connectors (to connect 6 pressurized compressed air bottles to a single line), pressure switch (to signal the heliostat field to de-focus in case the pressure [and consequently, mass flow rate] from air cylinders drop below a pre-set level), a pressure regulator and pressure gauge, a pressure relief valve, an on-off ball valve, a digital mass flow-temperature-pressure measurement meter (Alicat Scientific model number M-1500SLPM-D), and finally, the receiver. Three such loops operate in parallel, while the receiver is subjected to concentrated irradiation using the heliostat field at NSTTF. As mentioned in the 'Geometry' section, each flow path of the receiver consists of 2 bladed panels (9 tubes per panel) and 1 vertical panel of 13 tubes. The hot air at the exit of receiver is guided to the atmosphere through braided metal tubes. The air cylinders and air handling manifold system are shown in figures 6.17 and 6.18, respectively.

Fig. 6.17: Three stacks of air bottles (6 bottles per stack) located just behind the receiver

Fig. 6.18: Air handling manifold system

Twelve K-type thermocouples are inserted in the receiver through Swagelok T-joints to measure the flow temperature directly. Three thermocouples at inlets, three at outlets, six at recirculation points and three K-type thermocouples are spot-welded to the central tube on

the backside of each vertical panel, at a distance of 20 cm from the top, measured from the edge of the heated part. The three thermocouples at the back are used to monitor the temperature of the receiver panels during preheating with flow. These points are the same as the ones monitored in the CFD model.

After the receiver is mounted on a supporting movable frame, Dura Board HD is used to protect the instrumentation and other equipment from the spillage flux. Any part of the receiver which is not subjected to direct flux from the solar field is covered with high temperature insulation, while braided flexible metal hoses are used to safely carry the hot air at receiver exits for releasing into the atmosphere. The insulated receiver and supporting structure are shown in figures 6.19 (Front View) and 6.20 below (Back View).

Fig. 6.19: Front view of mounted receiver

Fig. 6.20: Back view of the mounted receiver

Weather instrumentation for measurement of wind speed and wind direction, measurement of direct normal irradiation (DNI) and lightning detector are some of the crucial instrumentation which are continuously monitored during the test, to ensure safe operation. This instrumentation mounted on the control room is shown in figure 21 below.

Fig. 6.21: Weather instrumentation mounted on the control room

6.10. TEST PROTOCOL FOR AIR RECEIVER TESTING

The following test protocol is followed for performing the test:

1. Initiate heliostat field start-up
2. Inspect test rig and ensure all connections are secure and apparatus is secured in rig
    a) Connect/Power UPS to power DAQ
    b) Plug Ethernet cable
    c) Power mass flow meters
    d) Ensure all connections are proper
3. Start-up cooling pumps and water cooling for Kendall and flux target and start tower NIP
4. Pressurize the three loops
    a) Ensure on-off ball valve is closed
    b) Ensure all bottles are connected and fully open
    c) Pressurize the system (~100 psi)
    d) Check the mass flow meters and tare (zero out)
5. Secure test bay and turn test in progress lights on
6. Make site announcement
7. Start collecting data and ensure values appear correct
8. Start recording data
9. Move heliostat beams to receiver
    a) Move heliostats to preheat the receiver (800 K)
    b) Once temperature is achieved, bring selected heliostats to the calibration panel
    c) Bring selected heliostats to close stand-by
    d) Start flow by opening valves
    e) Move the heliostats from calibration panel to the receiver
10. Operate for about 15 minutes, while the mass flow rate is constant at 15 g/s per loop
11. Bring selected heliostats to close stand-by
12. Shut-off valves
13. Move beams back to calibration panel to get post-test irradiance
14. Stop recording and save data
15. Shut down heliostat field
16. Vent test loops to depressurize system
17. Power down DAQ and mass flow meters
18. Make site announcement and turn test in progress lights off

19. Disconnect all cylinders and store them south of the tower and prepare for the next test with new cylinders

6.11. MODELLING AND TESTING RESULTS

Normally, the transient efficiency of the receiver can be calculated at every time step by accounting for the heat absorbed by the gas using equation 6.1.

$$\varphi^k = \frac{\sum_{i=1}^{3} \dot{m}_i^k \int_{T_{in}^k}^{T_{out}^k} C_{p_f}(T)dT}{\dot{Q}_{incident}^k} \quad \text{(…Eqn. 6.1)}$$

where $\dot{m}_i^k$ is the mass flow rate per flow path, $T^k$is the temperature, Cp_f is the heat capacity of the fluid, and $\dot{Q}_{incident}^k$ is the incident power on the receiver at time step k.

However, the insulated sections of the receiver that are not heated, as shown in figure 6.22, absorb part of the heat absorbed by the working fluid during the actual flow test. These sections are heated by conduction and by convection during flow test. However, conduction heat transfer is not occurring fast enough to heat up these regions. Therefore, most of the heating occurs by convection.

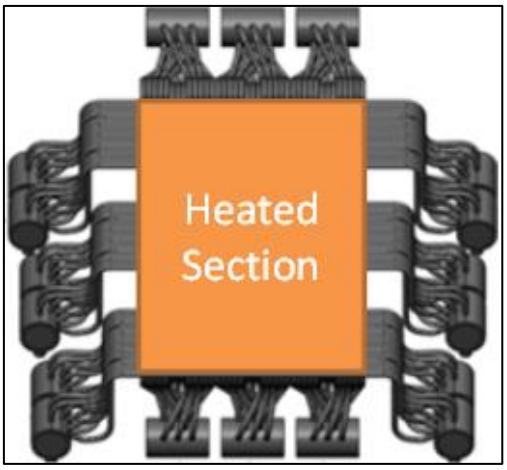

Fig. 6.22: Irradiated (Heated Section)

6.11.1. Adjusted Transient Receiver Efficiency

To account for the heat transferred to the non-irradiated regions, an adjusted efficiency calculation at every time step is suggested in this thesis. The adjusted efficiency considers the isothermal temperature increase of these regions as part of the energy that is absorbed by the fluid, in order to account for the heat transferred from the fluid to receiver at every time step using equations 6.2-6.4.

$$T_j^k = T_j^{k-1} + \frac{hA_s(T_f^k - T_j^{k-1})(t^k - t^{k-1})}{m_{h,j}Cp_h} \quad (\ldots\text{Eqn. 6.2})$$

Where T_j^k is the isothermal non-heated section temperature, T_f^k is the bulk fluid temperature entering the section, Cp_h is the heat capacity of Inconel 625, $m_{h,j}$ is the mass of the non-heated section, h is the HTC at temperature, A_s is the surface area of the non-heated section, and t^k is the flow time at every time step k.

Using equation 6.3, the total heat absorbed by the fluid is computed. Equation 6.4 is used to calculate the modified efficiency of the receiver at every time step.

$$\dot{Q}_{total}^k = \sum_{i=1}^{3} \dot{m}_i^k \int_{T_{in}^k}^{T_{out}^k} C_{p_f}(T)dT + \sum_{j=1}^{6} \frac{m_{h,j}C_{p_h}(T_j^k - T_j^{k-1})}{t^k - t^{k-1}} \quad (\ldots\text{Eqn. 6.3})$$

$$\varphi^k = \frac{\dot{Q}_{total}^k}{\dot{Q}_{incident}^k} \quad (\ldots\text{Eqn. 6.4})$$

where $\dot{m}_i^k$ is the mass flow rate per flow path, T^k is the temperature, Cp_f is the heat capacity of the fluid, and $Q_{incident}^k$ is the incident power on the receiver at every time step k.

6.11.2. Header Modelling

To account for the heat lost to the insulated sections shown in figure 6.23, the heat transfer coefficient (HTC) is modeled as a function of temperature for a mass flow rate of ~15 g/s. The average HTC over the entire zone is modeled across a range of temperatures and two flow directions for the two header types as shown in figure 6.24.

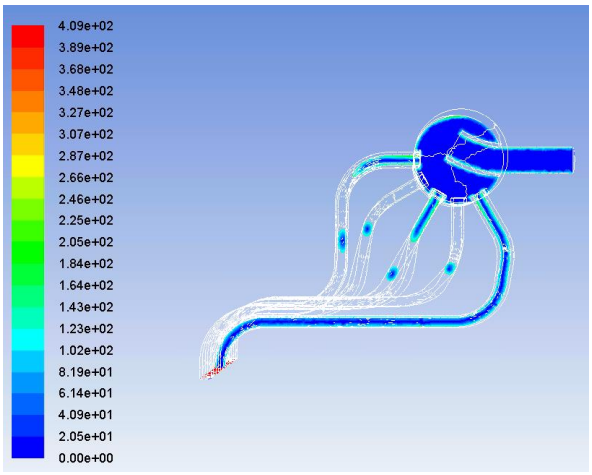

Fig. 6.23: Heat transfer coefficient contours on a centre plane across a back header with an air inlet flow rate of 15 g/s at 293 K and 250 kPa

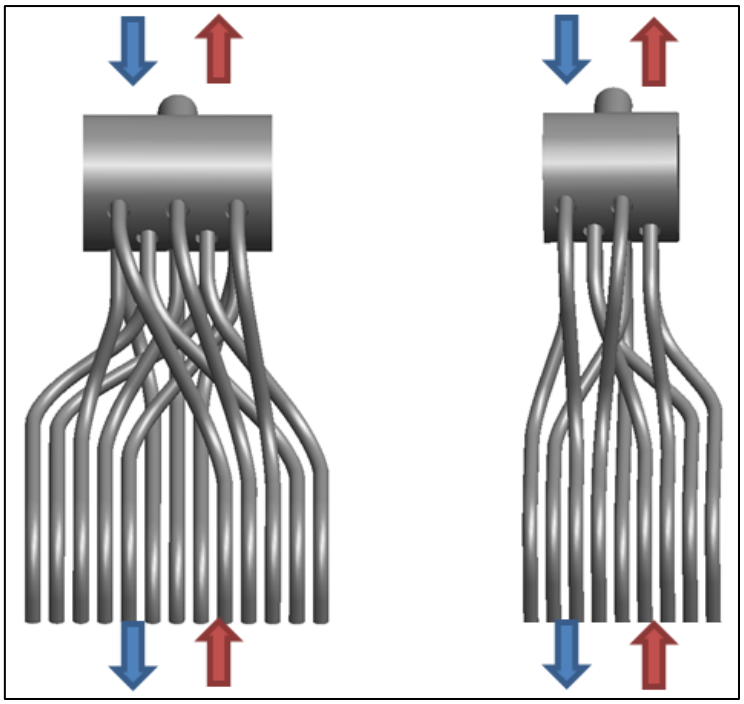

Fig. 6.24: Headers and tube sections insulated in the back panels (left) and fin panels (right)

The blue arrows correspond to the downstream flow (inlet) and the red arrows correspond to the upstream flow (outlet) across the headers.

The heat transfer coefficients (HTC's) shown in figure 6.25 are used to account for the temperature change in equation 6.2, which is then used to compute the modified receiver efficiency. These HTC's are computed as a function of temperature and type of header.

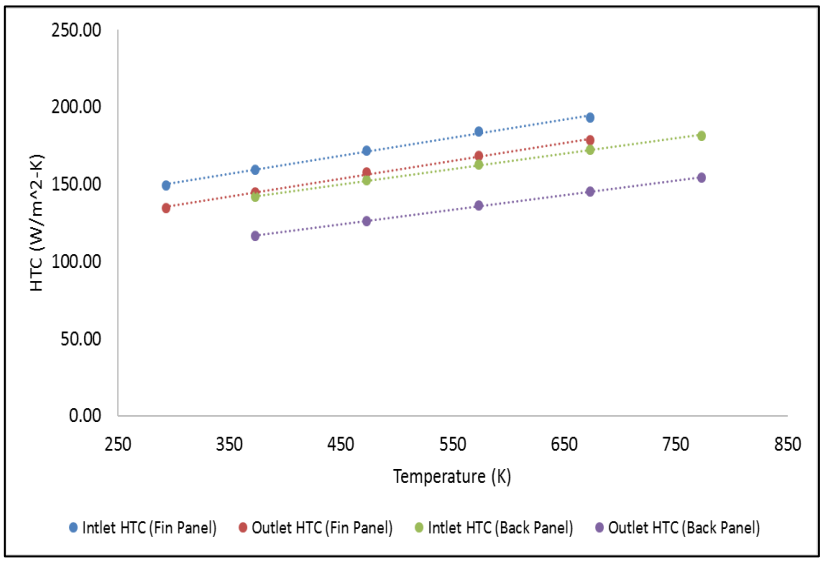

Fig. 6.25: Average heat transfer coefficient (HTC) as a function of temperature on the insulated sections of the back and fin panels

6.11.3. Temperature and mass flow measurements

To achieve a higher operating temperature of the receiver, even with the low power levels and small test times due to the limitation on amount of heat transfer fluid in the bottles, the receiver is preheated slowly using few heliostats (for a duration of about an hour). Figure 6.26 shows a typical preheating temperature variation as measured by the thermocouple at the back of the panels. The flux and variation of temperature is found to be similar for the three panels.

Figure 6.27 shows the temperature variation throughout the test, from preheating to post-test cool-down.

It can be observed that all the three loops undergo nearly same variation in temperatures.

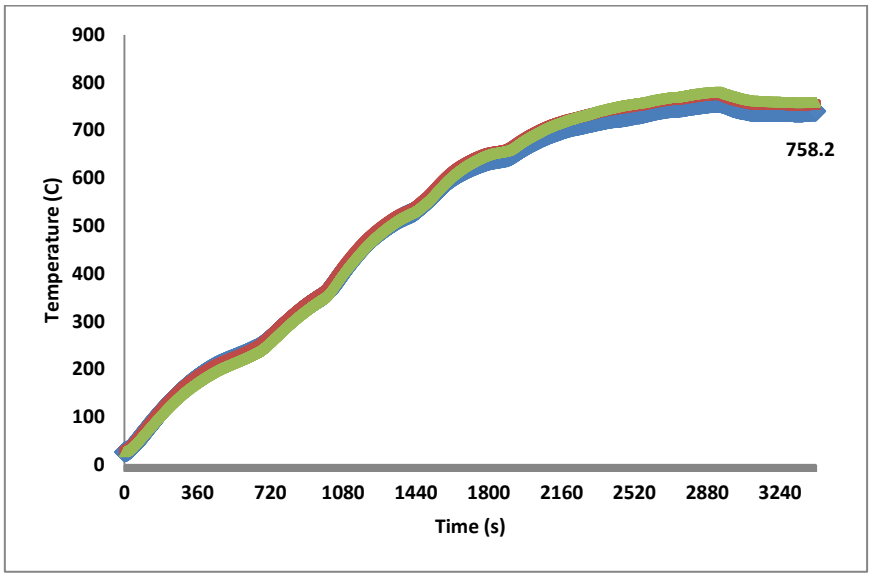

Fig. 6.26: Temperature variation during preheat measured by thermocouple at back of the panels

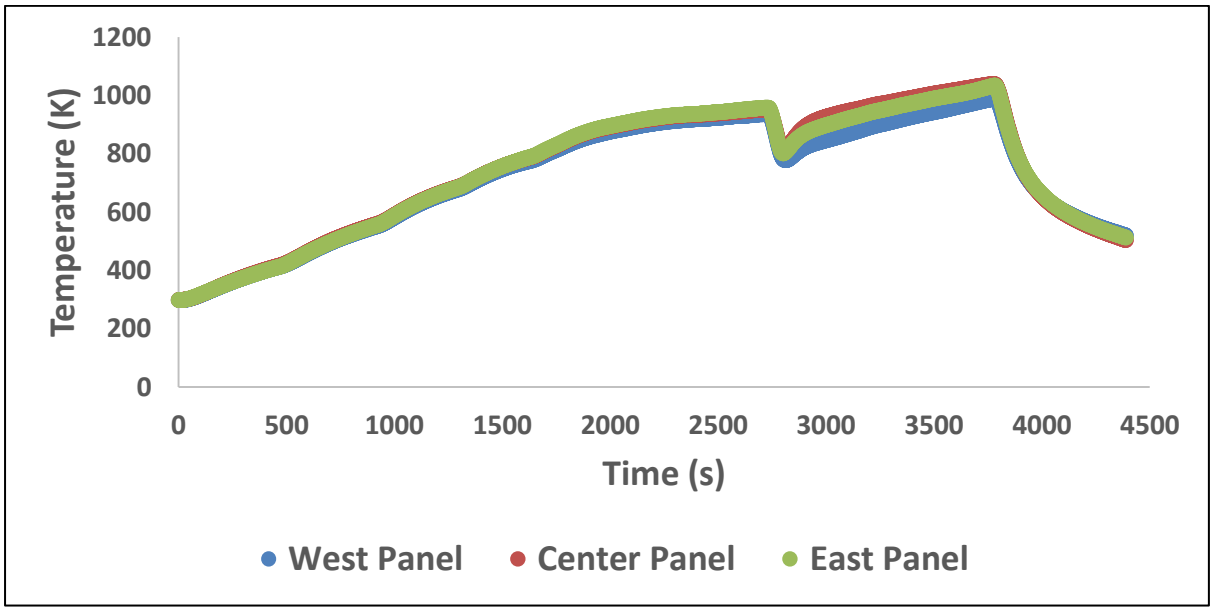

Fig. 6.27: Temperature variation for the full test (preheat, flow test, cool down) as measured by the thermocouples at the back

As mentioned earlier, similar to the thermocouples in experimental setup, 15 temperature monitors are setup in the CFD model to monitor the 3 inlets, 3 outlets, 6 recirculation points and 3 points on the receiver surface which had the thermocouples in the actual receiver test. Figure 6.28 shows the temperature contour of bladed receiver for the 150 suns case at the end of 900 seconds of flow time.

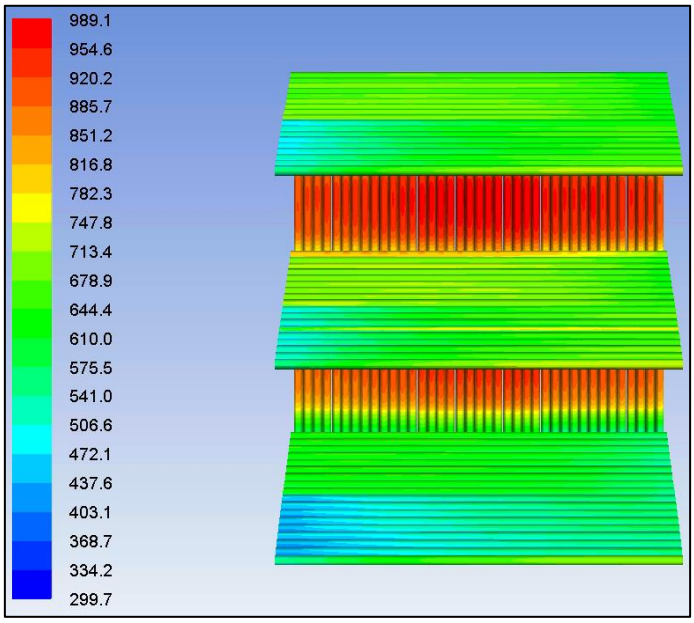

Fig. 6.28: Temperature contours (in K) of bladed receiver for 150 kW/m^2 case after 900 seconds of flow time

Mass flow measurement using the Alicat digital meter and the temperatures measured by various thermocouples for the 150 suns case are shown in figures 6.29 and 6.30, respectively. A receiver outlet temperature of about 700 K is obtained while using air bottles available at an initial pressure of about 15 MPa, while the test time is about 12-15 minutes. It can be seen that the inlet temperature remains nearly constant throughout the test time, while the flow rate starts dropping towards the end, but is constant for more than 10 minutes. The temperature at the outlet increases over the test period, as the receiver body got hotter and the air heats, expands and accelerates resulting in augmentation of convection heat transfer.

The data is only considered when the mass flow is stable, which is for a test time of 10-15 minutes. The slight variability in the mass flow rate of the three loops can be attributed to the variability of initial air pressure of the gas bottles.

While the preheat time for computational model is very low in comparison to the actual preheat due to the absence of the large thermal mass, the temperature monitor at the rear side of the panel showed same variation as observed in the experiment during the flow test time, albeit in a shorter simulated duration.

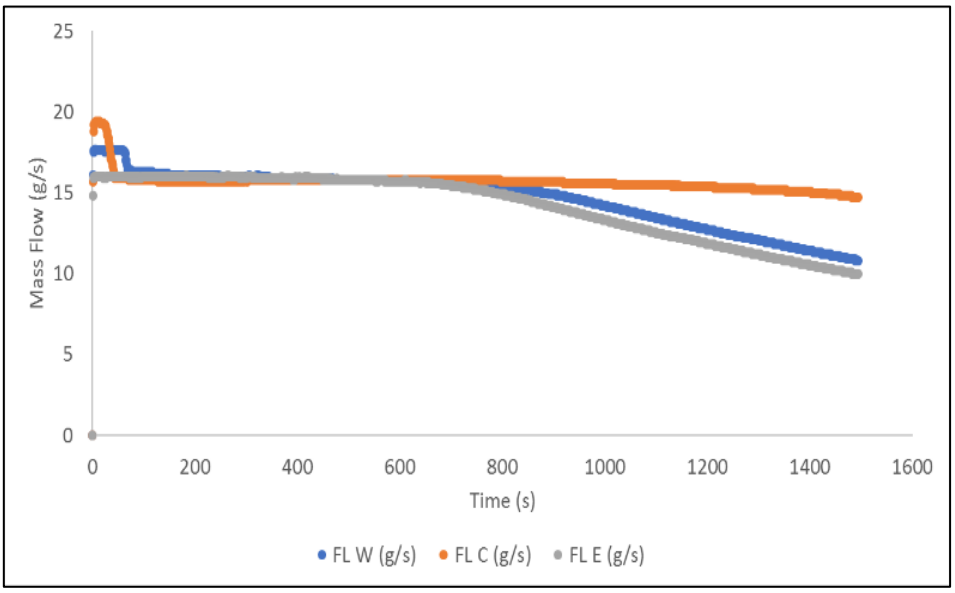

Fig. 6.29: Mass flow variation during the flow test for the 150 kW/m^2 peak flux case

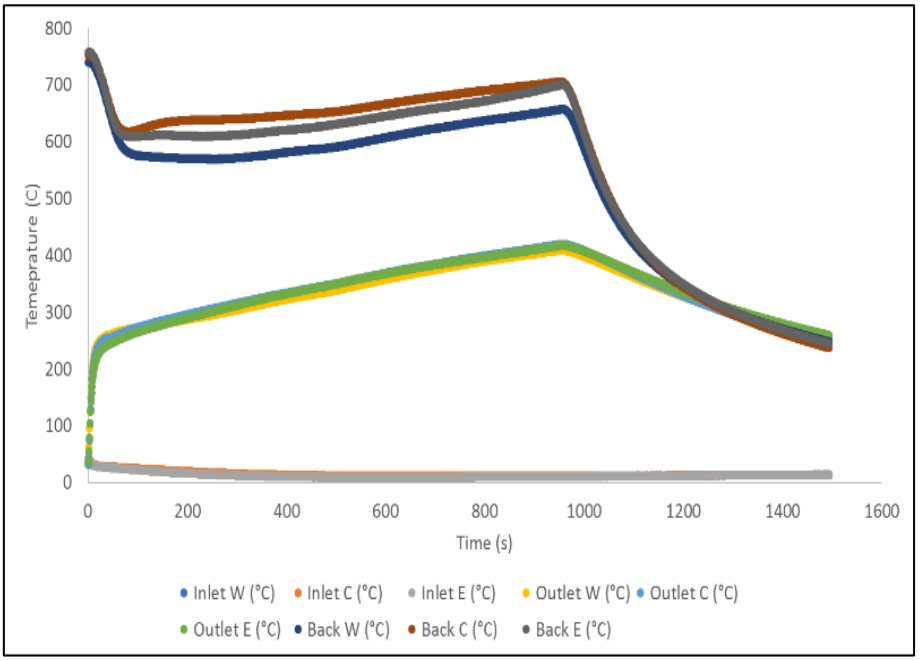

Fig. 6.30: Temperature variation during flow test for 150 kW/m^2 peak flux case

6.11.4. Receiver Efficiency

As mentioned earlier, the receiver is subjected to three different power levels, 23 kW, 32 kW and 43 kW during subsequent tests. An overall comparison of the experiment and simulations (figures 6.31 and 6.32) for the three cases reveals that the range of efficiencies is comparable for all three power levels for experiments and simulation.

The effect of increasing power on thermal efficiency shows similar behavior, too. The efficiencies shown in figure 6.32 are the modified receiver efficiencies, which are obtained as discussed in section 6.11.1. The modified efficiency is found to be higher by about 5 %, when compared to the efficiency obtained using standard efficiency formulation.

It is observed from figure 6.31 that the efficiency value for all the three cases in the simulation approaches steady state in a very short duration (~ 3 minutes). The steady state value of the efficiency along with the modified transient efficiency for the three cases is plotted in figure 6.32. The steady state efficiencies obtained from the simulations are plotted as a constant value in figure 6.32.

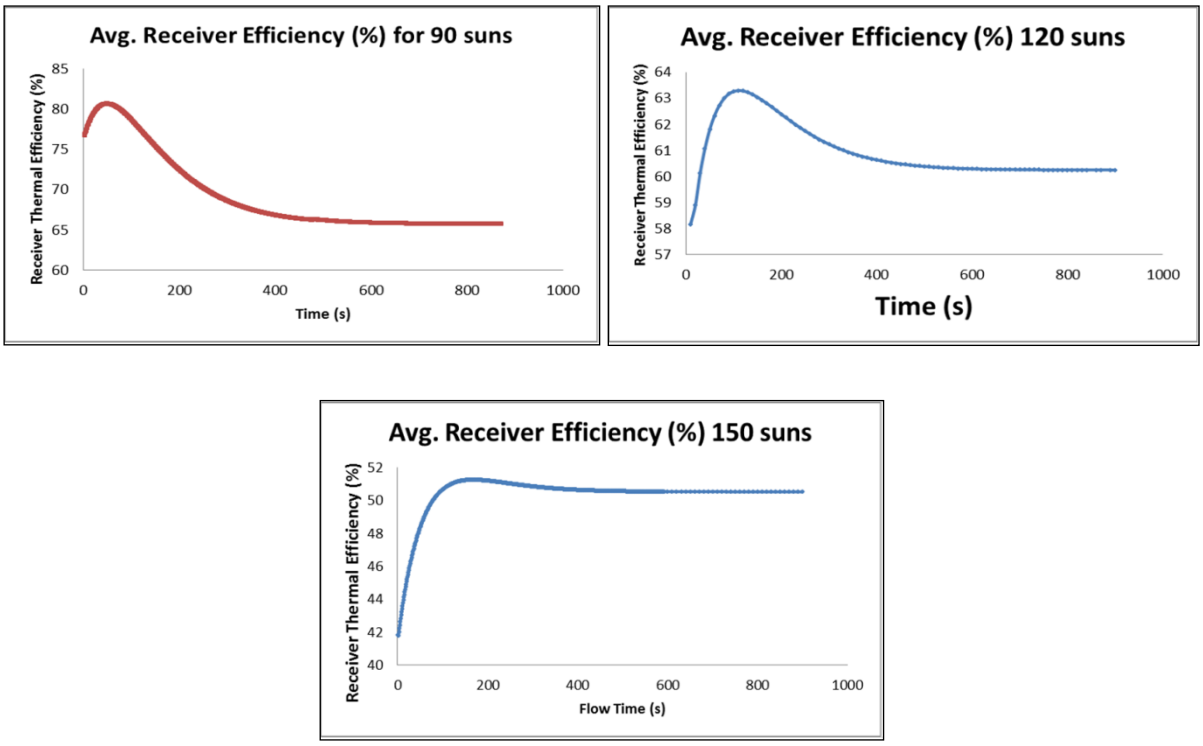

Fig. 6.31: Thermal efficiency for the CFD models of 90, 120, and 150 kW/m^2 peak fluxes

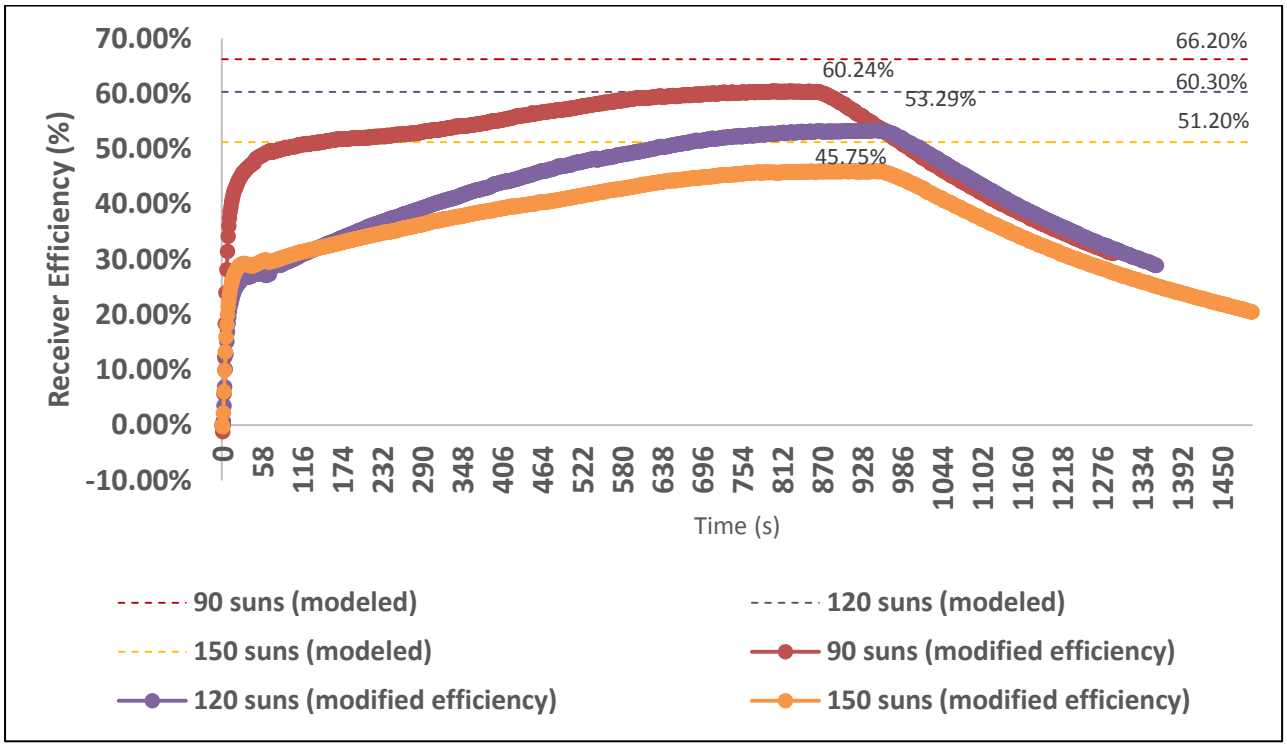

Fig. 6.32: Modified thermal efficiency for the on-sun test of 90, 120, and 150 kW/m^2 peak flux cases along with the steady state values from the simulations

It can be observed from figure 6.32 that while the on-sun tests exhibit a highly transient behaviour, the efficiencies are below the steady-state efficiency and the transient efficiency values seem to be converging on the steady state values predicted by the computational model, confirming the validity of the modelling.

The incident power on the receiver tube is split into three streams during the transient heating: power transferred to fluid, thermal losses to atmosphere, and transient heating of thermal mass of the irradiated tubes (figure 6.33).

As the process approaches steady state, rate of energy absorbed by the irradiated tubes (due to thermal mass) will decrease and ultimately reduce to zero at steady state, while the thermal losses will increase and attain a constant steady state value. If the energy absorbed by irradiated receiver tubes during transient heating is accounted for as a part of the transient receiver efficiency, the efficiency values will be estimated to be higher than those presented in figure 6.32. To illustrate this, consider the peak value of 150 suns (modified efficiency) show in figure 6.32, which is 45.75 % at about 950 s. The energy absorbed by tubes in the three back panels can be estimated based on the mass of the tubes, specific heat of Inconel 625 and the rate at which tube temperature changes, which is about 75 °C in 950 seconds (assuming linear variation with time), as measured by the thermocouple and plotted in figure

6.30. If this power absorbed by tubes is added to the power absorbed by the fluid, the resulting transient receiver efficiency curve will shift upward, resulting in an estimated peak transient receiver efficiency of about 59 %. At steady state, the tube temperatures will be higher. This would result in the efficiency value approaching the predicted value from simulations, which is 51.2 % and does not consider thermal mass effect.

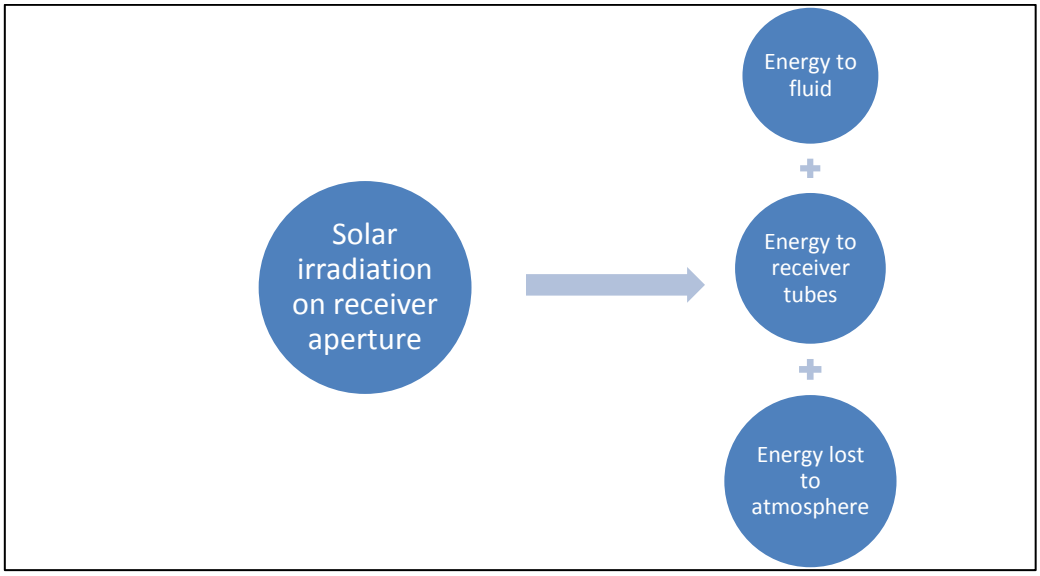

Fig. 6.33: Incident solar radiation on receiver aperture

6.11.5. Heat Flux

Figure 6.34 below shows a typical incident heat flux measured using the flux calibration panel adjacent to the receiver. The peak flux is about 160 suns (160 kW/m^2). The same heliostat configuration used during the above measurement is simulated using SolTrace and the corresponding heat flux map from SolTrace is shown in figure 6.35. The agreement between the simulated and measured heat flux is found to be satisfactory.

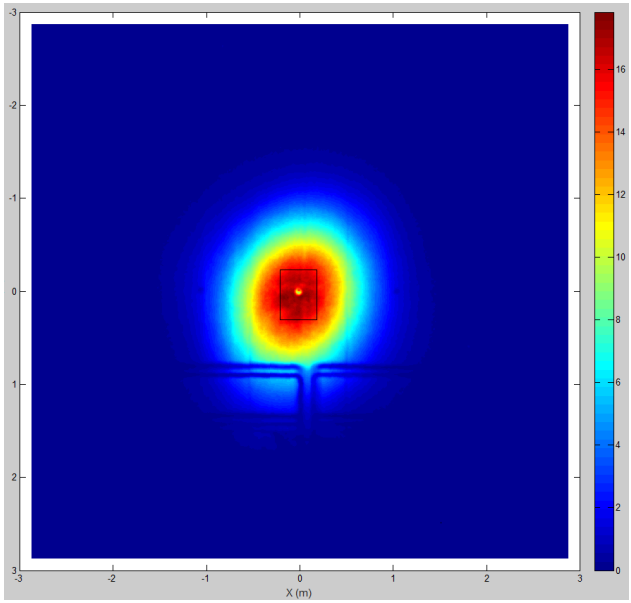

Fig. 6.34: Measured heat flux distribution with a peak flux of about 160 kW/m^2

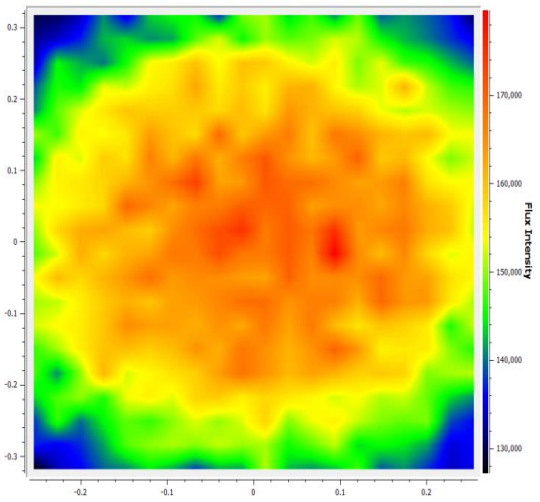

Fig. 6.35: SolTrace heat flux map for 160 kW/m^2 peak flux case

6.12. SUMMARY

The following points summarize the study in this chapter:

1. A bladed receiver which exhibits enhanced receiver efficiency (up to 5% higher compared to flat receiver) due to its unique light trapping geometry has been analysed in this work, both computationally and experimentally.

2. The details of the experimental procedure using three identical banks of compressed air bottles are explained and the computational model is developed to simulate the same process which happens in the on-sun tests (preheating followed by a short high temperature test with air flow).
3. Due to the limited test time, a novel methodology to calculate the efficiency by accounting for the transient nature and heat transfer to the header is presented.
4. The efficiencies from the experiment and numerical analysis are converging to the same value. The low values of receiver efficiency obtained in this chapter can be attributed to use of air instead of s-CO_2, and the low power input (compared to design power input which is ~0.5 MW) at high temperatures,
5. The bladed receiver configuration using the s-CO_2 receiver panels is successfully demonstrated to deliver air at an outlet temperature up to 500 °C and the computational model limitations and similarities to the experiment are established.
6. The low thermal efficiency for the tests can be attributed to the low heat fluxes and the transient nature of the tests which do not achieve steady state operation.

7. CONCLUSIONS

1. A review of the Concentrated Solar Power (CSP) technologies and current trends in the field of CSP suggest that solar powered supercritical carbon dioxide (s-CO_2) Brayton cycle with the central receiver system, i.e. power tower configuration is a viable option for achieving high power plant efficiency (~50 %) with the possibility of having distributed small scale systems suitable for addressing the energy needs in India.
2. For accurate design and estimation of heat transfer performance of equipment handling supercritical CO_2, the participating nature of s-CO_2 can be significant in the overall heat transfer calculations. Detailed spectroscopic measurements must be undertaken for obtaining reliable optical property (absorption coefficient spectrum, emissivity) data.
3. For heat transfer equipment using circular tubes, neglecting radiation absorption by s-CO_2 can result in deviation up to 250 K in the prediction of tube wall temperatures. Due to enhancement of the overall heat transfer coefficient by virtue of radiation heat transfer to s-CO_2, the resulting lower tube wall temperature implies lower heat loss, lower required heat transfer area and possibility of using lower temperature materials. In general, the radiative component in the overall heat transfer is more significant for lower values of Reynolds number and larger values of tube internal emissivity, radiative path length and tube temperature.
4. For measurement of total emissivity of s-CO_2, a new experimental technique using shock tube is presented in this work. It is found that s-CO_2 acts as a participating medium, and the percentage contribution of radiation towards the total heat exchange can be significant. For the conditions studied, the total emissivity value of supercritical conditions is nearly 0.2, implying that s-CO_2 acts as a participating medium for radiation heat transfer. This opens up a wide scope for making more accurate and detailed measurements of spectral radiative properties of s-CO_2 for different path lengths and at higher pressures and temperatures. Traditionally, such effects were not considered in the design of heat exchangers used in s-CO_2 based power cycles involving high temperatures. Hence, the results of the present work will have tremendous implication in such designs. The estimated total emissivity value

compares favourably with that predicted theoretically using a standard method available in literature.

5. For design of a supercritical carbon dioxide tubular receiver, a coupled optical-thermal-fluid modelling methodology is developed in this work. It is found that using the real heat flux distribution on the receiver surface is important and use of a uniform or approximate heat flux variation may result in underestimation of the peak tube temperatures.
6. The coupled methodology is used to design a s-CO_2 receiver using the real heat flux distribution obtained from optical modelling of the heliostat field at National Solar Thermal Test Facility (NSTTF) at Sandia National Laboratories (SNL), USA. Detailed modelling reveals that the designed receiver panels are capable of raising temperature of s-CO_2 by about 160-200 K, while operating within the permissible range of temperature from material integrity point of view, while maintaining an allowable pressure drop across the s-CO_2 receiver.
7. The computational modelling indicated that staggering of receiver tubes deteriorates its thermal performance, while recirculation within the receiver panels can enhance the receiver efficiency significantly. Operation at larger power inputs and higher peak fluxes generally results in an increase in the receiver efficiency, while the aim point strategy is found to be generally significant for large receiver apertures only.
8. As suggested in a recent innovation at SNL, arrangement of the receiver panels in the form of blades can result in an increase in the overall receiver efficiency by up to 5 % compared to the flat arrangement, due to better optics. This bladed receiver arrangement is adopted in the final stage of this work for modelling, testing and validation of the s-CO_2 receiver using air as the heat transfer fluid. Details of the receiver prototyping procedure, testing and coupled modelling of the bladed receiver is presented. The prototype is successfully demonstrated to safely heat air up to a temperature of 700 K, with receiver wall temperatures approaching 1000 K.

REFERENCES

1. Liao, Z., Li, X., Xu, C., Chang, C., & Wang, Z. (2014). Allowable flux density on a solar central receiver. *Renewable Energy*, *62*, 747-753.
2. Selvakumar, N., & Barshilia, H. C. (2012). Review of physical vapor deposited (PVD) spectrally selective coatings for mid-and high-temperature solar thermal applications. *Solar Energy Materials and Solar Cells*, *98*, 1-23.
3. Ho, C. K., Mahoney, A. R., Ambrosini, A., Bencomo, M., Hall, A., & Lambert, T. N. (2014). Characterization of Pyromark 2500 Paint for High-Temperature Solar Receivers. *Journal of Solar Energy Engineering*, *136*(1), 014502.
4. Behar, O., Khellaf, A., & Mohammedi, K. (2013). A review of studies on central receiver solar thermal power plants. *Renewable and sustainable energy reviews*, 23, 12-39.
5. Romero-Alvarez, M., & Zarza, E. (2007). Concentrating solar thermal power. *Handbook of energy efficiency and renewable energy*.
6. Danielli, A., Yatir, Y., & Mor, O. (2011). Improving the optical efficiency of a concentrated solar power field using a concatenated micro-tower configuration. *Solar Energy*, *85*(5), 931-937.
7. Gong, G., Huang, X., Wang, J., & Hao, M. (2010). An optimized model and test of the China's first high temperature parabolic trough solar receiver. *Solar Energy*, *84*(12), 2230-2245.
8. Xiong, Y., Wu, Y., Ma, C., Traore, M. K., & Zhang, Y. (2010). Numerical investigation of thermal performance of heat loss of parabolic trough receiver. *Science China Technological Sciences*, *53*(2), 444-452.
9. Avila-Marin, A. L. (2011). Volumetric receivers in solar thermal power plants with central receiver system technology: a review. *Solar Energy*, 85(5), 891-910.
10. Tan, T., & Chen, Y. (2010). Review of study on solid particle solar receivers. *Renewable and Sustainable Energy Reviews*, *14*(1), 265-276.
11. Tamme, R., Laing, D., & Steinmann, W. D. (2003, January). Advanced thermal energy storage technology for parabolic trough. In *ASME 2003 International Solar Energy Conference* (pp. 563-571). American Society of Mechanical Engineers.
12. Zanganeh, G., Pedretti, A., Zavattoni, S., Barbato, M., & Steinfeld, A. (2012). Packed-bed thermal storage for concentrated solar power–Pilot-scale demonstration and industrial-scale design. *Solar Energy*, *86*(10), 3084-3098.
13. Mahian, O., Kianifar, A., Kalogirou, S. A., Pop, I., & Wongwises, S. (2013). A review of the applications of nanofluids in solar energy. *International Journal of Heat and Mass Transfer*, *57*(2), 582-594.
14. Watanabe, T., Kikuchi, H., & Kanzawa, A. (1993). Enhancement of charging and discharging rates in a latent heat storage system by use of PCM with different melting temperatures. *Heat Recovery Systems and CHP*, *13*(1), 57-66.
15. Gil, A., Medrano, M., Martorell, I., Lazaro, A., Dolado, P., Zalba, B., & Cabeza, L. F. (2010). State of the art on high temperature thermal energy storage for power generation. Part 1—Concepts, materials and modellization. *Renewable and Sustainable Energy Reviews*, *14*(1), 31-55.

16. Medrano, M., Gil, A., Martorell, I., Potau, X., & Cabeza, L. F. (2010). State of the art on high-temperature thermal energy storage for power generation. Part 2—Case studies. *Renewable and Sustainable Energy Reviews*, *14*(1), 56-72.
17. Kalogirou, S. A. (2013). Solar thermoelectric power generation in Cyprus: Selection of the best system. *Renewable Energy*, *49*, 278-281.
18. Romero, M., Buck, R., & Pacheco, J. E. (2002). An update on solar central receiver systems, projects, and technologies. *Journal of solar energy engineering*, *124*(2), 98-108.
19. Steinmann, W. D., & Eck, M. (2006). Buffer storage for direct steam generation. *Solar Energy*, *80*(10), 1277-1282.
20. Tian, Y., & Zhao, C. Y. (2013). A review of solar collectors and thermal energy storage in solar thermal applications. *Applied Energy*, *104*, 538-553.
21. http://www.wikipedia.com
22. www.cspworld.com.
23. http://americanhistory.si.edu/powering/images/gallry53.html
24. http://inhabitat.com/sevilles-solar-power-tower/
25. Ho, C. K., & Iverson, B. D. (2014). Review of high-temperature central receiver designs for concentrating solar power. *Renewable and Sustainable Energy Reviews*, *29*, 835-846.
26. Bienert WB, Rind H, Wolf AA. Conceptual design of an open cycle air Brayton Solar Receiver: Phase 1 final report, DTM-79-1 prepared under contract no. 955135 for California Institute of Technology Jet Propulsion Laboratory, Dynatherm Corporation, Cockeysville, MD. 1979.
27. Heller P, Pfander M, Denk T, Tellez F, Valverde A, Fernandez J, et al. Test and evaluation of a solar powered gas turbine system. Solar Energy 2006;80 (10):1225–30.
28. Amsbeck L, Buck R, Heller P, Jedamski J, Uhlig R. Development of a tube receiver for a solar-hybrid microturbine system. In: Proceedings of the 2008 SolarPACES Conference, Las Vegas, NV; March 4–7, 2008.
29. Amsbeck L, Helsch G, Roger M, Uhlig R. 2009. Development of a Broadband antireflection coated transparent silica window for a solar-hybrid microturbine systems. In: Proceedings of solarPACES 2009, Berlin, Germany; September 15–18, 2009.
30. Heller P, Jedamski J, Amsbeck L, Uhlig R, Ebert M, Svensson M, et al. Development of a solar-hybrid microturbine system for a mini-tower. In: Proceedings of SolarPACES 2009, Berlin, Germany; September 15–18, 2009.
31. Amsbeck L, Denk T, Ebert M, Gertig C, Heller P, Herrmann P, et al. Test of a solar-hybrid microturbine system and evaluation of storage deployment. In: Proceedings of solarPACES 2010, Perpignan, France; September 21–24, 2010.
32. Uhlig R. Transient stresses at metallic solar tube receivers. In: Proceedings of solarPACES 2011, Granada, Spain; September 20–23, 2011.
33. Kolb GJ. An evaluation of possible next-generation high-temperature mol-ten-salt power towers, Sandia National Laboratories, SAND2011-9320, Albu-querque, NM. 2011.

34. Kelly B. Advanced thermal storage for central receivers with supercritical coolants. Lakewood, CO: Abengoa Solar, Inc.; 2010 (DE-FG36-08GO18149).
35. Pacheco JE. Final test and evaluation results from the solar two project, SAND2002-0120. Albuquerque, NM: Sandia National Laboratories; 2002.
36. Radosevich LG. Final report on the power production phase of the 10 MWe solar thermal central receiver pilot plant, SAND87-8022, Sandia National Laboratories, Albuquerque, NM. 1988.
37. Smith DC. Design and optimization of tube-type receiver panels for molten salt application. In: ASME international solar energy conference, Maui, HI, USA; April 5–9, 1992.
38. Smith DC, Chavez JM. A final report on the phase I testing of a molten-salt cavity receiver, SAND87-2290, Sandia National Laboratories, Albuquerque, NM. 1987.
39. Schiel WJC, Geyer MA. Testing an external sodium receiver up to heat fluxes of 2.5 MW/m2: results and conclusions from the IEA-SSPS high flux experi-ment conducted at the central receiver system of the Plataforma Solar de Almeria (Spain). Solar Energy 1988;41(3):255–65.
40. Drouot LP, Hillairet MJ. The themis program and the 2500-kW themis solar power-station at Targasonne. Journal of Solar Energy Engineering-Transac-tions of the ASME 1984;106(1):83–9.
41. Falcone PK. A handbook for solar central receiver design, SAND86-8009. Livermore, CA: Sandia National Laboratories; 1986.
42. Forsberg CW, Peterson PF, Zhao HH. High-temperature liquid-fluoride-salt closed-Brayton-cycle solar power towers. Journal of Solar Energy Engineer-ing-Transactions of the ASME 2007;129(2):141–6.
43. Smith DC. Design and optimization of tube-type receiver panels for molten salt application. In: ASME international solar energy conference, Maui, HI, USA; April 5–9, 1992.
44. Smith DC, Chavez JM. A final report on the phase I testing of a molten-salt cavity receiver, SAND87-2290, Sandia National Laboratories, Albuquerque, NM. 1987.
45. Singer C, Buck R, Pitz-Paal R, Muller-Steinhagen H. Assessment of solar power tower driven ultrasupercritical steam cycles applying tubular central receivers with varied heat transfer media. Journal of Solar Energy Engineer-ing 2010;132(4):041010 1–12.
46. Ambrosini A, Lambert TN, Bencomo M, Hall A, K vanEvery, Siegel NP, et al. Improved high temperature solar absorbers for use in concentrating solar power central receiver applications, in energy sustainability, Washington DC; August 7–10, 2011.
47. Kennedy CE, Laboratory NRE. Review of mid- to high-temperature solar selective absorber materials, NREL/TP-520-31267, National Renewable Energy Laboratory, Golden, CO. 2002.
48. Epstein M, Liebermann D, Rosh M, Shor AJ. Solar testing of 2 MWth water/ steam receiver at the Weizmann Institute solar tower. Solar Energy Materials 1991;24(1–4):265–78.

49. Li X, Kong W, Wang Z, Chang C, Bai F. Thermal model and thermodynamic performance of molten salt cavity receiver. Renewable Energy 2010;35(5):981–8.
50. Freeman ES. The kinetics of the thermal decomposition of sodium nitrate and of the reaction between sodium nitrite and oxygen. Journal of Physical Chemistry 1956;60(11):1487–93.
51. Siebers DL, Kraabel JS. Estimating convective energy losses from solar central receivers. Livermore, CA: Sandia National Laboratories; 1984 (SAND84-8717).
52. Persky MJ, Szczesniak M. Infrared, spectral, directional-hemispherical reflectance of fused silica, teflon polytetrafluoroethylene polymer, chrome oxide ceramic particle surface, Pyromark 2500 paint, Krylon 1602 paint, and Duraflect coating. Applied Optics 2008;47(10):1389–96.
53. Ambrosini A, Lambert TN, Bencomo M, Hall A, K vanEvery, Siegel NP, et al. Improved high temperature solar absorbers for use in concentrating solar power central receiver applications. In: Proceedings of the ASME 2011 energy sustainability and fuel cell conference, ESFuelCell2011-54241, Washington DC; August 7–10, 2011.
54. Hall A, Ambrosini A, Ho C. Solar selective coatings for concentrating solar power central receivers. Advanced Materials & Processes 2012;170(1):28–32.
55. Niu, X. D., Yamaguchi, H., Zhang, X. R., Iwamoto, Y., & Hashitani, N. (2011). Experimental study of heat transfer characteristics of supercritical CO 2 fluid in collectors of solar Rankine cycle system. Applied Thermal Engineering, 31(6), 1279-1285.
56. Kim, H. Y., Kim, H., Song, J. H., Cho, B. H., & Bae, Y. Y. (2007). Heat transfer test in a vertical tube using CO_2 at supercritical pressures. Journal of nuclear science and technology, 44(3), 285-293.
57. Fourier, J. B. J. (1827). Les temperature du globe terrestre et des espaces planétaires. *Mémoires de l'académie royale des sciences de l'institut de France, Tome VII*.
58. Caliot, C., & Flamant, G. (2014). Pressurized Carbon Dioxide as Heat Transfer Fluid: Influence of Radiation on Turbulent Flow Characteristics in Pipe. AIMS Energy, 3(2), 172-182.
59. Rothman, L. S., Gordon, I. E., Babikov, Y., Barbe, A., Chris Benner, D., Bernath, P. F., ... & Wagner, G. (2013). The HITRAN2012 molecular spectroscopic database. Journal of Quantitative Spectroscopy and Radiative Transfer, 130, 4-50.
60. Rothman, L. S., Gordon, I. E., Barber, R. J., Dothe, H., Gamache, R. R., Goldman, A., ... & Tennyson, J. (2010). HITEMP, the high-temperature molecular spectroscopic database. Journal of Quantitative Spectroscopy and Radiative Transfer, 111(15), 2139-2150.
61. Incropera, F., & DeWitt, D. (1985). Introduction to heat transfer.
62. ANSYS Academic Research, Release 13.0, Help System, Fluent Theory Guide, ANSYS, Inc, pp. 1-18, 41-174, 577-640.
63. Lemmon, E.W., Huber, M.L., McLinden, M.O., (2013), NIST Standard Reference Database 23: Reference Fluid Thermodynamic and Transport Properties-REFPROP,

Version 9.1, National Institute of Standards and Technology, Standard Reference Data Program, Gaithersburg

64. Span, R., & Wagner, W. (1996). A new equation of state for carbon dioxide covering the fluid region from the triple point temperature to 1100 K at pressures up to 800 MPa. Journal of physical and chemical reference data, 25(6), 1509-1596.
65. Modest, M. F. (1993). Radiation heat transfer. McGraw, New York.
66. Cook W. J. and Felderman E.J. "Reduction of data from thin film heat transfer gauges: a concise numerical technique", AIAA J. Vol. 4. No 3, 1966, pp 561-562.
67. Anderson, J. D. (1990). Modern compressible flow: with historical perspective (Vol. 12). New York: McGraw-Hill.
68. Kumar, C. S., Takayama, K., & Reddy, K. P. J. (2014). Shock waves made simple. Wiley-Blackwell.
69. http://silver.neep.wisc.edu/~shock/tools/gdcalc.html
70. Jagadeesh G., Reddy N.M., Nagashetty K., Reddy K.P.J., "Fore-body Convective Hypersonic Heat Transfer Measurements Over Large Blunt Cones", Journal of Spacecraft and Rockets, 37-1, pp 137-139, 2000.
71. Srinivasa P., "Experimental Investigations of Hypersonic Flow over a Bulbous Heat Shield at Mach number of 6", PhD Dissertation, Indian Institute of Science, Bangalore, 1991.
72. Fay J.A., Riddell F.R., "Theory of Stagnation Point Heat Transfer in Dissociated Air", Journal of the Aeronautical Sciences, Vol. 25, No. 2, pp 73-85, 1958.
73. Kumar, C. S. (2017). Experimental Investigation of Aerodynamic Interference Heating Due to Protuberances on Flat Plates and Cones Facing Hypersonic Flows, PhD Dissertation, Indian Institute of Science, Bangalore, 2017.
74. Kumar, Chintoo Sudhiesh, Kazuyoshi Takayama, and K. P. J. Reddy. Shock waves made simple. Wiley-Blackwell, 2014.
75. Farag, I. H., & Allam, T. A. (1982). Carbon dioxide standard emissivity by mixed gray-gases model. Chemical Engineering Communications, 14(3-6), 123-131.
76. Dostal V., "A supercritical carbon dioxide cycle for next generation nuclear reactors," PhD Thesis, Nuclear Engineering, (2004) Massachusetts Institute of Technology.
77. Wendelin, T., 2003, "SolTRACE: A New Optical Modeling Tool for Concentrating Solar Optics," Proceedings of the ISEC 2003: International Solar Energy Conference, 15-18 March 2003, Kohala Coast, Hawaii. New York: American Society of Mechanical Engineers, pp. 253-260; NREL Report No. CP-550-32866.
78. Ortega, J. D., Yellowhair, J. E., Ho, C. K., "Calorimetric Evaluation of Novel Concentrating Solar Receiver Geometries with Enhanced Effective Solar Absorptance", Proceedings of the 10th International Conference on Energy Sustainability (ES2016), San Diego, CA, June 26th – 30th 2016.
79. Garbrecht, O., Al-Sibai, F., Kneer, R., and Wieghardt, K., 2013, "CFD-simulation of a new receiver design for a molten salt solar power tower," Solar Energy(90), pp. 94-106.
80. Friefield, J. M., and Friedman, J., 1974, "Technical Report No. 1: Solar Thermal Power Systems Baded on Optical Transmission,"Rocketdyne Division, Rockwell International.

81. "U.S. Patent Application 14535100, Filed Nov. 6, 2014, BLADED SOLAR THERMAL RECEIVERS FOR CONCENTRATING SOLAR POWER".
82. Christian, J. M., Ortega, J. D., Ho, C. K., (2015, June). Novel Tubular Receiver Panel Configurations For Increased Efficiency Of High-Temperature Solar Receivers. In ASME 2015 9th International Conference on Energy Sustainability, American Society of Mechanical Engineers, paper number ES2015-49431.
83. Christian, J. M., Ortega, J. D., Ho, C. K., & Yellowhair, J. (2016, June). Design and Modeling of Light-Trapping Tubular Receiver Panels. In ASME 2016 10th International Conference on Energy Sustainability collocated with the ASME 2016 Power Conference and the ASME 2016 14th International Conference on Fuel Cell Science, Engineering and Technology (pp. V001T04A005-V001T04A005). American Society of Mechanical Engineers.
84. Ortega, J., Khivsara, S., Christian, J., Ho, C., & Dutta, P. (2016). Coupled modeling of a directly heated tubular solar receiver for supercritical carbon dioxide Brayton cycle: Structural and creep-fatigue evaluation. Applied Thermal Engineering, 109, 979-987.
85. ASME Boiler and Pressure Vessel Code. New York, NY: American Society of Mechanical Engineers, 2013